COMENIUS UNIVERSITY IN BRATISLAVA

FACULTY OF MATHEMATICS, PHYSICS AND INFORMATICS

DEPARTMENT OF NUCLEAR PHYSICS AND BIOPHYSICS

DEVELOPMENT AND UTILIZATION OF IBA TECHNIQUES FOR MATERIAL ANALYSIS

Dissertation thesis

BRATISLAVA 2017 **Mgr. Jakub Zeman**

COMENIUS UNIVERSITY IN BRATISLAVA

FACULTY OF MATHEMATICS, PHYSICS AND INFORMATICS

DEPARTMENT OF NUCLEAR PHYSICS AND BIOPHYSICS

DEVELOPMENT AND UTILIZATION OF IBA TECHNIQUES FOR MATERIAL ANALYSIS

Dissertation thesis

Study programme:	Nuclear and Subnuclear Physics
Field of study:	4.1.5. Nuclear and Subnuclear Physics
Department:	Department of Nuclear Physics and Biophysics
Supervisor:	prof. RNDr. Pavel Povinec, DrSc.

BRATISLAVA 2017 **Mgr. Jakub Zeman**

Comenius University in Bratislava
Faculty of Mathematics, Physics and Informatics

THESIS ASSIGNMENT

Name and Surname:	Mgr. Jakub Zeman
Study programme:	Nuclear and Subnuclear Physics (Single degree study, Ph.D. III. deg., full time form)
Field of Study:	Nuclear And Subnuclear Physics
Type of Thesis:	Dissertation thesis
Language of Thesis:	English
Secondary language:	Slovak

Title: Development and utilization of IBA techniques for material analysis

Aim: PIXE is one of the most employed IBA techniques for elemental composition of samples, while it is used in various sectors from physical and technological sciences through nature sciences up to analysis of pieces of art. Main advantage of PIXE technique is high sensitivity for elements heavier than sodium, as well as, it is a non-destructive method. At the Department of nuclear physics and biophysics a new Center for Nuclear and Accelerator technologies (CENTA) was established. This center is equipped with new system for ion production and analysis of various ion types, while PIXE analysis represents one of possible utilizations. Gaseous ion source will be used for helium ions production in case of PIXE analyzes. These ions will be accelerated by the tandem accelerator Pelletron, which represents the crucial device installed in the CENTA laboratory. A PhD. student will be, together with the employees of the Department of nuclear physics and biophysics, as well as via cooperation with foreign laboratories, participating in the development of PIXE method and its utilization for various samples analyzes, e.g. aerosol filters, meteorites, etc. as well as material from everyday life (coins, rocks, etc.). The part of PhD. student's work will be also a development of proton beam for further analyzes, e.g. development of PIGE and RBS method. The PhD. student will be sent for a study stay abroad.

Comment: The thesis follows ongoing projects:
IAEA project: Centre for Nuclear and Accelerator technologies
APVV project: Slovak meteorites research
VEGA project: Košice meteorite and similar chondrites research
Cooperating laboratories:
University in Vienna, VERA laboratory
University in Arizona, Tucson, USA
IAEA Vienna and Monaco
R. Boskovic Institute, Zagreb
Institute of Physics, Slovak Academy of Sciences, Bratislava
FEI STU, Bratislava

Tutor:	prof. RNDr. Pavel Povinec, DrSc.
Department:	FMFI.KJFB - Department of Nuclear Physics and Biophysics
Head of department:	prof. RNDr. Stanislav Tokár, DrSc.

Comenius University in Bratislava
Faculty of Mathematics, Physics and Informatics

Assigned: 25.02.2013

Approved: 25.02.2013 prof. RNDr. Jozef Masarik, DrSc.
Guarantor of Study Programme

.....
Student

.....
Tutor

Univerzita Komenského v Bratislave
Fakulta matematiky, fyziky a informatiky

ZADANIE ZÁVEREČNEJ PRÁCE

Meno a priezvisko študenta: Mgr. Jakub Zeman
Študijný program: jadrová a subjadrová fyzika (Jednoodborové štúdium, doktorandské III. st., denná forma)
Študijný odbor: jadrová a subjadrová fyzika
Typ záverečnej práce: dizertačná
Jazyk záverečnej práce: anglický
Sekundárny jazyk: slovenský

Názov: Development and utilization of IBA techniques for material analysis
Vývoj a využitie IBA metód na analýzu materiálov

Cieľ: PIXE je jednou z najpoužívanejších IBA metód na určenie prvkového zloženia vzoriek, pričom je používaná v rôznych odvetviach od fyzikálnych a technologických vied cez prírodné vedy až po analýzu umeleckých diel. Jej hlavnou výhodou je vysoká citlivosť pre prvky ťažie ako sodík, ako aj to, že sa jedná o nedeštruktívnu metódu. Na Katedre jadrovej fyziky a biofyziky bolo vybudované Centrum pre nukleárne a urýchľovačové technológie (CENTA). Toto centrum je vybavené novým systémom na produkciu a analýzu rôznych typov iónov, pričom jedným z možných využití je aj PIXE analýza. V prípade PIXE analýz ako zdroj iónov sa bude používať plynový zdroj iónov produkujúci ióny hélia. Tieto ióny budú urýchľované v tandemovom urýchľovači Pelletrone, ktorý je hlavným zariadením inštalovaným v laboratóriu CENTA. Dizertant sa v spolupráci so zamestnancami KJFB, ako aj v spolupráci s viacerými zahraničnými pracoviskami bude podieľať na vývoji PIXE metódy a jej využití na analýzu rôznych typov vzoriek, napr. aerosólových filtrov, meteoritov, a pod. ako aj predmetov z bežného života (mince, kamene atď.) Súčasťou práce dizertanta bude aj vývoj a využitie protónového zväzku na ďalšie analýzy, napr. na vývoj PIGE a RBS metód. Dizertant počas práce na dizertácii bude vyslaný na študijný pobyt do zahraničia.

Poznámka: Náväznosť témy na riešené projekty:
IAEA projekt: Centrum nukleárnych a urýchľovačových technológií
APVV projekt: Výskum slovenských meteoritov
VEGA projekt: Výskum meteoritu Košice a podobných chondritov
Spolupracujúce pracoviská:
Univerzita vo Viedni, VERA laboratórium
Arizonská univerzita, Tucson, USA
IAEA Viedeň a Monako
R. Boskovic Institute, Zagreb
Fyzikálny ústav SAV, Bratislava
FEI STU, Bratislava

Školiteľ: prof. RNDr. Pavel Povinec, DrSc.
Katedra: FMFI.KJFB - Katedra jadrovej fyziky a biofyziky
Vedúci katedry: prof. RNDr. Stanislav Tokár, DrSc.

Univerzita Komenského v Bratislave
Fakulta matematiky, fyziky a informatiky

Dátum zadania: 25.02.2013

Dátum schválenia: 25.02.2013 prof. RNDr. Jozef Masarik, DrSc.
garant študijného programu

.....
študent

.....
školiteľ

Statement of the author

I honestly declare that presented thesis was elaborated by my person using listed bibliography and internet sources. These sources of information are listed at the end of the thesis.

Bratislava 2017 …….

Jakub Zeman

Acknowledgements

I would like to express my thanks to everyone who supported me in any way within the whole time of this thesis elaboration.

My first thanks belong to my tutor, professor Pavel Povinec, who supported me with ideas and who was always there to explain unclear physics behind the problems under study. His enthusiasm and dedication to nuclear and environmental physics pushed me forward all the time.

Next, I would like to thank my colleagues, namely dr. Miroslav Ješkovský, dr. Jakub Kaizer, Mgr. Ján Pánik and Mgr. Ivan Kontuľ. I am extraordinary grateful for their time spent with me in the laboratory performing analyzes. Many of solved problems in presented thesis would not be done without their knowledge and professional skills. I have appreciated the team work and spirit.

I am pleased to express my thanks to Assoc. Professors Ivan Sýkora and Jaroslav Staníček who were so kind to help with the calibration and optimization of setup installed in the CENTA laboratory. I also thank to drs. Alexander Šivo and Marta Richtáriková for their skills in chemical laboratory during sample preparation. Special thanks go to Mr. Miroslav Šulc, Mr. Jozef Haško, Mr. Eduard Hanuska, dr. Ján Szarka and all other members of the team who often helped to solve technical problems.

Furthermore, I express my gratitude to dr. Róbert Breier for his unique skills concerning computers, programming and all kind of software related issues.

I feel immense gratefulness to my family, friends and everyone who stood behind me all the time. Their support and relationship were very helpful in crucial times.

Last but not least, I like to thank to my fiancée, Martina. Your patience and love is the engine in my life.

Abstract

Zeman, Jakub. Development and utilization of IBA techniques for material analysis. [Dissertation thesis]. Comenius University in Bratislava, Faculty of Mathematics, Physics and Informatics.
Supervisor: prof. RNDr. Pavel Povinec, DrSc. Level of professional qualifications: PhD. in the field of Nuclear and Subnuclear Physics. Bratislava: FMFI UK, 2017. 153 p.

Ion beam analysis (IBA) techniques have been developed in order to retrieve information about material compositions avoiding destruction of investigated samples. Individual techniques employed various approaches in this process. The common aspect of IBA techniques is analysis of processes occurring within interactions of ion beam with the material. High demands are being put on of well-defined ion beams which can be used for such research. Proper adjustment of the detection setup has been crucial to obtain reliable results.

The first part of the presented thesis comprises a description of the IBA techniques. The emphasis is put on five main IBA techniques: RBS, ERDA, PIXE, PIGE and NRA. Principles and possible utilization of mentioned methods are briefly explained. Further, a description of the experimental setup of the CENTA laboratory is presented. Information on ion sources, on the injection beam-line system, on the tandem accelerator, and on the focusing and analyzing systems is provided together with corresponding figures. Ion beam optics devices used for the beam manipulation and stabilization are presented as well.

The experimental part comprises of four chapters containing optimization of ion beam trajectories, calibration and adjustment of detection setup, and results of PIXE analyzes carried out in the laboratory in past year and a half. Important results on successful evaluation of the iron distribution in a sample of rat brain using GUPIXWIN software are presented as well.

Conclusion summarizes all results, giving an overall insight into the topic. Stripping efficiency measurements, beam profile simulations, PIXE chamber adjustment and results of material analyzes show how much effort had to be spent to achieve the objectives of presented thesis.

Key words: IBA techniques, tandem accelerator, transmission efficiency, SIMION beam profile simulations, PIXE, GUPIXWIN, elemental composition.

Abstrakt

Zeman, Jakub. Vývoj a využitie IBA metód na analýzu materiálov. [Dizertačná práca]. Univerzita Komenského v Bratislave. Fakulta matematiky, fyziky a informatiky. Katedra jadrovej fyziky a biofyziky.
Školiteľ: prof. RNDr. Pavel Povinec, DrSc. Stupeň odbornej kvalifikácie: PhD. v odbore Jadrová a subjadrová fyzika. Bratislava : FMFI UK, 2015. 153 s.

IBA metódy (z anglického Ion Beam Analysis, analýza pomocou iónového zväzku) sú vyvíjané so zámerom zistiť zloženie materiálu, pričom sa dbá na to, aby sledovaný materiál nebol poškodený. Jednotlivé IBA metódy využívajú rôzne prístupy, pričom spoločným prvkom je analýza procesov, ku ktorým dochádza počas interakcie zväzku iónov s materiálom. Na zväzky iónov, ktoré je možné využiť sú kladené vysoké nároky. Správne nastavenie celého detekčného systému je nutné pre dosiahnutie hodnoverných výsledkov.

Prvá časť predkladanej práce sa zaoberá opisom IBA techník. Dôraz je kladený na 5 hlavných IBA metód, menovite: RBS, ERDA, PIXE, PIGE a NRA. Ich princípy a možné využitia sú stručne zhrnuté v tejto časti. Ďalej táto časť obsahuje opis experimentálneho vybavenia CENTA laboratória. Hlavné informácie týkajúce sa iónových zdrojov, vstupnej urýchľovacej trasy, tandemového urýchľovača, fokusujúceho a analyzujúceho kanála spolu so zodpovedajúcimi obrázkami sa nachádzajú na niekoľkých stranách. Tiež sú tu opísané prvky iónovej optiky, ktoré slúžia na manipuláciu so zväzkom a jeho stabilizáciu.

Experimentálna časť práce pozostáva zo 4 kapitol, ktoré sa venujú optimalizácii trajektórie iónového zväzku, kalibrácii a nastaveniu detekčného systému a výsledkom PIXE analýz, ktoré boli realizované v laboratóriu za posledného jeden a pol roka. Najdôležitejším výsledkom je ohodnotenie koncentrácie železa vo vzorke z mozgu potkana využitím programu GUPIXWIN.

Záver práce zhŕňa všetky výsledky poskytujúc celkový pohľad do problematiky. Meranie účinnosti stripovania, simulácie profilu iónového zväzku, nastavenia PIXE komory a výsledky analýz ukazujú, aké úsilie muselo byť vynaložené, aby sa dosiahli ciele predkladanej práce.

Kľúčové slová: IBA techniky, tandemový urýchľovač, účinnosť stripovania, SIMION simulácie profilu zväzku, PIXE, GUPIXWIN, prvkové zloženie.

Foreword

The author of presented work was fascinated by physics since his early youth. After high school he chose to study physics at Faculty of Mathematics, Physics and Informatics of the Comenius University in Bratislava, and he finished by successful master graduation in nuclear and sub-nuclear physics. Then he was accepted by professor Povinec to start his dissertation thesis at the newly formed CENTA facility. The scope of his thesis concerned the IBA techniques which have been under development in the CENTA facility.

Four years have passed and the subject of the thesis was investigated into details. Principles and possible utilization of individual IBA techniques have been understood. The whole time period was rather exciting and pioneering. Tandem accelerator installed in the CENTA laboratory was first of this kind in Slovakia. Therefore the staff together with PhD students had to handle many technical difficulties together with involved physics behind.

Developments in the CENTA laboratory proceeded in several steps and this process is still ongoing. At the beginning, after the first laboratory installation in summer 2013, first test measurements were carried out. The author had to be very flexible and patient because all of the things were new to him as well as to his colleagues. Many measurements had to be repeated to obtain reliable results. Later, in September 2015, an additional PIXE/PIGE beam line was installed so PIXE analyzes of different materials could be carried out.

The thesis goals were followed in order to achieve valuable results. Many, many hours spent in the laboratory and afterwards processing the data and performing analyzes lead to successful completion of the thesis. The author hopes that the presented results will satisfy the expectations.

The setup of the CENTA laboratory is still under continual development. Every month brings something new and novel approaches are revealed to optimize the performance of utilized detection and analytical systems. Hopefully, successfully solved projects will bring new possibilities and physics' directions in further developments of the CENTA facility.

Goals of the dissertation thesis

The goals of the thesis may be summarized as follows:

(i) Ion beam trajectory simulations using SIMION software.

(ii) Ion source optimization for proton and helium beams production using the ALPHATROSS ion source, and for beryllium and carbon beams using the MC-SNICS ions source.

(iii) Investigations of tandem accelerator transmissions for protons, helium, beryllium and carbon ions.

(iv) Optimization of the analyzing beam line.

(v) Development of IBA techniques (PIXE, PIGE) for elemental analyzes of materials.

(vi) Calibration methods and interpretation of acquired results.

Contents

1. Introduction

In November 2015 a new laboratory for nuclear and environmental research and for development of nuclear technologies was established at the Department of Nuclear Physics and Biophysics at the Faculty of Mathematics, Physics and Informatics, Comenius University in Bratislava. This laboratory was given a name CENTA (Centre for Nuclear and Accelerator Technologies). The facility is equipped with a system that is capable of various ions production and their further application and analysis. The main device in the laboratory is an electrostatic linear tandem accelerator, which is designed for obtaining of ion beams with acquired attributes (energy, intensity etc.). The main scientific purpose of the laboratory is the gradual implementation and consecutive utilization of ion beam techniques and methods primary in nuclear and environmental sciences. The idea is to extend the area of research on new material development and surface treatment of materials using ion beams.

The basic equipment of the laboratory consists of two ion sources – Alphatross for gaseous targets and MC-SNICS for solid targets; 3 MV electrostatic linear tandem accelerator Pelletron; electrostatic analyzer; two bending magnets and a magnetic quadrupole triplet.

The techniques that are being developed in the laboratory can be divided in 3 groups:

1.) IBA – Ion Beam Analysis, techniques for material and sample analysis.
2.) AMS – Accelerator Mass Spectrometry, specifying of isotope content in various samples.
3.) IBM – Ion Beam Modification, techniques for material surface treatment, material aging in high ion flows etc.

IBA techniques are used for various material analyses for physical and technological sciences. Results are more and more introduced into the industry as well. The leading techniques in the world are PIXE, RBS, ERDA and NRA analysis. They are used for new material development for nanotechnology, as well as in the area of medicine and biotechnology. Via proper application of these techniques a chemical elemental

composition and depth profiles can be obtained. Depending on the specified material, the surface layers from nanometers up to several hundreds of nanometers (and possibly up to microns) can be analyzed. The IBA techniques represent an important role at material studies in the new generation of nuclear fission reactors development and development of thermonuclear fusion reactors. Further, specific nuclear reactions are being studied using NRA (Nuclear Reaction Analysis) method. These reactions are interesting mainly for astrophysical research, but other reactions are under analysis for different purposes. The importance of the IBA techniques is in the analysis of environmental samples and samples of great historical and cultural value. These techniques are nondestructive, so the is a wide range of possible analysis options for precious samples and materials such as sculptures, paintings, etc.

AMS is the most sensitive method for long-lived radioactive isotopes analysis. The AMS is implemented in various research fields such as nuclear physics, environmental physics, nuclear astrophysics and geophysics, etc. One of the main advantages of the AMS is the low requirement for the sample amount (milligrams down to micrograms are sufficient).

IBM methods are used for modification and treatment of materials for nanotechnologies. The ions penetrating ability into specified depths depending on the ion type and energy are introduced. Such ions can form continuous layers with different properties in the involved material in desired depths. These techniques can monitor the influence of various ion beams on the studied material or sample. In this way, the IBM methods utilize the development of new materials, e.g. construction materials for nuclear fission or thermonuclear reactors.

2. Ion Beam Analysis techniques

Several methods have been developed for material analyzing purposes. The implementation of particular technique depends on multiple factors. The first and most affecting factor is the availability and accessibility of required technique or method, since the majority of the IBA techniques put high demands on the involved technical equipment. The initial investments to the laboratory devices and necessary equipment can reach several hundreds of thousand Euro. Furthermore, the investor (which is usually some university or scientific company) should bear in mind that properly educated scientific stuff for operation and servicing of the whole system is obligatory. The next fundamental factor for analytical technique selection is the matter how can be the samples of interest treated. The analysis of rare and precious samples requires an extraordinary careful treatment. The possible damage or any harm to the sample must be reduced to the minimum. In this case, the value of analyzed samples can have in two aspects. First aspect is that the samples can be of some historical and cultural value, e.g. paintings, sculptures etc. The other aspect is that the sample is precious because it originates from a rare material. It means, that it is possible to analyze fraction of some meteorite or archeological object, but such samples cannot be damaged in any way. For this purpose, multiple nondestructive analytical methods were developed, while the possibilities of these methods are still proceeding. The majority of nondestructive analytical methods have the basis on the applied atomic and nuclear physics because the chemical analysis often requires such chemical procedures which lead to the partial damage or total destruction of samples. But, it is not always a rule, that a sample must be treated carefully. The destructive analytical methods still have an important position in sample analysis because these methods are much cheaper in comparison to the nondestructive techniques and they can even reach desired results faster. The method is therefore chosen according to the sample attributes and the optimal approach, which takes into account the sample properties and analytical method accessibility is selected.

Ion Beam Analysis (IBA) methods are being developed in the CENTA laboratory for samples and materials analysis purpose. IBA techniques are modern analytical techniques which utilize ion beams with energies of several MeV in order to determine the chemical composition of material involved and to investigate the depth profiles in solid samples

[Mayer, 2012]. All IBA methods are extremely sensitive and they can lead to obtain a depth profile in very thin layers. Depending on the analyzed material the typical depth resolution varies between few nanometers to several tenths of nanometers. The depth which is reachable with the IBA techniques varies from nanometers up to tenths of micrometers [Nastasi, 2015]. The best IBA laboratories can reach the uncertainty of few percent in the determination of sample composition.

The most employed IBA techniques are:

1.) RBS and EBS: Rutherford BackScattering and Elastic (non – Rutherford) BackScattering. The RBS technique is especially sensitive for detection of heavier elements (and isotopes) in a material created by lighter elements. The EBS technique is sensitive also to lighter elements. The combination, on the one hand of incidents particle mass and energy, and on the other hand of mass of the elements presented the matrix is crucial in this analytical technique.
2.) ERDA: Elastic Recoil Detection Analysis. This technique is used for determining the content of light elements (and isotopes) in the matrixes consisting of heavier elements. With the increasing mass of elements presented in the matrix, the sensitivity drops. The ERDA technique is a complementary technique to the RBS. For one sample, RBS measurement can determine the content of heavier elements and ERDA can determine the content of lighter elements in the same matrix.
3.) PIXE and PIGE: Particle Induced X-ray Emission and Particle Induced Gamma ray Emission. These techniques are specialized to tracer elements contents determination. They can be used for mostly all elements contents evaluation depending on the sample structure. The number of ions which induce the emission of detected radiation has to be treated carefully.
4.) NRA: Nuclear Reaction Analysis. This method is sensitive to particular isotopes and can provide us information about tracer elements and depending on incident particle energy as well as about most of the isotopes presented in the sample. The proper intensity and energy of incident ion beam is obligatory.

2.1. Rutherford Backscattering

Rutherford Back-Scattering (RBS) technique is used for determination of material chemical composition without using any additional standard material or sample. The RBS technique provides information about the target thickness and depth profile. Usually ion beams consisting of light ions, e.g. protons or helium, are for this analysis. The basis of the technique stands on the kinematics of two body collision (Figure 1).

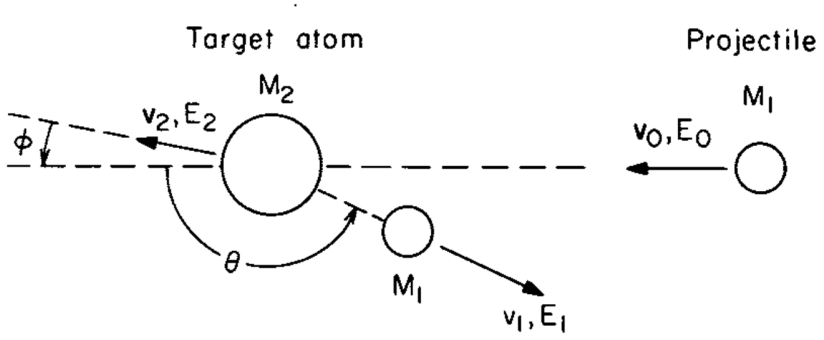

Fig. 1: The RBS technique principle [Chu, 1978]

The incident particle (often denoted as a projectile) with mass M_1, velocity v_0 and kinetic energy E_0 collides with a stable atom (often denoted as a target) in the sample matrix. The target atom has a mass M_2 and since it is considered as a stable atom its kinetic energy equals to zero. In this collision the incident projectile ion transfers a part of its energy to the target atom, which gains energy E_2 and is moving with velocity v_2. After this collision the projectile ion is scattered from the target atom at an angle Θ with a different velocity v_1 and energy E_1. The RBS technique focuses on the detection of the scattered incident particles with the energy E_1, mass M_1 under the angle Θ. Applying the conservation of energy and the conservation of momentum the kinematic factor K can be obtained [Chu, 1978]. This value represents the ratio of E_1/E_0. The higher this ratio is the better is the resolution in the detector. Therefore this technique is widely used in a way of using light particles as projectiles to determine the content of heavier elements (and isotopes) in material matrixes. It is recommended to place detector very close to the beam axis because the amount of backscattered ions increases in this direction [Chu, 1978]. Depending on the energy of backscattered ions and the number of ions with such energies, the particular element concentration can be calculated. The ion beams that are usually used

for the RBS measurements consist of light ions with energy of several MeV and beam diameter approximately one millimeter [Sério, 2012]. Mostly surface barrier detectors are installed in the RBS reaction chamber in the angle close to the beam axis, e .g. 140° backscattered angle Θ [Magalhães, 2012].

In the transmission process when projectile ions penetrate through the specimen material the registered ions are backscattered under angle Θ. While the incident ions are losing their energy not only via Rutherford scattering, the energy E_0 cannot be well defined in the higher depths in the measured material. However, this energy can be estimated and hence the value of energy just before the collision can be calculated. If the matrix material is known then the energy loses can be converted into the depth scale. This is the principle of using the RBS technique to obtain information about several micrometer thick layer from the surface of the sample. Depth profiles of elements presented in the sample matrix can be calculated depending on the particular element composition.

The independence of this technique lies in the possible overcrossing of detected E_1 energy. In the layered sample it is a high possibility to measure the energy of backscattered ions in various ranges. Depending on the occurrence of elements in various depths different backscattered spectra can be obtained and further analysis of the same sample has to be done. Therefore, it is recommended to use another IBA technique to help to understand the nature of measured sample. Usually, laboratories which carry out the RBS measurements also possess a system for at least one different IBA technique, e. g. ERDA, PIXE, NRA or all of them.

2.2. Elastic recoil detection analysis

The ERDA technique is focused on analysis of material surface and the area near the surface of material using beam of positive ions. The majority of projectile ions is being elastically scattered from target atoms, but some amount of projectile ions can get close to the nuclei of atoms in the matrix. Here, the transferred energy can be high enough for target nucleus to leave the material. These recoiled nuclei are subsequently detected. The principle of ERDA is shown in Fig. 2. From the physics point of view, ERDA deals with a two-body elastic collision process in a central force field, where Coulomb interaction plays the main role. It is important that within this process the RBS still occurs. The detailed

physics of this process can be found in [Nastasi, 2015]. One the crucial aspects for ERDA is that the detection system for recoiled nuclei has to be placed in angle greater than the angle for RBS in order to prevent excessive dead time and energy overlap due to the large elastic yield coming from the scattered beam.

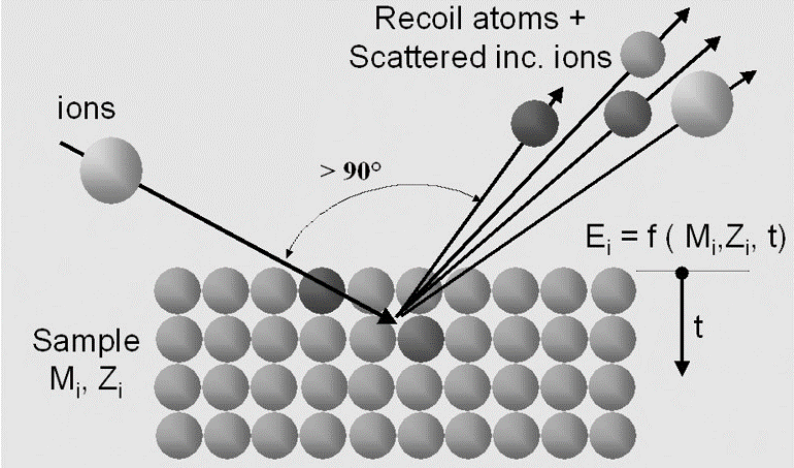

Fig. 2: The ERDA technique principle [ERDA, 2016]

For the detection of recoiled nuclei two approaches are usually chosen. The technique is then done as transmission or reflection ERDA.

At the transmission ERDA the geometry is designed so the beam of projectile ions hits the sample material in the direction of sample surface normal. For thin target material, e.g. foils, thin films, etc., the majority of projectile ions and recoiled nuclei comes out of from the back side of the sample. For thicker targets only particles with higher energy can pass through the material. In both cases the recoiled nuclei are detected at certain angle behind the sample. This technique is limited by the target thickness. For thick samples, i.e., the projectiles and recoils cannot pass through the material, transmission ERDA cannot be applied.

At the reflection ERDA the geometry is different. The incident angle of projectile ion beam is carefully selected so the recoiled nuclei can be detected at desired angle. At this technique a proper option for these angles is crucial because of unwanted detection of scattered projectiles. It is common to set these angles to high values, e.g. 140°. The detection system of recoiled nuclei has to cover a wide range of these nuclei. For this purpose different detection systems have been developed and involved. The most common

in ERDA technique is the Time-Of-Flight (TOF) detection system. For the recoiled nuclei identification magnetic detectors or gas ionization detectors are used. The best results can be reached with combination of multiple detectors. The qualitative analysis has to handle the characterization of recoiled nuclei masses via the energy transfer in the elastic recoil interaction in the process. The quantitative analysis requires the determination of recoiled nuclei yield, which can be converted into the abundance of certain isotope in the analyzed sample material. This yield is determined by elastic cross section for each pair of projectile – target and the angular distribution which is covered by the detection system [Martin, 2003].

The ERDA technique can be used for determining concentration depth profiles or areal densities of hydrogen isotopes (H, D, and T) with helium ion beam as projectiles. The energy of such beam is ~ MeV [Reiche, 2006], [Calligaro, 2001]. For detection of other light isotopes in analyzed samples an ion beam of heavy nuclei as projectiles is used, e.g. ^{35}Cl [Sério, 2012], ^{84}Kr [Msimanga, 2012], ^{127}I [Petersson, 2012]. The energy of projectiles is set from tens of MeV up to ~ 200 MeV.

2.3. Particle induced X-ray emission and gamma-ray emission

Both, PIXE and PIGE techniques, are considered as nondestructive material analytical techniques. This statement is valid within standard conditions for both methods. Obviously, if the intensity and energy of the incident beam exceed certain level then the analyzed material can be damaged even destroyed, especially thin samples. This is valid for RBS and ERDA as well. For low beam intensities ~ nanoamperes (nA) and short measurement times ~ few minutes the effects caused by incident particles are usually negligible.

The PIGE technique represents a modification of PIXE for higher energy of ion beam, sufficient for inducing gamma quanta emission from the target nuclei. The PIGE technique is more sensitive for lighter elements presented in the sample material (Z = 3 – 20). For higher values of proton number Z the Coulomb repulsive potential rises. This prevents the projectile ions to interact with the target nuclei and thus to excite target atoms nucleons what would lead to emission of gamma-rays from deexcitation process. With the increasing proton number Z of target nuclei the probability of projectile ions interactions with the target nuclei decreases. The projectile ions then interact only with atomic shells leading to

emission of X-rays. This is the main reason why is PIGE limited by the Z number and thus can be used as a complementary technique for PIXE analysis.

A possible PIXE detection system geometry is shown in Figure 3.

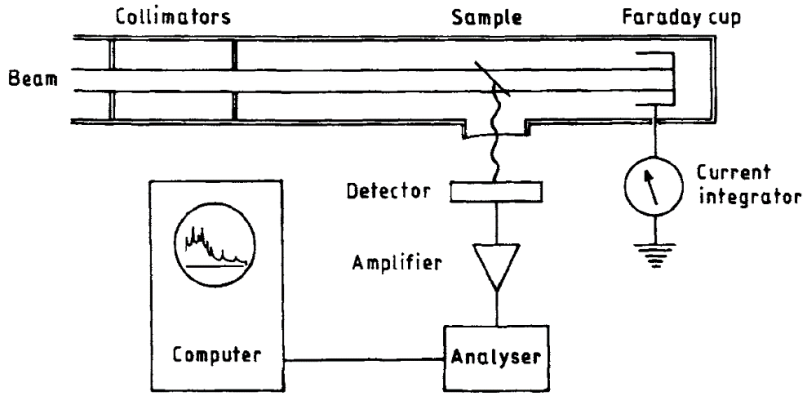

Fig. 3: A schematic view of possible PIXE detection system [Martin, 2003]

The ion beam passes through a collimation system into the chamber with mounted sample. For thin samples a Faraday cup is placed behind the sample. The X-rays produced in the interaction among projectiles and target atoms are detected with detector. The most employed detectors for X-rays are semiconductor detectors, e.g. Si(Li) which have good energetic resolution and high detection efficiency for X-rays. The signal from detector is then processed with a computer and proper software. The explanatory principle of PIXE/PIGE technique is shown in the Figure 4 [Nakai, 2015]. In this example, a thin proton beam is used for X-ray and gamma-ray production in a thin sample material. Induced radiation is being detected by two detectors placed as shown.

Depending on the projectiles energy PIXE is divided into 3 groups. Within the range of 1 – 10 MeV it is classical PIXE, then with energies below 1 MeV it is low-energy PIXE and with energy above 10 MeV it is used to speak about high-energy PIXE technique. The X-rays that are necessary for PIXE analysis have their origin in the interaction of charged particles (projectile ions) with the atoms in the sample matrix (target atoms). The projectiles interact with the target atoms electron shells and these atoms are being ionized. The empty places left behind by excited electrons are being filled with electrons from higher orbital levels. This process is accompanied by the emission of X-rays, which energy

is characteristic for each element. Detection and interpretation of these X-rays is the crucial feature of PIXE analysis.

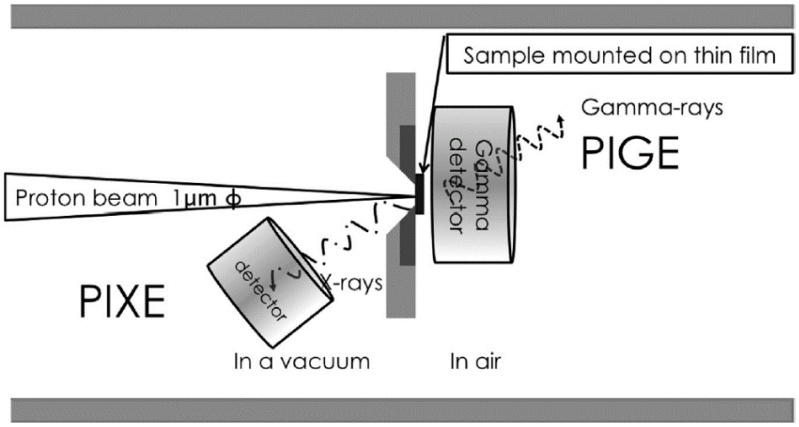

Fig. 4: The principle of PIXE/PIGE technique [Nakai, 2015]

The amount of X-rays produced in the sample is proportional to the amount of the target atoms presented in the sample. There is a strong dependence among X-ray emission and the properties of ion beam that induces this emission. The probability of X-ray production is dependent on the projectile ion beam intensity and on the projectiles energy. It is used to indicate the beam intensity in amperes units. Commonly used intensities are about ~1 mA down to tens of nA. The higher this current is, the higher the X-ray production probability is and vice versa. This probability is also bound to the projectiles energy loses in the sample matrix. According to the projectiles mass and the target nuclei mass the projectiles sequentially loses their energy as they pass through the matter of sample. For PIXE measurements light particles such protons or helium ions are used. With heavier target atoms in the sample the projectiles lose the energy and below a certain value they lose the ability to induce X-ray emission. The whole situation can be imagined as a ball on a snooker table. Although the energy transfer in a single interaction is small, the high amount of interactions significantly reduces the projectiles energy. Since the calibration of whole detection system is done for particular projectiles energy, it is necessary to be aware of the energy loses, and to know exact values for energy loose of the projectile – the matrix system. The determination of particular element abundance in the sample is being done regarding these values as well. The changing projectiles energy as they pass through the matter influences the final determination of the concentration of certain element in the sample. For PIXE analysis the most employed detectors are

semiconductors, e.g. lithium drifted silicon detectors Si(Li) [Chêne, 2012], [Karydas, 2014], [Pichon, 2010], [Tripathy, 2010], [Zucchiatti, 2015], High Purity Germanium detectors HPGe [Denker, 2005], Silicon drifted detectors SDD [Calzolai, 2015], [Manuel, 2014], or combination of more detectors [Morilla, 2012], [Ortega, 2010], [Suárez, 2011].

2.4. Nuclear reaction analysis

The NRA technique focuses on the nuclear reactions which are caused by the incident ion beam on the material surface. The projectile ions interact with atomic structure of the specimen and after entering the sample matter the projectiles begin to lose their energy via interactions with electron shells of atoms presented in the analyzed material. Depending on the projectiles initial energy these ions penetrate to a certain depth into the matter. These energy loses correspond to the Bragg curve so the maximum of energy loss is in the end of the ion path in the matter. The whole NRA technique has the basis standing on these phenomena. The fact that a certain ion loses its energy to a certain value allows using nuclear resonances to maximize the yield from nuclear reaction taking place between projectile and a specific nucleus inside of the sample matter. Via evaluation of these reactions products energy distributions measurements it is possible to obtain the information about depth distribution of target nuclei. Since the nuclear reactions are isotope specific, NRA results can provide information about isotopic composition of the sample.

An example of NRA technique can be monitoring of nuclear reaction: ^{27}Al (p, γ) ^{27}Si where the emitting gammas were measured to obtain information about ^{27}Al displacement [Martin, 2003]. A schematic view for NRA is shown in Fig. 5. The incident ions induce nuclear reactions which products can be detected. In practice are used mostly gammas but other reaction products can be detected as well. In [Založnik, 2016] a reaction D (^{3}He, p) α was monitored and emitting protons were analyzed with a partially depleted Passivated Implanted Planar Silicon (PIPS) detector.

The NRA technique uses the resonance energy for nuclear reactions to observe even small amount of target nuclei in the sample. While the projectile ions lose their energy in the matter at certain depth where is this energy close to the resonance energy the cross section for the process rises what makes possible to measure small abundant isotopes presented in the sample. A nice example of resonance energy exploitation can be found in

[Mathayan, 2016]. They analyzed the lattice location of O^{18} isotope. This can be analyzed by the out coming α-particle yield from the nuclear reaction O^{18} (p, α) N^{15} which has a broad resonance at 820 keV and Q-value of 3.981 MeV. The idea of the resonance energy reaction exploitation is both simple and brilliant. When an incoming particle has higher energy than the resonance energy of the monitored process then there is a well-defined depth in the material where the projectile's initial energy drops to the reaction resonance energy. In this depth the reaction cross section rises rapidly and thus the yield of products rises as well. The signal in the detector, which is set for the searching products, will be stronger. Depending on the particular isotopes of interest concentration in the sample the probability to find desired signal from the wanted reaction rises above the level of unwanted signals from reactions with other isotopes presented in the sample.

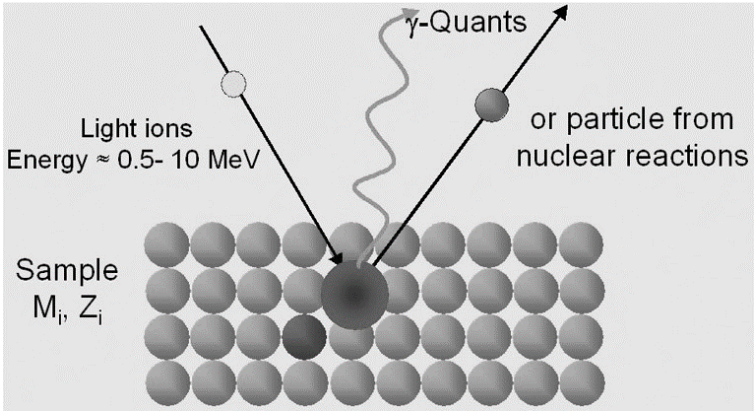

Fig. 5: The principle of NRA technique [NRA, 2016]

The detection of protons, deuterons, ^{3}He and ^{4}He nuclei can be used silicon surface barrier detectors [Guillou, 2014], [Paneta, 2014], [Patronis, 2014], Passivated Implanted Planar Silicon (PIPS) detectors [Carella, 2014] or combination of more detectors to cover range of possible products in the reactions [Borysiuk, 2014]. Another example of NRA study can be [Martin, 2012]. They analyzed the concentration and depth profile of helium implanted into uranium dioxide lattice. The monitored reaction was ^{3}He (d, p) ^{4}He. The projectile deuterons energy was 900 keV and 2 detectors under 0° a 150° angles were detecting the emitting protons. For spectra analysis the SIMNRA software is commonly used. This program simulates the spectra for nuclear reactions and computes the data and results [Bykov, 2012], [Pellegrino, 2012].

3. Experimental setup of the CENTA laboratory

The main intention of CENTA laboratory birth and development was to build a national laboratory that will be able to unify and mediate the scientific research in Slovakia. The range of possible impact of this laboratory is quite broad. The principal focus is aimed at the most recent nuclear technologies that involve an acceleration process to gain ions in various energy states. These ions can be either analyzed directly (in AMS measurements) or can be used for further analysis of samples and material (IBA techniques), or the ion beam can be utilized for material modification (IBM methods). At present, the laboratory is collaborating with more foreign laboratories in Europe on multidisciplinary levels. The AMS measurements are carried out with the VERA laboratory in Vienna, Austria, with the laboratory CIRCE in Naples, Italy and with the laboratory in Debrecen, Hungary. The IBA measurements were performed at the ETH in Zürich, Switzerland and then the PIXE line with chamber for sample irradiation was installed in CENTA. The current equipment in the CENTA laboratory was limited by available funds. At present (April 2017), two ion sources, the injection system, 3 MeV electrostatic tandem accelerator, and high energy analyzer with 2 channels for ion beam measurements are available. All equipment was designed and manufactured in the USA by National Electrostatic Corporation (NEC, Middleton). The funding of the laboratory building and equipment was done thanks to more sources. The main contributions were achieved via European structural and investment funds and the IAEA (International Agency for Atomic Energy).

A floor scheme of the CENTA laboratory is illustrated in the Figure 6. The previous scheme which does not include PIXE/PIGE beam line can be found in [Povinec, 2015B]. Hopefully, in the near future an AMS beam line will be installed. The plan is to install this line on the place where the switching magnet is currently. The whole beam line in forward direction of accelerated ion beam should be shifted into a special laboratory room which was built with double concrete walls for radiation shielding. IBM and further IBA measurements are planned to be carried out inside of this shielded space. The AMS extension should contain a 90° bending magnet which will change the ion trajectory to the left direction of accelerated ion beam. For readers' better imagination, the extensions are shown in the Figure 7.

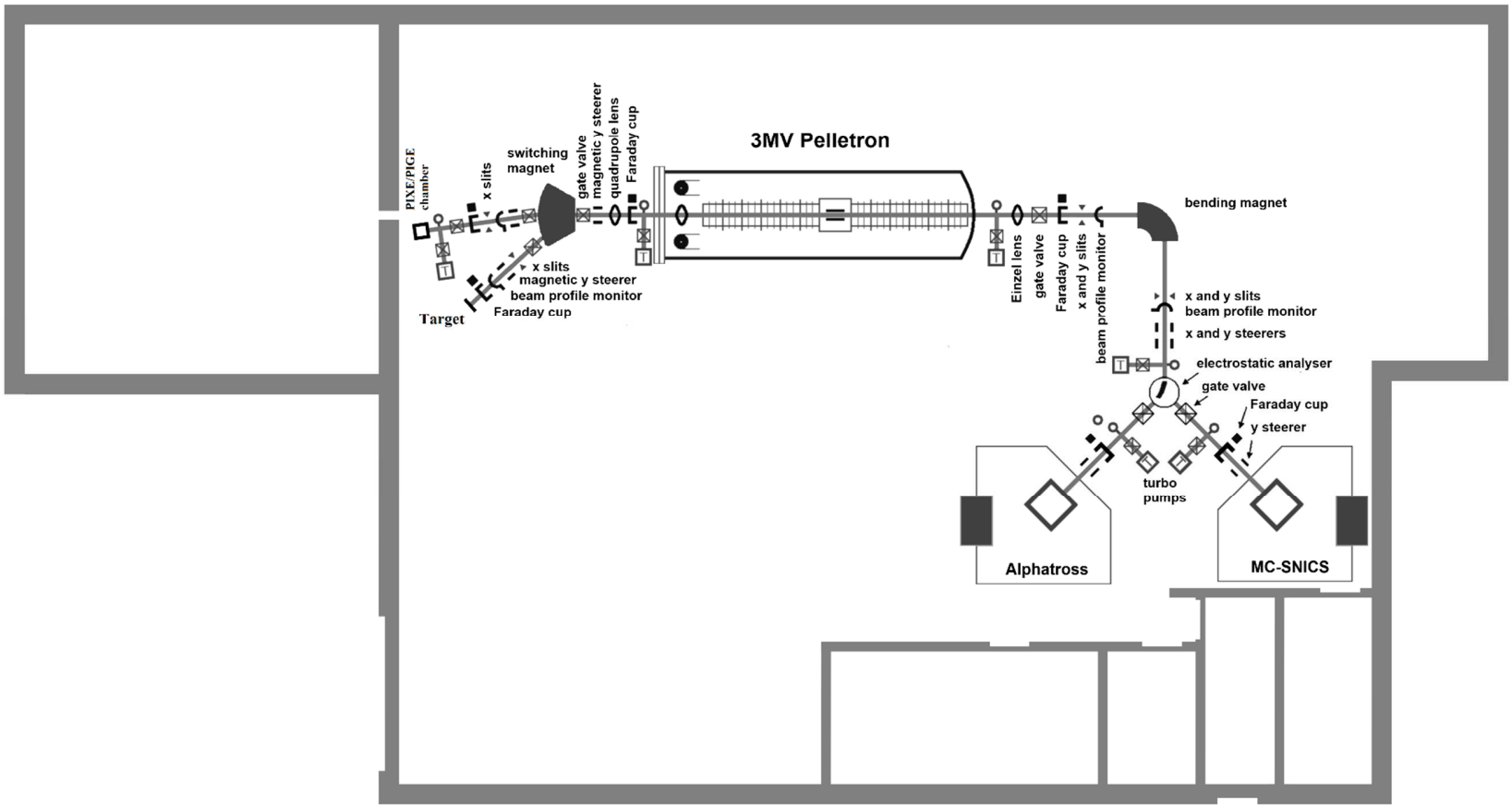

Fig. 6: A floor scheme of the CENTA laboratory (April 2017)

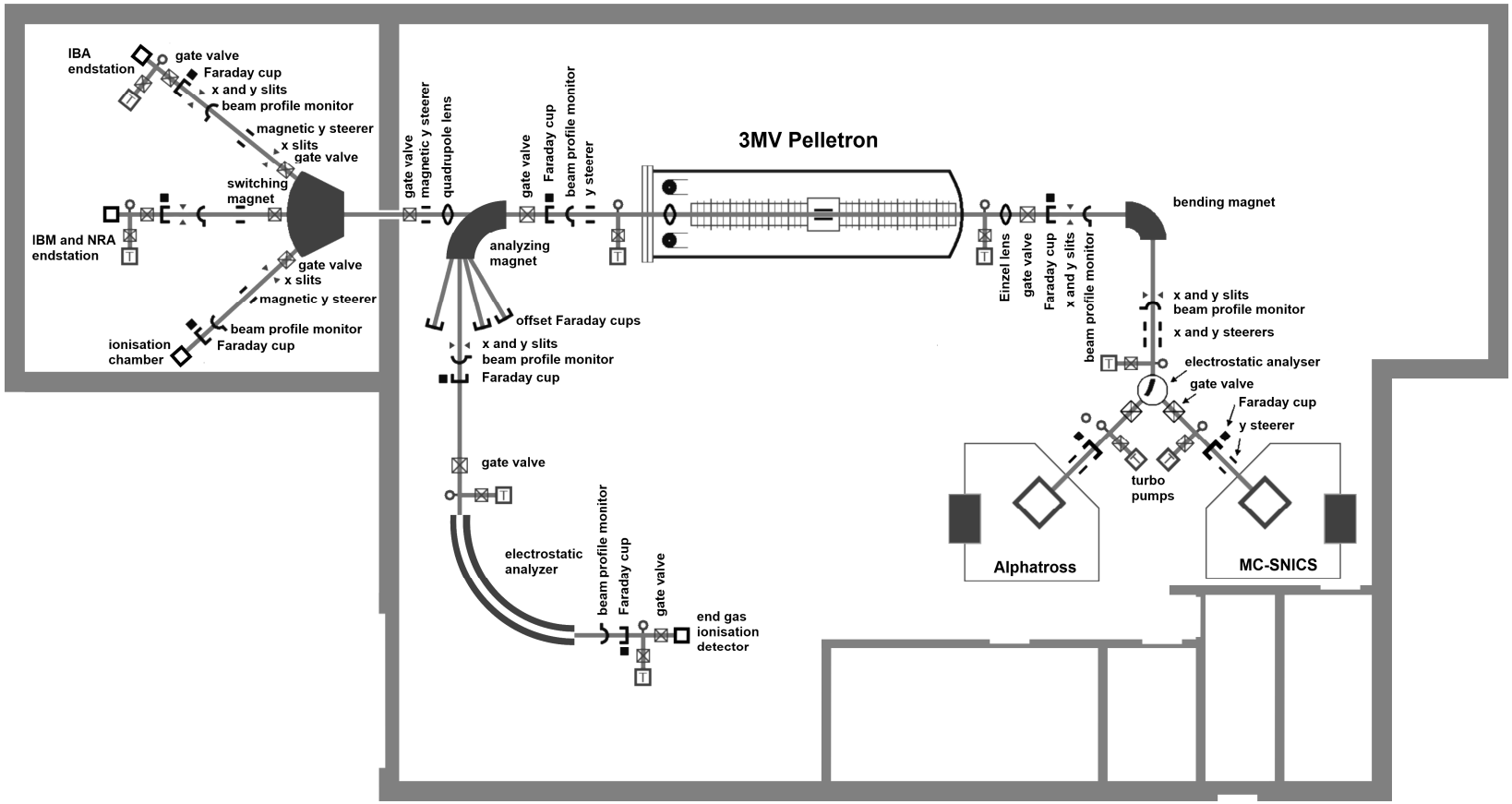

Fig. 7: A floor scheme of the CENTA laboratory with planned extensions

The planned AMS line should contain an electrostatic spectrometer and a gas ionization chamber detector. Faraday cups and offset Faraday cups with a proper ion beam and vacuum components will be installed as well. The extension in the forward ion beam direction should contain IBM and NRA techniques line with proper endstation chamber, the existing IBA line with chamber for these analyzes and modified existing line with added ionization chamber. The plans for IBA and IBM measurements incorporate a nuclear microscope, raster scan and biomedical station for material analysis. The proposed outlined laboratory completion should be able to fully manage research in wide area including nuclear physics, environmental physics, nuclear astrophysics, biomedical sciences and adjacent research. The purpose of the smaller laboratory room, where should be IBA and IBM measurements realized, is to afford a proper radiation protection for the staff executing these measurements. This shelter is covered with roughly one meter thick soil layer and has a double reinforced concrete walls. The idea of whole laboratory project was to achieve an environment where various experiments with different radiation exposures should be managed, more or less, at the same time. In this way, the AMS line will be separated from the environment with increased radiation, while the neutron and gamma-ray detectors will continuously monitor the radiation levels in the main laboratory where operators and scientific staff will carry out the measurements.

The detailed description of devices installed in the laboratory is given in the next sections.

3.1. Ion sources

The CENTA laboratory is equipped with 2 ion sources: Alphatross and MC-SNICS. The Alphatross is a radio frequency ion source designed to produce ions from gas or a mixture of gases. The MC-SNICS (Multi-Cathode Source of Negative Ions by Cesium Sputtering) is designed for ion production from solid material. Both sources are able to produce negative ions. Negative ions are necessary for tandem acceleration process which is described in section 3.5.

3.1.1. Alphatross

The structure of Alphatross was originally designed only for negative helium ions productions [Alph, 2011]. But with further upgrades it is capable of production variate of ions, e.g. H^-, NH^-, O^-. The principle of Alphatross operation for He ions is shown in the Figure 8.

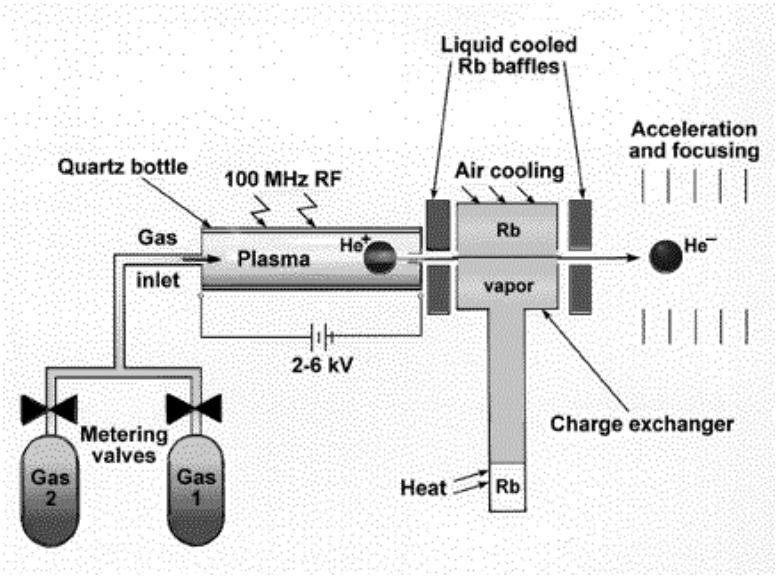

Fig. 8: The Alphatross operation principle for He ions production [Pelletron1, 2017]

An RF (radio frequency) ion source produces positive ions. A gas or gas mixture is bled into a quartz bottle; an RF oscillator connected to the quartz bottle dissociates the neutral gas. The frequency of 100 MHz is applied. A voltage difference (usually about 2-6 kV) is used to push the ions out of the chamber through the exit aperture, making a continuous beam. To produce a negative beam, the positive beam is immediately injected into a charge exchange cell with rubidium vapor. The rubidium is used due to its low

electron affinity. Positive He ions which pass through this vapor can easily pull more than one electron from rubidium and become negative. Rubidium is used also because the cross section for He negative ions production is higher compared to other elements. The charge exchange process efficiency is about 1–2 %. Negative He ions are consequently extracted into the beam line. Typical ion beam current from Alphatross is ~ 2mA.

3.1.2. MC-SNICS

This source is used for negative ion beam production from solid targets with masses ranging from lithium to transuranic elements. The condition for proper utilization of ion beam is that the target material must be able to form stable negative ions. The Multi-Cathode in its name means that this source is equipped with a rotary carousel for 40 target positions. The target material is pressed into small holders and placed into these 40 positions in the carousel. During the operation, the whole carousel is being held on positive potential, therefore the target material holders are usually denoted as cathodes. Hence the MC-SNICS is designed for rapid cathode change and precise, repeatable positioning without cathode exposure to air and keeping the high vacuum stable inside of the source. Negative ions are produced in cesium sputtering process. The principle is shown in the Figure 9.

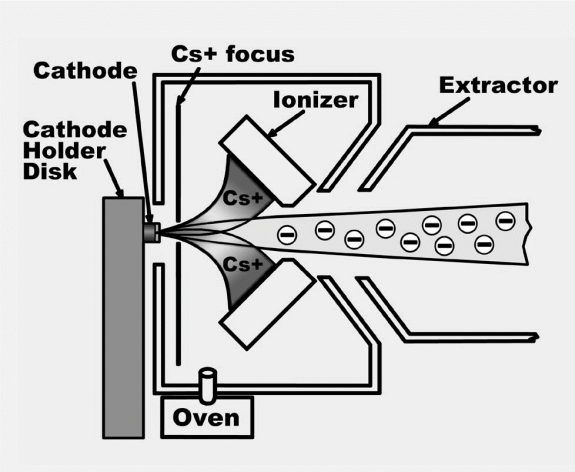

Fig. 9: The MC-SNICS operation principle for negative ions production [Pelletron2, 2017]

The primary parts of this source consist of cathode holder disk, oven with liquid cesium, ionizer, focusing electrode (Cs+ focus) and extractor electrode. Cesium is being heated up to ~200°C causing its evaporation. The vapor rises to small space between the

hot ionizer surface and cooled cathode wheel. Some amount of the cesium vapor condenses on the cathode wheel and the rest is thermally ionized on the ionizer surface. Positive cesium ions are than attracted by negative cathode potential (– 5 kV in standard operation). In the path from ionizer surface to the cathode surface these ions are accelerated and their energy is sufficient for material sputtering from the target material placed in the cathode. Some materials prefer to form negative ions in this sputtering process. But, there are certain materials which suppress negative ion formation and prefer to form positive ions or neutral particles. The design of the MC-SNICS takes this fact into account. Inside of the source, there is a small space close to the cathode surface where is the cesium vapor. Positive ions or neutrals can easily pick some electrons from this cesium because of low electron affinity of cesium and hence become negative. The extractor electrode which is held at high positive potential (~+16 kV) extract negative ions produced in the MC-SNICS and further ion optics devices accelerate them into the beam line.

3.2. Low energy part

Description of main devices installed among the ion sources and the accelerator is presented in this section. Specifically, the list of these main devices includes:

1.) Electrostatic analyzer
2.) Bending magnet
3.) Electrostatic steerers
4.) Einzel lens

3.2.1. Electrostatic analyzer

Electrostatic analyzer (ESA) is installed in the beam trajectory after the pre-acceleration of ions in the sources and it is used for beam selection from one of the sources. ESA operates on the principle of rotation table with 2 vertical electrodes. The table is capable of rotation in horizontal plane and has 2 positions; one for Alphatross and other one for MC-SNICS. The electrodes' curvature radius is 30 cm. A schematic view of ESA is illustrated in the Figure 10. The figure represents top view of the device. The vertical electrodes which determine the ions' trajectory are highlighted on purpose. The adjustable electrostatic potential of these electrodes enables to deflect ion beams of desired quality. In

this way, the ESA represents an energy filter. The separation of ions is guided by the *E/q* criterion (where *E* represents the energy and *q* the charge state of ion) for different ions coming out of the sources. The possible charge states from the sources can be 1^-, 2^-… but the majority of produced ions are in the 1^- charge state from both sources.

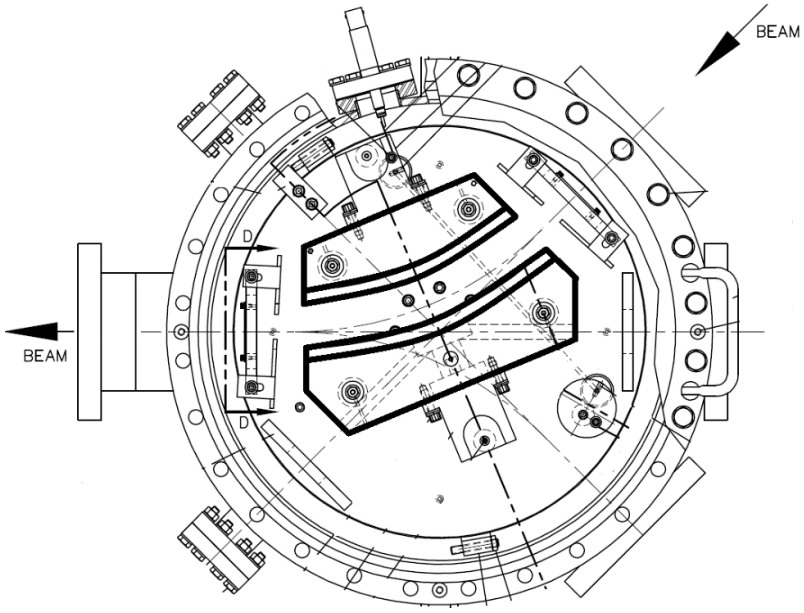

Fig. 10: A schematic top view of the Electrostatic analyzer (ESA) [ESA, 2011]

Vertical electrodes are highlighted for better orientation in the figure. Arrows represent the beam direction as shown.

3.2.2. Bending magnet

The most important device in the low-energy section represents a bending magnet (BM). It is a dipole magnet which deflects the ion beam to 90°. A uniform magnetic field, perpendicular to the ions' trajectory, causes a curvature of this trajectory. In this way, the BM represents a momentum filter. The ion separation is guided by *p/q* criterion (where *p* represents the momentum and *q* the charge state of ion) and thus the BM can be used for mass spectrometry. The distance between magnet poles is 4.8 cm, the curvature radius is 45.72 cm and whole magnet weights 2473 kg. Maximal electrical current in the coils is 96.3 A [Bend, 2011]. A schematic view of the BM is shown in the Figure 11. The poles are specially formed into shape (highlighted part in the figure) that meets the best performance results for ion trajectory deflection according to the manufacturer, the NEC.

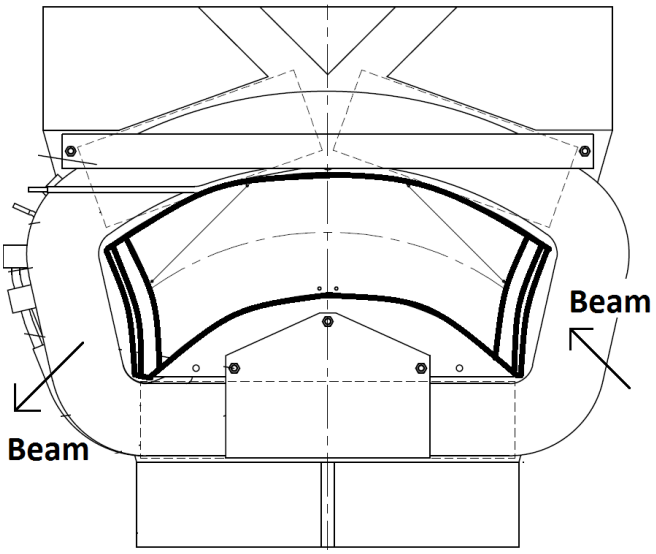

Fig. 11: A schematic top view of the bending magnet (BM) [Bend, 2011]

Magnetic pole is highlighted on purpose for better orientation. Arrows have been added for beam direction as shown.

3.2.3. Electrostatic steerers

In the beam line among the BM and ion sources, special devices for ion trajectory affection in horizontal and vertical direction are installed. These devices are called electrostatic steerers (ES). The name for these devices is really peculiar. Each device is able to deflect or "steer" the ion beam in a certain direction. The design of ES is quite simple. It consists of 2 parallel plane electrodes which are mounted in certain distance from each other. The space between the electrodes is supplied by an adjustable electrostatic potential and thus ions passing through the ES are forced to change their trajectory in this electrostatic field. Depending on the direction of electrostatic field intensity vector and the charge state of the ion the trajectory can be deflected into desired direction. A schematic view of ES is shown in the Figure 12. Two types of ES are installed in the low energy section; vertical steerers (for beam deflection in Y axis) and combined horizontal-vertical steerer (for beam deflection both in horizontal direction – X axis and vertical direction – Y axis). In the Figure 12, a scheme of the vertical steerer (ES-Y) is shown on the left side and a scheme of combined horizontal-vertical steerer (ES-XY) is shown on the right side. In the ES-XY, two pairs of planar electrodes are installed while they are 90° rotated along the

beam axis to each other. As can be seen in the floor scheme of CENTA laboratory (Figure 6), there are one and one ES installed among the sources and the ESA and one ES installed between the ESA and the BM. The ES which are installed between each source and the ESA is vertical (ES-Y) and the other one is combined for both directions (ES-XY).

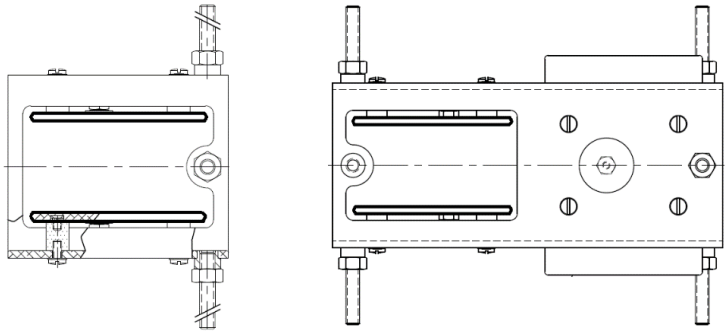

Fig. 12: A schematic side view of electrostatic steerers (ES) [ESXY, 2011]. On the left side the ES-Y scheme is shown, one is installed between the Alphatross and the ESA and another one between the MC-SNICS and the ESA. On the right side the combined ES-XY scheme is shown. This ES is installed between the ESA and the BM. The planar electrodes are highlighted on purpose in both cases.

3.2.3. Einzel lens

The ion beam before entering the Pelletron is passing through Einzel lens (EL) which are installed between the BM and the Pelletron (Figure 6). This device consists of three cylindrical electrodes which are mounted in a row along the beam axis. A longitudinal section view is shown in the Figure 13.

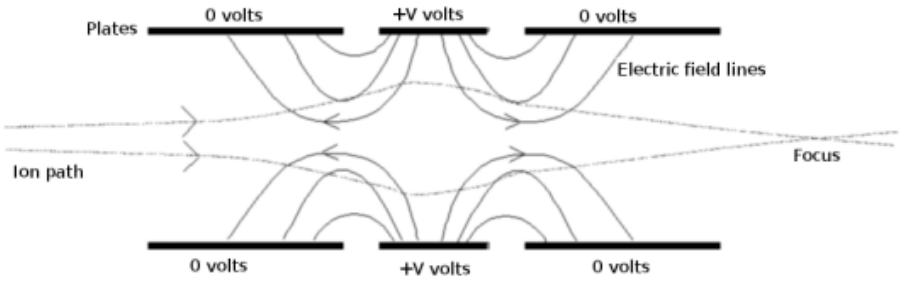

Fig. 13: A longitudinal section view of the Einzel lens installed in the laboratory [EL1, 2017]

The two outer electrodes are grounded while the middle one is being held on adjustable positive potential. Hence the electrostatic potential is symmetrical so ions' energy remains unchanged when they pass through such system. In the CENTA laboratory model Einzel

Lens EL 76-60 is installed. The maximal applied voltage on the middle electrode is 60 kV, inner diameter of electrodes is 76 mm and the length of the EL is 219 mm [EL2, 2011].

3.3. Ion beam monitoring devices

Along the whole beam line multiple different devices operate in order to monitor the ion beam. The ions produced in the ion sources form ion beam which has to pass through the pre-accelerating and accelerating system, consequently through the focusing and separation system and finally, in the end, these ions are either monitored or used for some application. Obviously, during this process, the features and characteristics of the ion beam variates because devices used for beam trajectory deflection, ions' acceleration and focusing affect the main features of the beam such as energy, intensity and shape, i.e., the cross section or the beam shape on the target surface. Depending on the ions which are subject of interest, the whole acceleration system has to be tuned with individual approach to settings of beam features affecting devices. For this purpose Faraday cups and beam profile monitors are installed along the beam line to monitor and record these changes in ion beam qualities.

3.3.1. Faraday cups

The Faraday cup (FC) is a device formed by conductive metal cylinder (alternatively cone) designed to capture charged particles in vacuum. Incident charged particles cause induction of electric current in the volume of (FC). Via precise measurement of this current the intensity of ion beam can be calculated or, as in common practice, the intensity of ion beam can be directly used in Amperes [Wiedemann, 2015] (usually mA and less). In the CENTA laboratory two models of FCs are installed: FC50 and FC18.

Faraday cup model FC50

This model consists of cylinder with a grounded entering aperture, an electron suppression electrode and a tantalum collector. A schematic view of this model is shown in the Figure 14; a view from the beam direction and a top view of the device. The position of the FC is controlled with an air pneumatic system guided from the computer. This system simply retracts or inserts a metal bar which holds the FC, so the cylinder moves in or out of the beam axis. The electron suppressor is designed for suppression of secondary electrons emitted from the cylinder since the ion beam produces these electrons when it hits the

surface of the FC. The suppressor's diameter is larger than the diameter of FC's entering aperture, so it does not capture the ions which are measured in the FC. The negative suppressor potential prevents the emission of secondary electrons; suppressor of this model is powered by -200 V power supply. The electric current induced in the cylinder corresponds then to the intensity of the ion beam. The amount of particles depends on the presented charge state of ions captured by the FC.

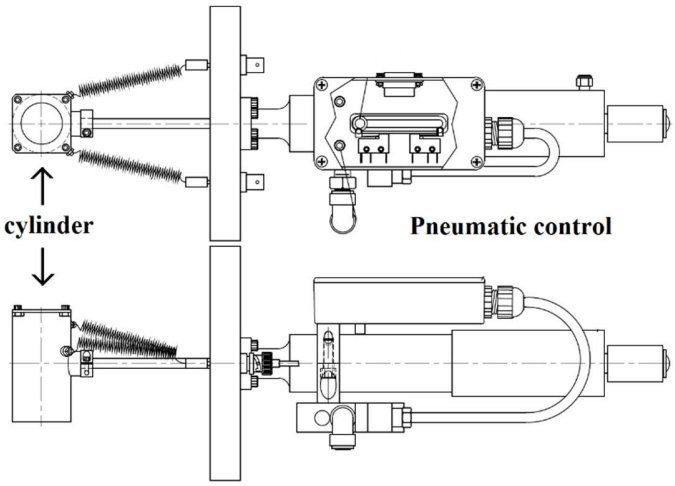

Fig. 14: A front and top view of Faraday cup model FC50 [FC50, 2011].The front view is in the beam direction. The FC is moved in or out of the ion beam with an air pneumatic controller. The labels were added for reader's better orientation in the figure.

Faraday cup model FC18

In contrast with the previous model, model FC18 consists of tantalum cone for capture of charged particles. The conical shape of the FC is designed in such way that the major part of the surface is exposed to the incident ion beam while avoid melting of tantalum with intense radiation. This model is illustrated in the Figure 15. The cone is electrically insulated from the cooling system which is realized with circulation of cooled water in a spiral tube wrapped around the cone. This cooling coil absorbs the heat produced by incident beam. The position of the cup is controlled with air pneumatic system mounted on the top of the FC. The difference compared with FC50 model is that this model is positioned into the beam axis via partial rotation around axis above the FC. On the left side of Figure 15 is shown the view from the beam direction and the FC. The cone is moved out of the beam axis by movement to the left (pneumatic system retracts the metal bar which

hold the cone). To move the cone into the beam axis, the system inserts the bar and the cone moves to the right (from the view in the Figure 15). The ion beam enters the cone through a grounded molybdenum aperture. The diameter of this aperture is smaller than the diameter of suppressor electrode which has the same function as in model FC50. The FC18 suppressor installed in the laboratory is powered by -400 V power supply.

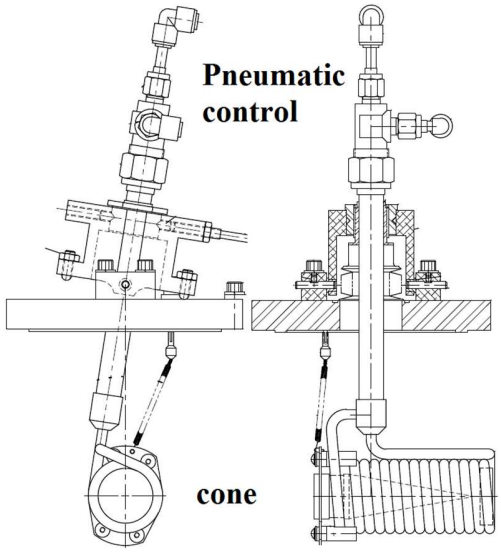

Fig. 15: A front and side view of Faraday cup model FC18 [FC18, 2011] 4The front view is in the beam direction. In the side view the beam is incident from the left. The FC is moved in or out of the ion beam with an air pneumatic controller (movement to the left or right, see text). The labels were added for reader's better orientation in the figure.

3.3.2. Beam profile monitors

This devices are installed along the whole beam line to monitor the position and the intensity of ion beam in horizontal (denoted as X axis) and vertical (denoted as Y axis) direction. The beam profile monitor (BPM) is able to measure these qualities while the beam is passing through the device. It is possible due to its design which allows beam to pass without significant change. The main part of the BPM is a wire bowed into 45° spiral which is rotating along the spiral axis with certain frequency. In the laboratory two models of BPMs are installed: BPM81 and BPM80. The BPM81 model rotates with frequency of 18 cps with radius of 2.25 cm; the BPM81 model rotates at 19 cps frequency with 2.7 cm radius [BPM, 2011]. The very important feature of the BPM is a proper mounting on the beam line. The device has to be mounted in a 45° angle in order to provide proper

functionality. The scheme of BPM is shown in the Figure 16. The rotating wire cuts the beam axis in two orthogonal planes while collecting information about X, in one section and then about Y axis, in the next section. Secondary electrons' electric current induced in the wire by passing ion beam is measured and recorded. In a properly calibrated oscilloscope two signals appear: one for X and other one for Y axis. This information is consequently transformed into the horizontal and vertical profiles of the beam.

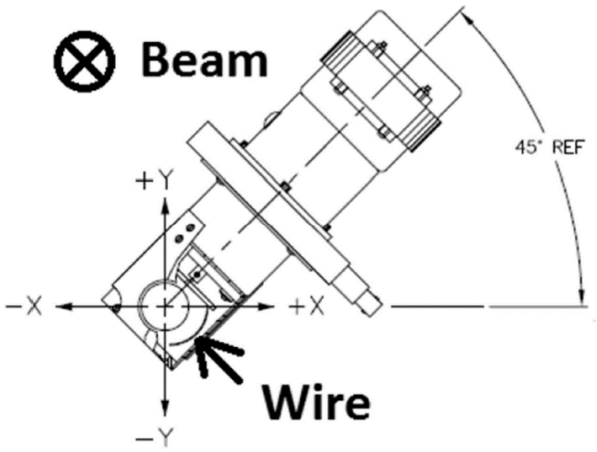

Fig. 16: A schematic view of BPM [BPM, 2011]. Information about beam direction and label for wire were added on purpose. The whole device is mounted on the beam line at 45° angle.

A final exemplary BPM output is shown in Fig. 17.

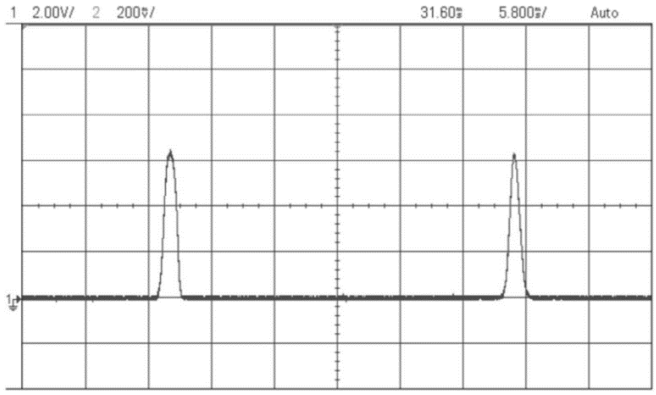

Fig. 17: An oscilloscope BMP output of ion beam profile [Povinec, 2015]. On the left side Y profile (vertical) and on the right side X profile (horizontal) are displayed. Specifically, the $^{9}Be^{2+}$ ion beam at 7.1 MeV energy after focusing is shown. One square of the grid represents 10 mm.

3.4. The Pelletron accelerator

The superior device installed in the CENTA laboratory is a linear tandem electrostatic accelerator Pelletron model 9SDH-2 with maximal terminal electrode voltage 3 MV. Inseparable component of the Pelletron is a stripping column in the middle of the acceleration tube. The column if filled with a stripping gas which provides charge exchange among accelerated ions and this strips gas molecules. Electrons are being stripped out from the originally negative ions so these ions are becoming positive. This is the core of tandem acceleration; negative ions are in the first half of the acceleration tube attracted by positive terminal electrode potential and consequently, after successful stripping of electrons, these ions are repelled by the same positive terminal electrode potential. The energy yield from tandem accelerators is hence doubled compared to single-stage accelerators for the same potential of terminal electrode. Presently, the stripping column is filled with a nitrogen gas. The column is equipped with a step valve and two turbo-molecular pumps. The step valve provides delicate control of pressure what is necessary for stripping process. The pumps are mounted on the sides of the column and they maintain a circulation of nitrogen inside of the column. Another purpose of the pumps is to prevent nitrogen escape the stripping column what would lead to degradation in vacuum in the beam line and possible automatic shutdown of the system in a case when the pressure in the beam line vacuum rises above certain level. The charging of terminal voltage is provided by circulating chains consisting of small pellets. The principle with a chain detail is shown in Fig. 18.

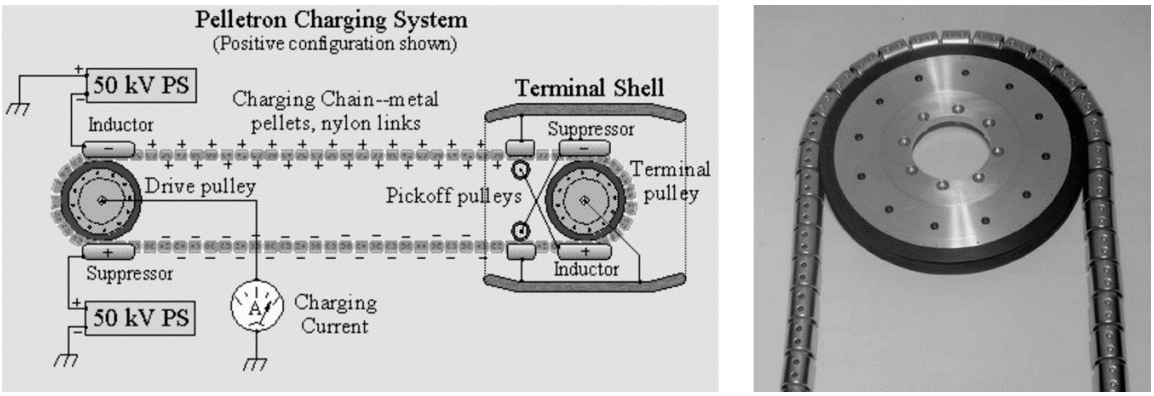

Fig. 18: Charging process scheme and detail of a charging chain [Pelletron3, 2011].

The charging chains are made of metal cylinders (pellets) connected by insulating nylon links. The pellets are charged by an induction scheme that does not use rubbing contacts or corona discharges. For a positive terminal Pelletron, the negatively-charged inductor electrode pushes electrons off the pellets while they are in contact with the grounded drive pulley. Since the pellets are still inside the inductor field as they leave the pulley, they retain a net positive charge. The chain then transports this charge to the high-voltage terminal, where the reverse process occurs. When it reaches the terminal, the chain passes through a negatively-biased suppressor electrode which prevents arcing as the pellets make contact with the terminal pulley. As the pellets leave the suppressor, charge flows smoothly onto the terminal pulley, giving the terminal a net positive charge. The motors which provide the chains' movement are supported on movable platforms which are counterweighted, automatically providing proper chain tension [Pelletron3, 2011]. The accelerator tube is placed in a pressure tank with 1.22 m diameter and 5.64 m length. This vessel is filled with an insulating gas, specifically sulfur hexafluoride (SF_6) at pressure of several bars (usually 5 bars of SF_6 is used). This gas has excellent insulating qualities, hence it is used for suppression of undesirable terminal electrode discharge. On the other hand, SF6 is a highly potent greenhouse gas so a cryogenic vacuum system is used for the manipulation and storage of this gas during the Pelletron maintenance.

3.5. Focusing and analyzing beam line

Accelerated ion beam leaves the Pelletron and proceeds to the focusing beam line. The principal device in this section is the triplet of magnetic quadrupoles (QP) that focuses the ion beam using different magnetic intensities applied among the poles of the triplet in QP. Consequently, the focused ion beam passes through a dipole magnet which provides the ion beam trajectory deflection into desired direction. The dipole magnet, called switching magnet (SM), is designed for 7 possible directions; 1 forward, 3 to the left and 3 to the right side. In terms of angles, these positions are 0°, ± 15°, ± 30° and ± 45°, with respect to the beam axis. At present, 2 channels are being used in the laboratory. Both are oriented on the left side in direction of passing beam (Figure 6). A PIXE/PIGE beam line is installed at 15° position and a channel used for calibration and testing is installed at 45° position. The PIXE/PIGE chamber is used for this measurements and the chamber itself will be explained

in the next section. For ion beam positioning in vertical direction additional magnetic steerers are installed. Faraday cups and BPMs are installed in this section as well for ion beam monitoring. Details of these devices are given in previous sections. Next sections give more information about the QP, SM and magnetic steerers.

3.5.1. Triplet of magnetic quadrupoles

The device comprises of three magnetic quadrupoles mounted in common rack. The magnetic field formed by a magnetic quadrupole (QP) is convenient for beam focusing. The intensity of such field rapidly rises with increasing distance in direction from the longitudinal axis of QP. The ion beam passing through the QP is being focused in one axis and defocused in axis perpendicular to the previous one. Thus, in practice, multiple QPs are usually installed in a row while they are 90° rotated along the beam axis to each other. The focusing of ion beam depends on the intensity and various strength of magnetic field formed by individual quadrupoles. Depending on the momentum of ions forming the beam, the beam diameter can be focused down to ~ mm. Some of various ion beam applications demand defocused beam which is incident on a larger area of the specimen. With proper settings of QPs the defocusing effect can be lead to beams of large diameters (1-2 cm). This technique is limited by construction of beam line and also by factors that rises from utilization of different devices in next steps after defocusing. The QP triplet installed in the CENTA laboratory is described later into details (chapter 5).

3.5.2. Analyzing magnet

The next step in AMS or IBA technique is selection of accelerated ions which undergo focusing process in the QP. For this purpose a dipole analyzing magnet is installed as can be seen in the Figure 6. This magnet was designed with 7 possible exiting beam lines. At present, two of them are used for research in the laboratory. The magnet itself is called switching magnet (SM) for its obvious functionality of switching among possible channels. The distance of magnet poles is 3.18 cm, the pole edge radius is 46.63 cm, and radius of curvature for 45° channel is 60.93 cm, 90.09 cm for 30° channel and 178.64 cm for 15° channel. The total weight of magnet with coils is 2161 kg. The magnet is designed for maximal 200 A of electric current in the coils [Switch, 2011]. The scheme of the SM is

shown in the Figure 19. More details about the SM are given in the chapter 5 which describes the ion beam trajectory simulations in the QP and SM.

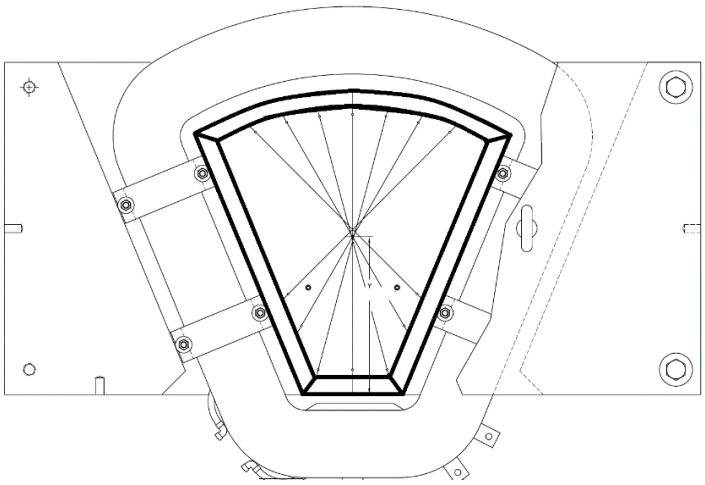

Fig. 19: A schematic top view of the SM [Switch, 2011]. The pole boundaries are highlighted on purpose for better orientation in the figure. In this view, the ion beam passes through the SM in upward direction.

3.5.3. Magnetic steerers

Two magnetic steerers (MS) are installed in the analyzing and focusing beam line. The scheme is shown in the Figure 20. As can be seen in this figure, the MS are installed from the outer side of the beam line. MS comprises of two poles (vertical plates in the figure) and corresponding coils. It “sits” on the beam line on four screws and the orientation of MS can be rotated around the beam line. The magnetic field strength depends on the electric current in the coils. This current is controlled by the command computer in the laboratory. This design is very convenient, because it gives opportunity to change the position of MS, if needed, within few minutes. Depending on its installation, various ion beam deflection can be achieved. Under standard circumstances, a horizontal or a vertical deflection is desired, so a corresponding installation of MS is utilized. At present, both MS are installed as shown in the Figure 20, so the deflection of trajectory is in the vertical direction.

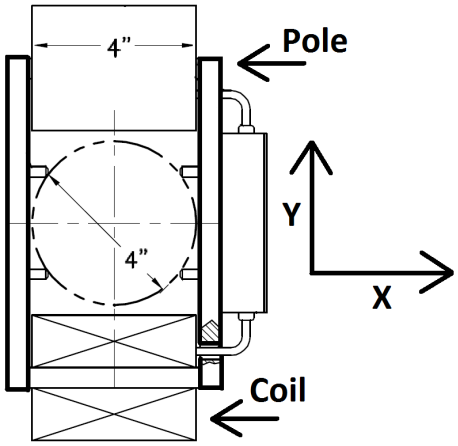

Fig. 20: A schematic view of the MS [MS-Y, 2011]

Magnetic poles are highlighted for better understanding of deflection process. In this mounting option, the magnetic field vector is horizontal, charged particle moves toward (or away from) the figure thus the Lorentz force vector is vertical, pushing the charged particle down or up (depending on the particle’s charge sign and the magnetic field vector orientation – left or right). Labels for pole, coil and horizontal and vertical directions were added. The dimensions in the figure are in inches.

4. Pelletron transmission efficiency measurements

The principal device of the CENTA laboratory is linear tandem accelerator Pelletron with two ion sources and several ion optics devices for ion beam manipulation. For proper functionality of the whole system many calibration and optimization measurements were elaborated. Tandem accelerator transmission efficiency for various ions is one of the key features of this system. Further development of ion beam applications depends on the determination of this characteristic feature. For tandem accelerators is crucial the usage of negative ions which are being stripped in acceleration process inside the Pelletron.

Tandem acceleration in Pelletron proceeds in two steps: firstly, negative ions are accelerated towards the positive potential of the terminal electrode (where ions change their charge in the stripping process) and secondly, positive ions are accelerated by positive potential of the terminal electrode. In this way, the energy gained in tandem acceleration is doubled compared to a single acceleration process using the same potential voltage on terminal electrode. Stripping is being done by introducing either foils or stripper gas into acceleration tube inside the volume of the terminal electrode, which is held on a positive potential. The quality of the stripping process determines the amount of ions, which change their electric charge from negative to positive. CENTA's Pelletron system incorporates gas-stripping technology with nitrogen as stripper gas. Negative ions are produced in ion source where they gain certain injection energy (tens of keV). Using ion optics devices for beam transmission through the system, certain type of ions can be selected and injected into the Pelletron. These ions are accelerated to energies of several MeV, separated using high-energy ion optics devices installed in the focusing and analyzing beamline and detected in the end of the beam line detector.

The quality of stripping process is defined by transmission efficiency. In literature it is possible to find different terms such as stripping efficiency or stripping yield [Steier, 2000], or charge state fraction [Winkler, 2015], or transmission efficiency [Maxeiner, 2015], but all of them describe the same quantity. Transmission efficiency is used for description of stripping process effectivity for different ions and different charge states of a certain ion. Negative ions enter stripping channel, i.e., volume of beam line which contains stripper gas. Via interactions with gas molecules, electrons are being stripped from negative ions so

the ions become positive. Depending on the ion mass, the stripper gas pressure and the energy of ions, various final charge states of positive ions are being accelerated in the second phase of the tandem acceleration process. Consequently, ions gain various amount of acceleration so they are leaving the Pelletron at different energies. Knowledge of the stripping process quality is very important for analysis of ions and for further applications.

Pelletron is designed for maximal terminal voltage of 3MV. All of the measurements were carried out for 6 values of terminal voltage: 1.5 MV, 1.8 MV, 2.1 MV, 2.4 MV, 2.7 MV and 3.0 MV. Unfortunately, some of the results are misleading, since the position of Pelletron was changed. During the time period from the laboratory establishment it was found out that the position of accelerator shifted in downward direction. One of possible explanations can be that the floor underneath the accelerator was pressed by its weight. More details are given in the end of this chapter.

4.1. Transmission efficiency calculation

The transmission efficiency was determined for ^{1}H, ^{4}He, ^{9}Be and ^{12}C ion beams. Protons and helium ions were produced in Alphatross, beryllium and carbon ions were produced in MC-SNICS (details in chapter 3.1.). The ions' injected energy from the sources was set to 52 keV for ^{1}H and ^{4}He and 61 keV for ^{9}Be and ^{12}C. Pelletron is designed for maximal terminal voltage of 3MV. Most of the measurements were done for 6 values of terminal voltage: 1.5 MV, 1.8 MV, 2.1 MV, 2.4 MV, 2.7 MV and 3.0 MV.

For Pelletron transmission efficiency determination we measured intensities of ion beams with Faraday cups before the acceleration in the Pelletron (at a low energy side) and after the acceleration at the end of the beam line. Consequently, for the transmission efficiency calculation we used the equation (1.):

$$T = \frac{FC05/n}{FC02}\ 100\ [\%] \qquad (1.)$$

where the *FC05* is the beam electric current at the end of the beam line measured by Faraday cup, denoted as FC05, the *n=1, 2, 3 …* represents the charge state of ions in the analyzed beam, and *FC02* is the beam electric current measured by Faraday cup, denoted as

FC02, before the acceleration. Our aim was to determine the dependency of the transmission efficiency on the gas pressure in stripping channel of the Pelletron.

The pressure of stripping gas was slowly increased in several steps from the starting point at 2 μbar up to the end point at 70 μbar. For each value of this pressure we measured values of electric currents in Faraday cups *FC02* and *FC05* for calculation of transmission efficiencies. Two approaches were used for these measurements. Some measurements were performed manually and some were performed using scripts. Manual measurements contain less measured points compared to the script measurements. The script controls the pressure level (by slowly valve opening in the stripping column) and continuously record values from corresponding Faraday cups in the whole range of stripper gas pressure. In the manual measurements, the pressure was changed manually by valve opening and measuring values from Faraday cups after the pressure stabilization. Depending on the current gas pressure in the stripping column, the measured points were smoother for low pressure levels up to ~ 15 μbar, becoming scattered to the end of monitored gas pressure region. For script measurements this fact is still valid, but less unambiguous because the amount of measured points is much higher compared to the manual measurements.

4.2. Transmission efficiency for ^{1}H ion beam

Beam of ^{1}H ions was produced in the Alphatross ion source. Negative H^- ion beam was extracted from this source with energy 52 keV and passed through the accelerator. The energy of accelerated $^{1}H^+$ ions was calculated using the equation (2.):

$$E = E_i + (n + 1)\, e\, TV \qquad (2.)$$

where E_i represents the injection energy of ions entering the accelerator, n is the charge state of accelerated ions, e is the elementary charge and TV is the terminal voltage. Since the protons can reach only 1+ charge state, the equation (2.) is quite simple and protons' energy equals simply to double the TV multiplied by e plus injection energy. Values of total gained energy of accelerated $^{1}H^{1+}$ ions are listed in Table 1.

Terminal Voltage (MV)	1.500	1.800	2.100	2.400	2.700	3.000
$^{1}H^{1+}$ Total energy (MeV)	3.052	3.652	4.252	4.852	5.452	6.052

Table 1: Total energy of accelerated $^{1}H^{1+}$ ion beam for individual values of terminal voltage

The transmission efficiency was calculated using equation (1.) with charge state n = 1 for monitored $^{1}H^{1+}$ ion beam. Stripper gas pressure dependency of $^{1}H^{1+}$ transmission efficiency is shown in next figures. The measurements were performed using script, thus the amount of measured points reaches ~ 100. The uncertainties were calculated using 2 % uncertainties of Faraday cups.

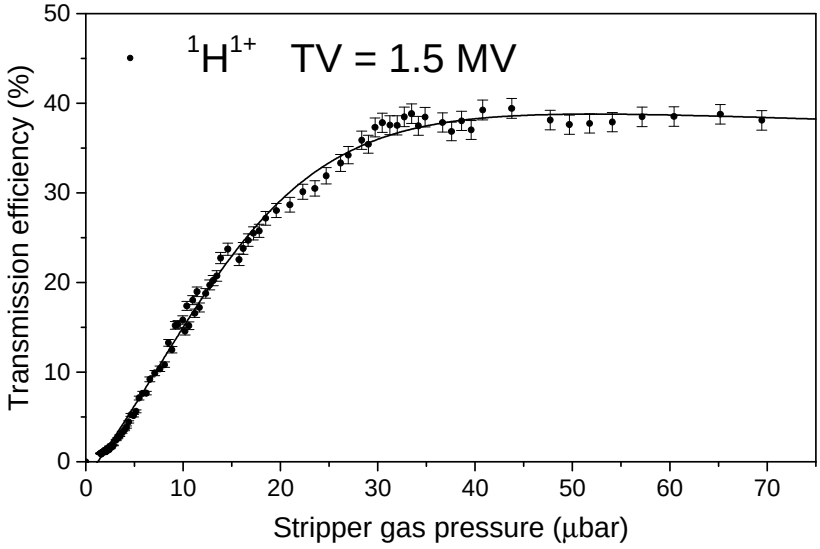

Fig. 21: $^{1}H^{1+}$ Transmission efficiency for 1.5 MV terminal voltage

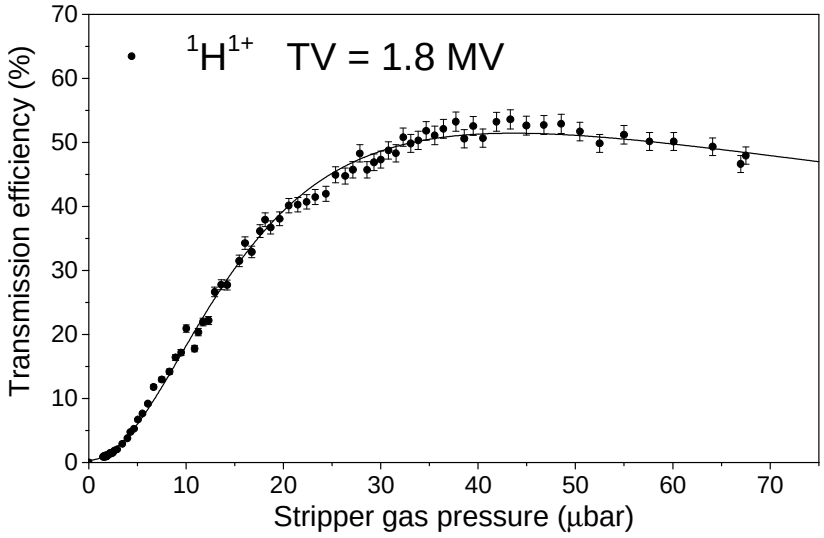

Fig. 22: $^1H^{1+}$ Transmission efficiency for 1.8 MV terminal voltage

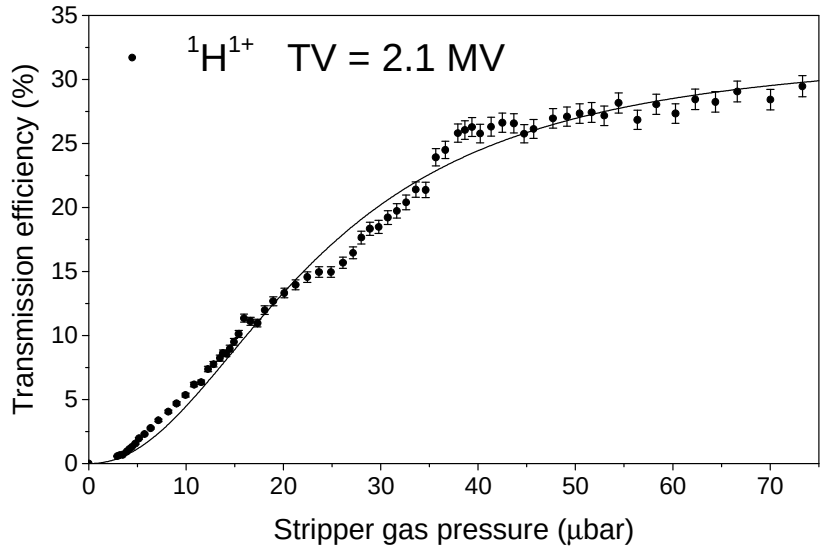

Fig. 23: $^1H^{1+}$ Transmission efficiency for 2.1 MV terminal voltage

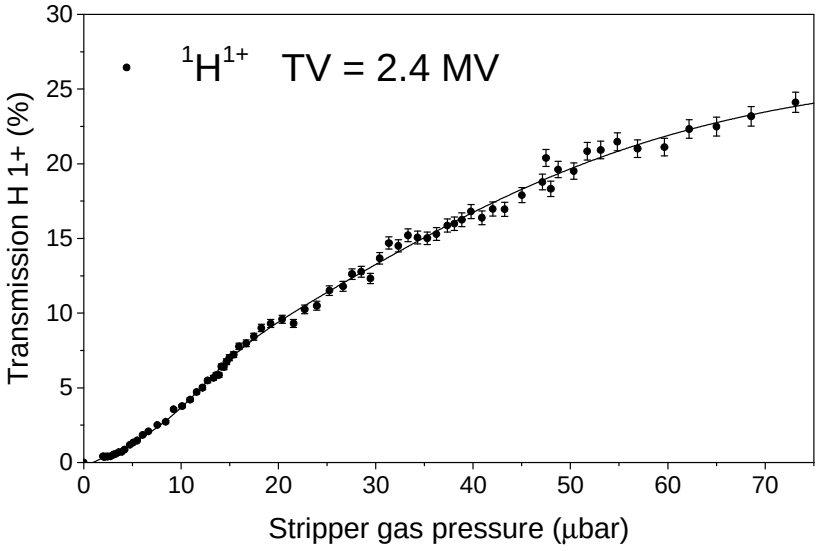

Fig. 24: $^1H^{1+}$ Transmission efficiency for 2.4 MV terminal voltage

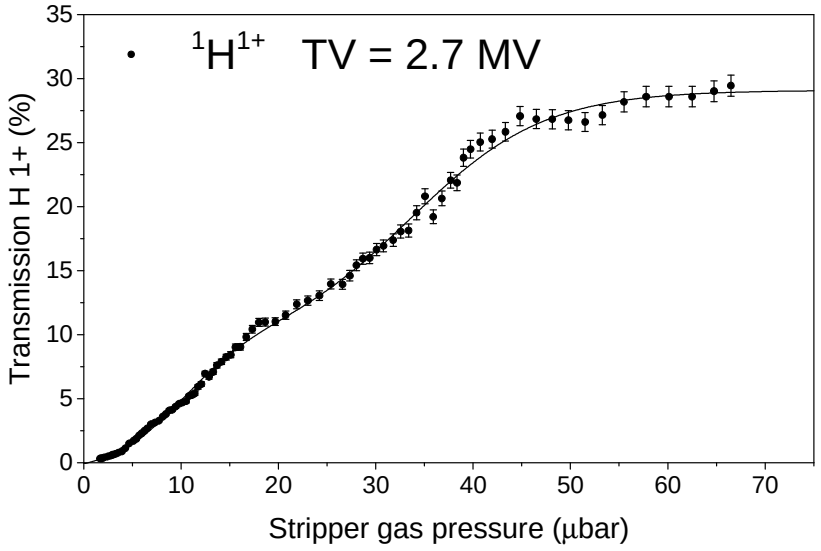

Fig. 25: $^1H^{1+}$ Transmission efficiency for 2.7 MV terminal voltage

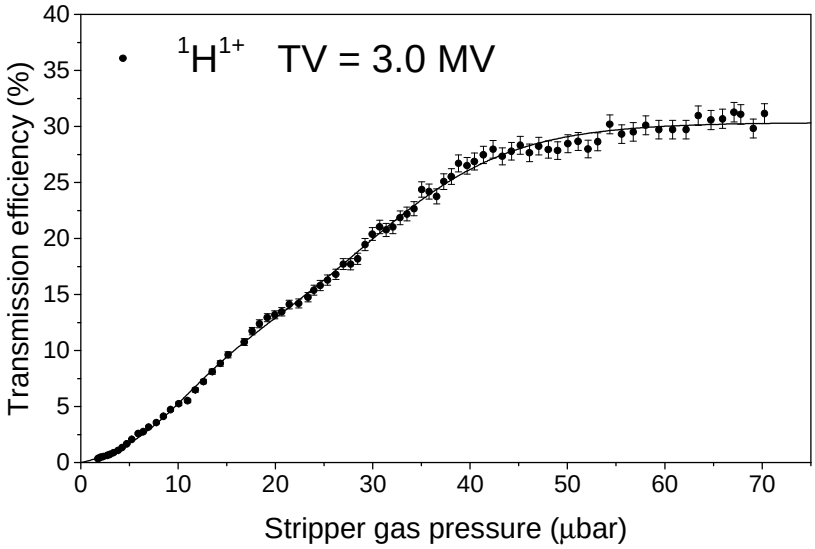

Fig. 26: $^1H^{1+}$ Transmission efficiency for 3.0 MV terminal voltage

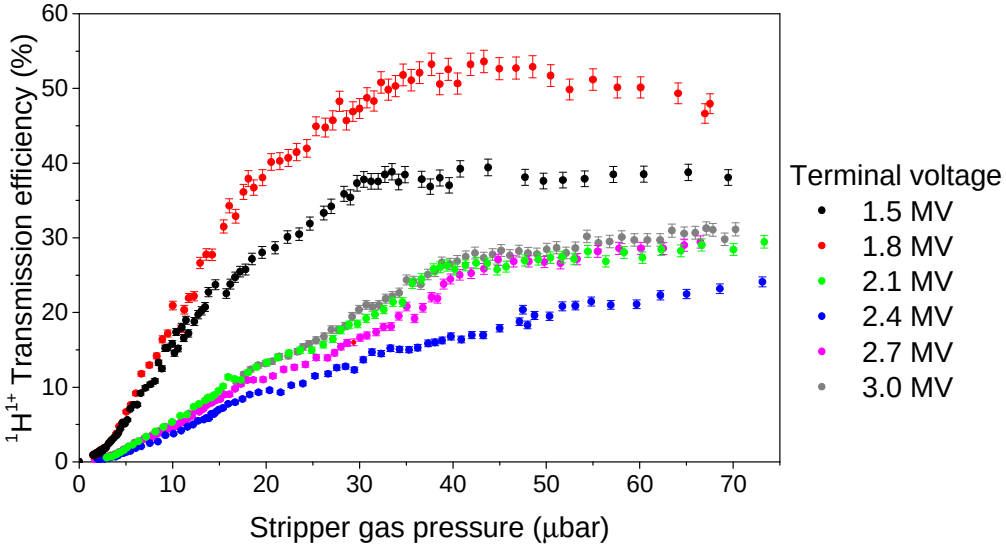

Fig. 27: $^1H^{1+}$ Transmission efficiency for all measured terminal voltages

As can be seen in the Figures 21 - 27, a strong transmission efficiency dependency on the stripper gas pressure was observed. In some measurements, especially at the terminal voltages 2.1 MV and 2.7 MV (Fig. 23 and Fig. 25), strange bumps occurred at 20 µbar and 40 µbar pressures. A possible explanation could be that there was some instability in the stripping column. The stripping gas pressure in the column is not equally distributed.

Therefore, there can exist for some trajectories of ions (beam shifts in mm) a space where this difference causes instability in the stripping process and final efficiency variates.

A much more disturbing result is in comparison of $^{1}H^{1+}$ transmission efficiencies for all measured terminal voltage values (Fig. 27). The assumption is that the transmission efficiency for one value of stripper gas pressure, e.g. for 30 μbar, should show some smooth dependency on the terminal voltage. For script measurements performed in the laboratory no such dependency was observed. The values of transmission efficiency in Fig. 27 are disarranged considering the assumptions.

4.3. Transmission efficiency for ^{4}He ion beam

Beam of ^{4}He ions was produced in the Alphatross ion source. Negative, He^{-} ion beam was extracted from this source with energy of 52 keV and it passed through the accelerator (the injection energy conditions were the same as for the $^{1}H^{-}$ ion beam). The energy of accelerated ^{4}He ions was calculated using the equation (2.). $^{4}He^{-}$ ions passed through the stripping column and two charge states of accelerated ions were observed: $^{4}He^{1+}$ and $^{4}He^{2+}$. Values of total energy for each ^{4}He charge state are listed in Table 2.

Terminal voltage (MV)	1.500	1.800	2.100	2.400	2.700	3.000
$^{4}He^{1+}$ Total energy (MeV)	3.052	3.652	4.252	4.852	5.452	6.052
$^{4}He^{2+}$ Total energy (MeV)	4.552	5.452	6.352	7.252	8.152	9.052

Table 2: Total energy of accelerated $^{4}He^{1+}$ and $^{4}He^{2+}$ ion beams for individual values of terminal voltage. The values were calculated according to the equation (2.)

The transmission efficiency was calculated using equation (1.) with charge state $n = 1$ and $n = 2$ for monitored $^{4}He^{1+}$ and $^{4}He^{2+}$ ion beams. Stripper gas pressure dependency of ^{4}He transmission efficiency is shown in next figures. Each figure contains values for both charge states. Sum of these values for individual stripper gas pressure values is denoted as "total". The measurements were performed using script, thus the amount of measured points is similar to $^{1}H^{1+}$. The uncertainties were calculated using 2 % uncertainties of Faraday cups.

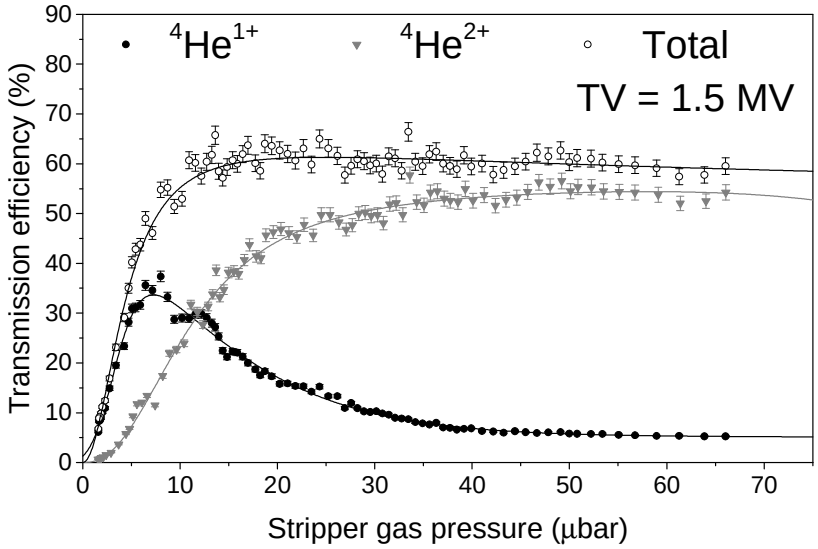

Fig. 28: $^4He^{1+}$ and $^4He^{2+}$ Transmission efficiency for 1.5 MV terminal voltage

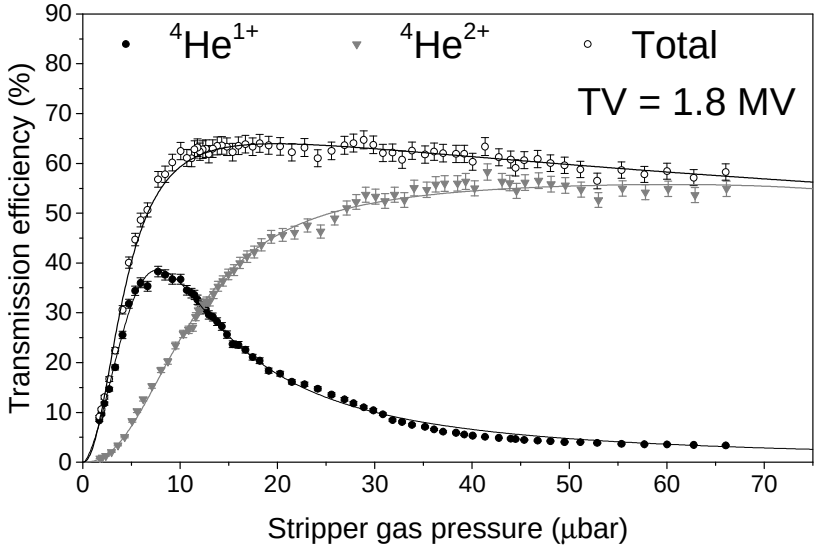

Fig. 29: $^4He^{1+}$ and $^4He^{2+}$ Transmission efficiency for 1.8 MV terminal voltage

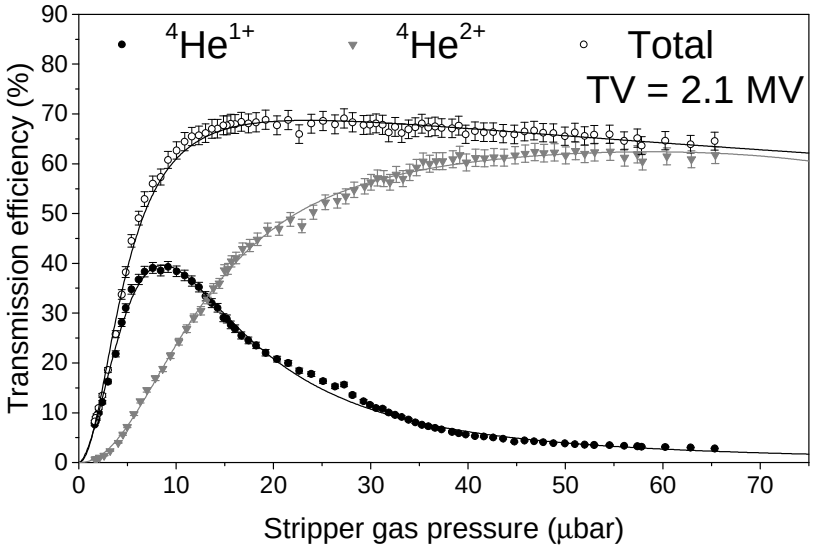

Fig. 30: $^4He^{1+}$ and $^4He^{2+}$ Transmission efficiency for 2.1 MV terminal voltage

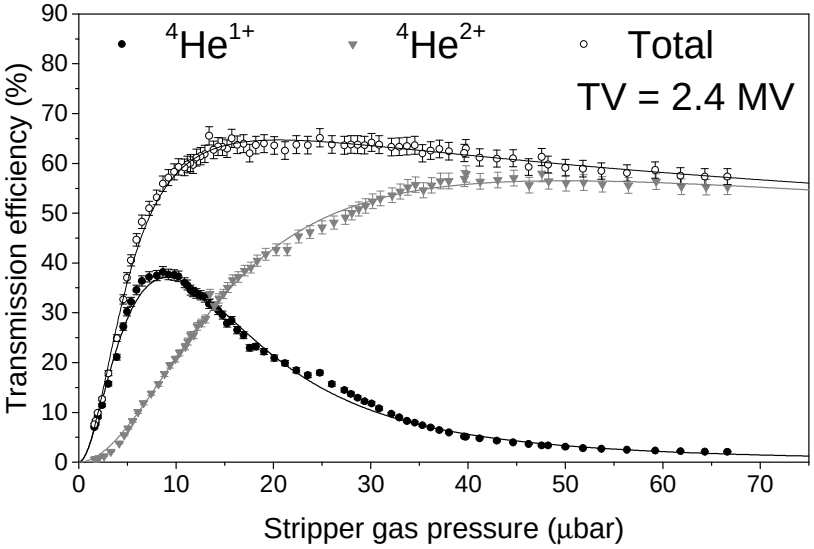

Fig. 31: $^4He^{1+}$ and $^4He^{2+}$ Transmission efficiency for 2.4 MV terminal voltage

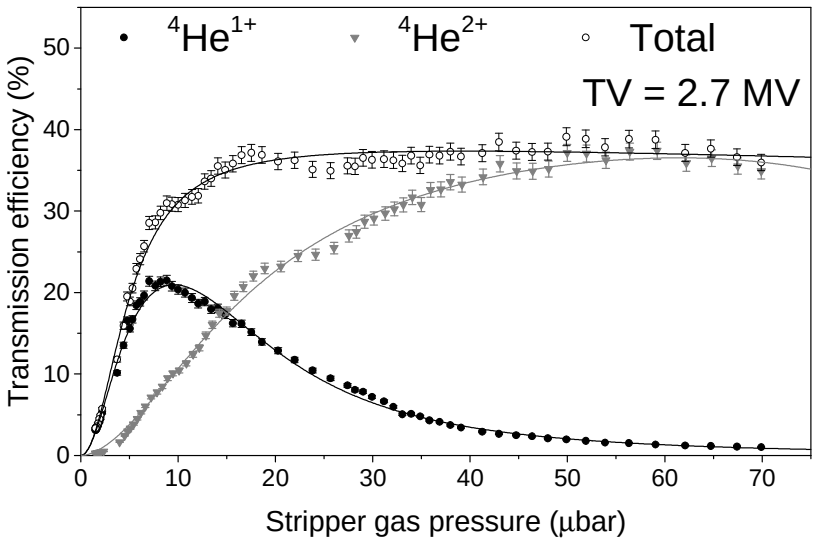

Fig. 32: $^4He^{1+}$ and $^4He^{2+}$ Transmission efficiency for 2.7 MV terminal voltage

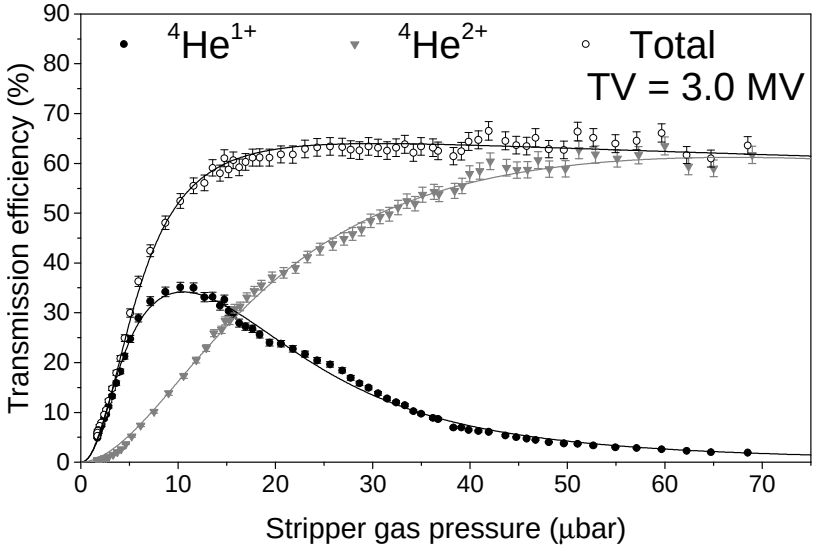

Fig. 33: $^4He^{1+}$ and $^4He^{2+}$ Transmission efficiency for 3.0 MV terminal voltage

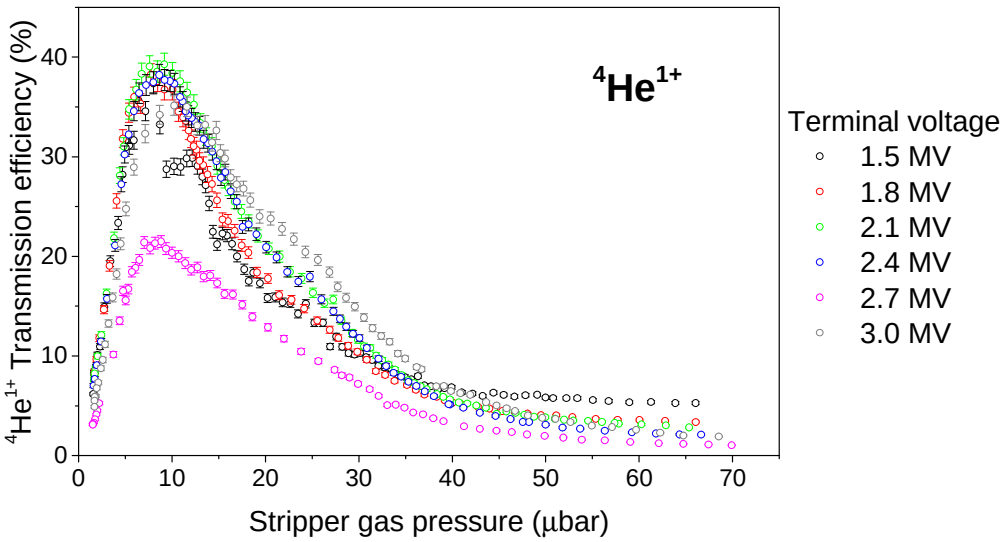

Fig. 34: $^4He^{1+}$ Transmission efficiency for all measured terminal voltages

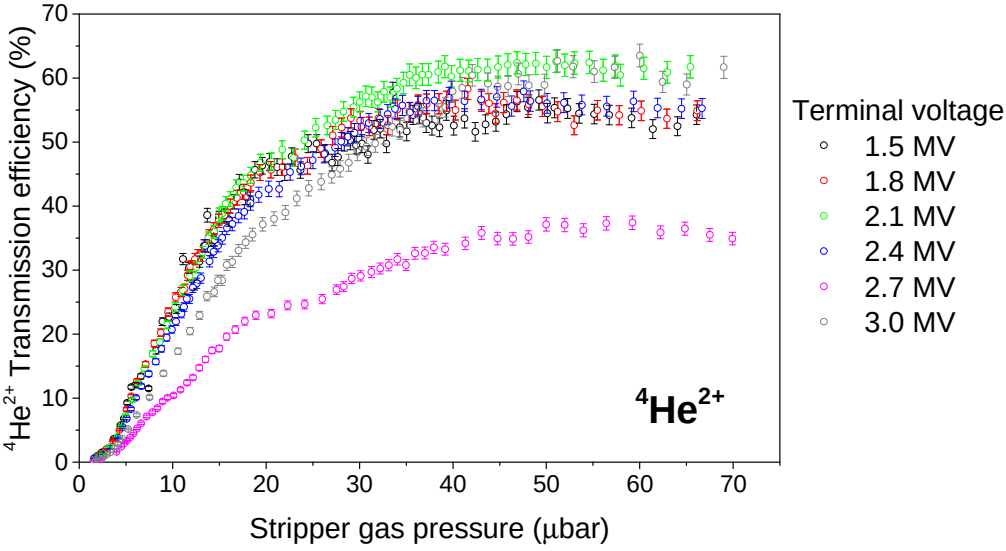

Fig. 35: $^4He^{2+}$ Transmission efficiency for all measured terminal voltages

First of all, the results for 2.7 MV terminal voltage seem to be incorrect. The assumption is that there was some instability in the analyzing beamline during this measurement. This instability pulled down values from Faraday cup FC05 causing low

transmission efficiency calculation results (see equation 1). A possible explanation could be that the ion beam trajectory was shifted, thus ions could not reach the Faraday cup. This shift could be caused by different setting of ion optics. Individual measurements were performed in a way that for each terminal voltage measurement, the ion optics settings were different. It seems, that the settings for 2.7 MV were done incorrectly, therefore the transmission efficiency drops. Another explanation could be that there was some instability in the injection beamline. If the ion beam was shifted so it hit the suppressor of Faraday cup FC02, then the current read value was incorrect and elevated. The FC02 value would be elevated because of secondary electron emission from the suppressor. Secondary emitted electrons cause induction of positive current in the Faraday cup. If the monitored ion beam hit the suppressor, then these electrons caused misinterpreted beam current in the Faraday cup. This higher value would have pulled the final transmission efficiency value down, since the FC02 value is in the denominator of the equation 1.

Measurements show some interesting aspects of stripping efficiency dependent on the stripping gas pressure. The stripping process for 1^+ charge state increases with increasing pressure to maximal values, and then it decreases to very low efficiencies. The maximal value for $^4He^{1+}$ transmission efficiency, nearly 40%, was observed around 10 μbar. The tail (pressure above ~ 45 μbar) in the Figure 34 exhibits the assumed dependency from terminal voltage, which influences the energy of helium ions in the stripping process. Ions with the lowest measured energy (1.5 MeV gain in first acceleration step), are stripped more compared to the ions with the highest energy (3 MeV gain).

All results for 2+ charge state exhibit increasing tendency with increasing stripping gas pressure. In all measurements, there were observed a gas pressure level from which the transmission efficiency remains stable. Depending on the terminal voltage this level is increased with increased terminal voltage. At 1.5 MV, this level is approximately at 30 μbar. Towards to 3.0 MV, this value rises to 40 μbar of stripping gas pressure (gray triangles in Fig. 28 and Fig. 33).

4.4. Transmission efficiency for ^{9}Be ion beam

Beam of ^{9}Be ions was produced in the MC-SNICS. As a source material for this beam, beryllium oxide (BeO) was used. Beryllium was extracted from the ion source MC-SNICS in a form of molecular ions $^{9}Be^{16}O^{-}$. These ions then formed an ion beam, which was accelerated in the Pelletron at different values of terminal voltage. Molecular ions $^{9}Be^{16}O$ passing through the stripping channel are dissociated into atomic ions of ^{9}Be and ^{16}O. In the stripping process most of these ions gain certain positive charge, and according to this charge state they gain certain acceleration in the electrostatic field of the terminal electrode, which is held at high positive voltage. The energy of such accelerated ions can be calculated using the equation (3.):

$$E = \frac{m}{M}(E_i + e\,TV) + n\,e\,TV \qquad (3.)$$

where m is the atomic mass of accelerated ions, M is the atomic mass of molecular ions entering the accelerator, E_i is the injection energy of ions entering the accelerator, e is the elementary electric charge, TV is the terminal voltage and n is the charge state of accelerated ions. We were interested in ^{9}Be ions, therefore the m and M were selected as 9 and 25 respectively. The injection energy E_i was set to 61 keV. After acceleration we observed charge states 1^{+}, 2^{+} and 3^{+} of ^{9}Be ions. Fully stripped ions, i.e., charge state 4^{+}, were not measured because Faraday cups' lower detection limit is 0.1 nA, and the intensity of $^{9}Be^{4+}$ beam was in most cases below this value. Table 3 shows the energies of ^{9}Be ions according to the charge state and terminal voltage used for transmission efficiency measurements and calculations.

Terminal voltage (MV)	1.500	1.800	2.100	2.400	2.700	3.000
$^{9}Be^{1+}$ Total energy (MeV)	2.062	2.470	2.878	3.286	3.694	4.102
$^{9}Be^{2+}$ Total energy (MeV)	3.562	4.270	4.978	5.686	6.394	7.102
$^{9}Be^{3+}$ Total energy (MeV)	5.062	6.070	7.078	8.086	9.094	10.102

Table 3: Total energy of accelerated $^{9}Be^{1+}$, $^{9}Be^{2+}$ and $^{9}Be^{3+}$ ion beams for individual values of terminal voltage. The values were calculated according to the equation (3.)

Stripper gas pressure dependency of ^{9}Be transmission efficiency values are shown in next figures. Notice that the transmission efficiency for 3+ charge state has a different scale on the right axis, because these values are too low compared to the other values in the

graphs. For better viewing these scales and corresponding plots are in gray color (figures 36 – 41). The transmission efficiency for charge states 1+, 2+ and sum of all three efficiencies ("Total") are in black color with scale on the left axis. The individual charge states transmission efficiency plots for all monitored terminal voltages are shown in the Figure 42. The total transmission efficiency (sum of transmission efficiencies for individual charge states) for all monitored terminal voltages is plotted in the Figure 43.

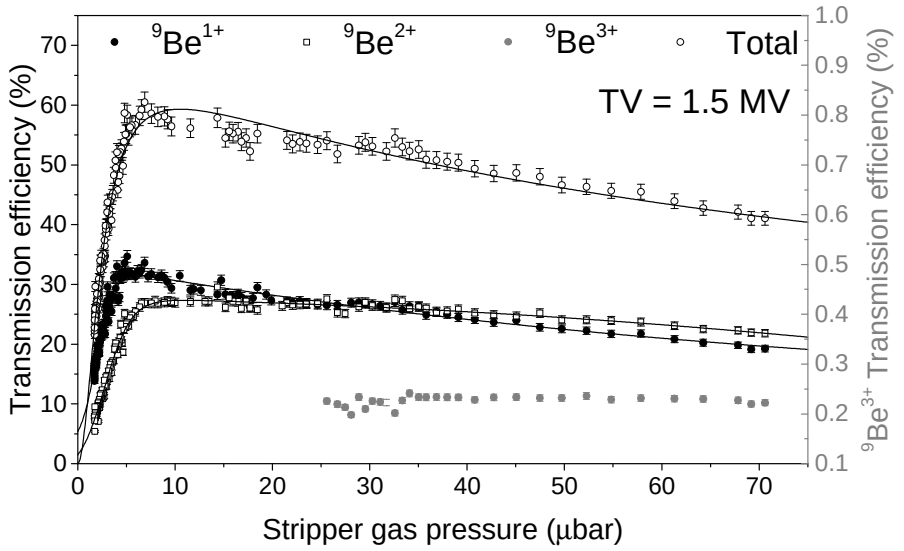

Fig. 36: Beryllium transmission efficiency for 1.5 MV terminal voltage. The $^9Be^{3+}$ values were measured from the pressure ~ 25 μbar (below only the lower detection limit of FC05 was reached)

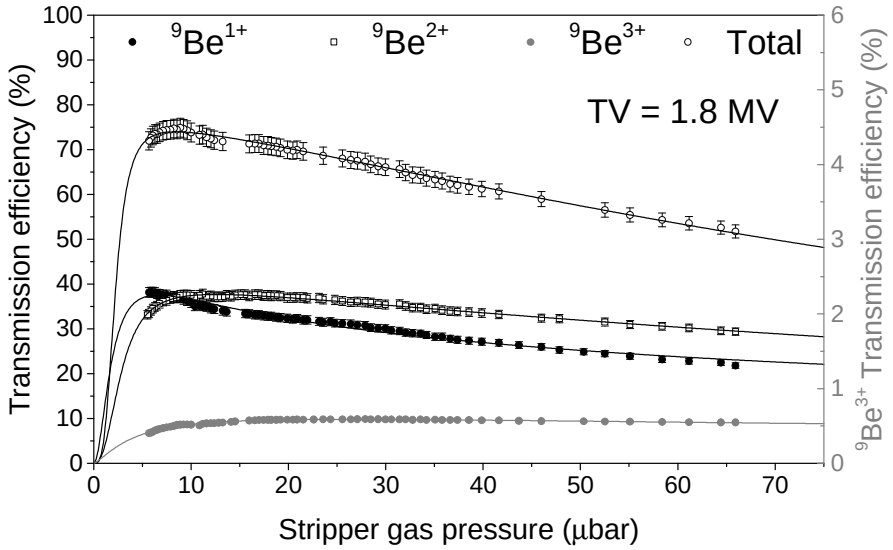

Fig. 37: Beryllium transmission efficiency for 1.8 MV terminal voltage

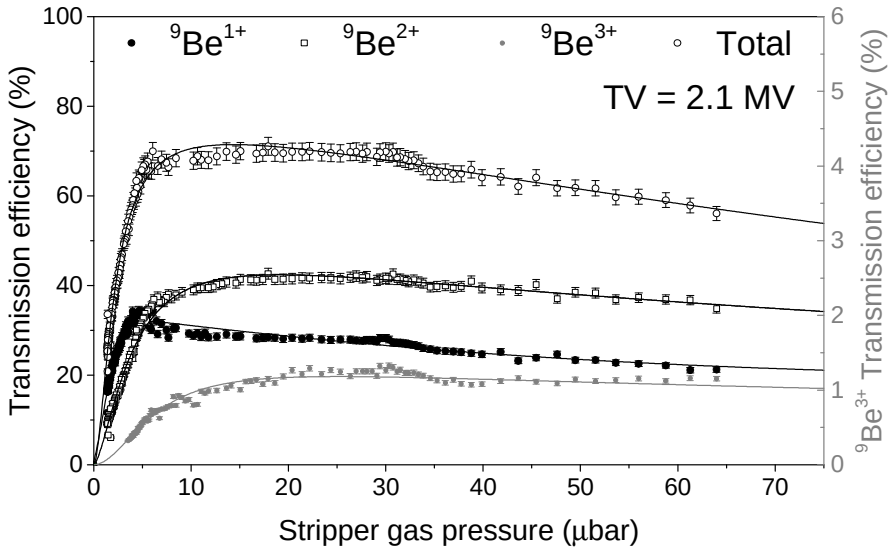

Fig. 38: Beryllium transmission efficiency for 2.1 MV terminal voltage

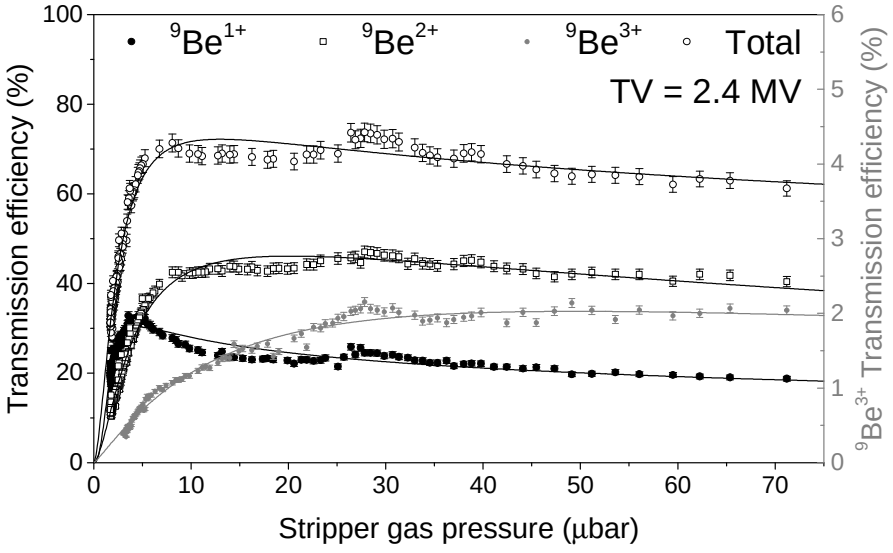

Fig. 39: Beryllium transmission efficiency for 2.4 MV terminal voltage

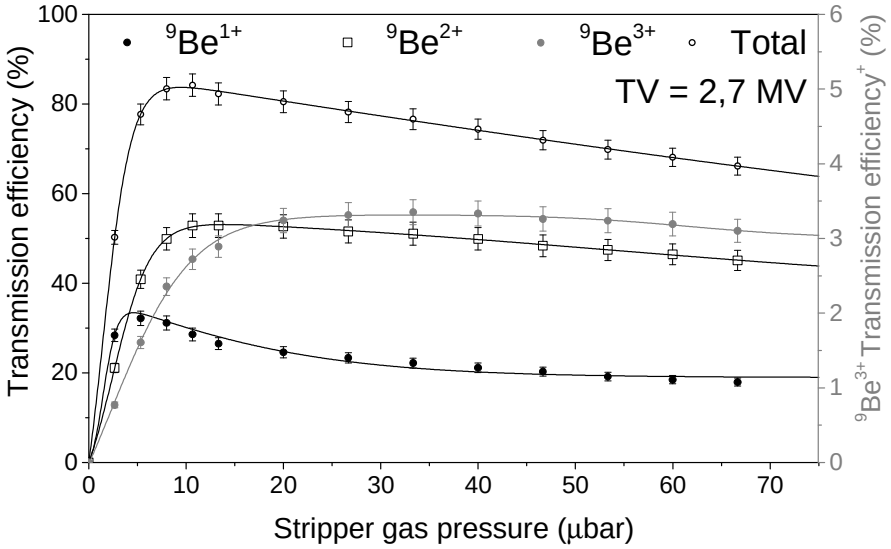

Fig. 40: Beryllium transmission efficiency for 2.7 MV terminal voltage

This measurement was done manually, therefore the amount of points is lower compared to previous script measurements [Zeman, 2016]

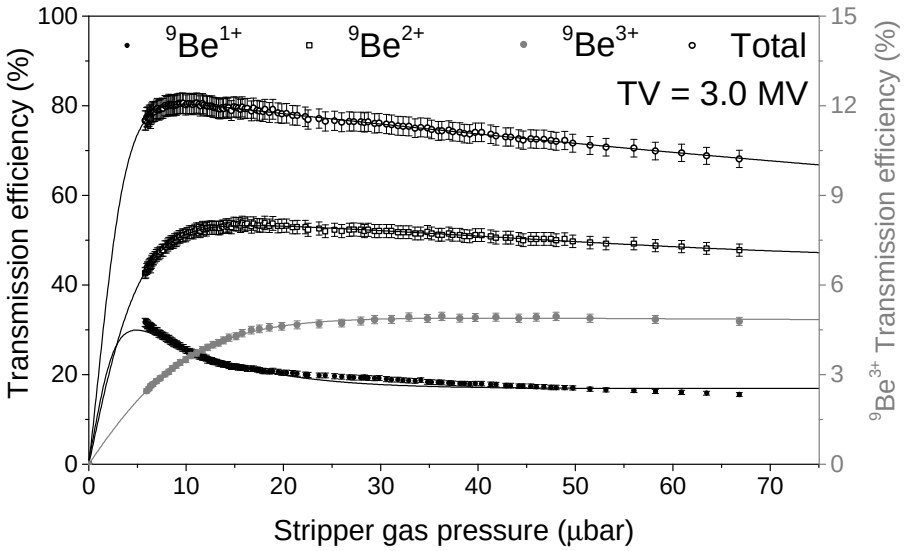

Fig. 41: Beryllium transmission efficiency for 3.0 MV terminal voltage

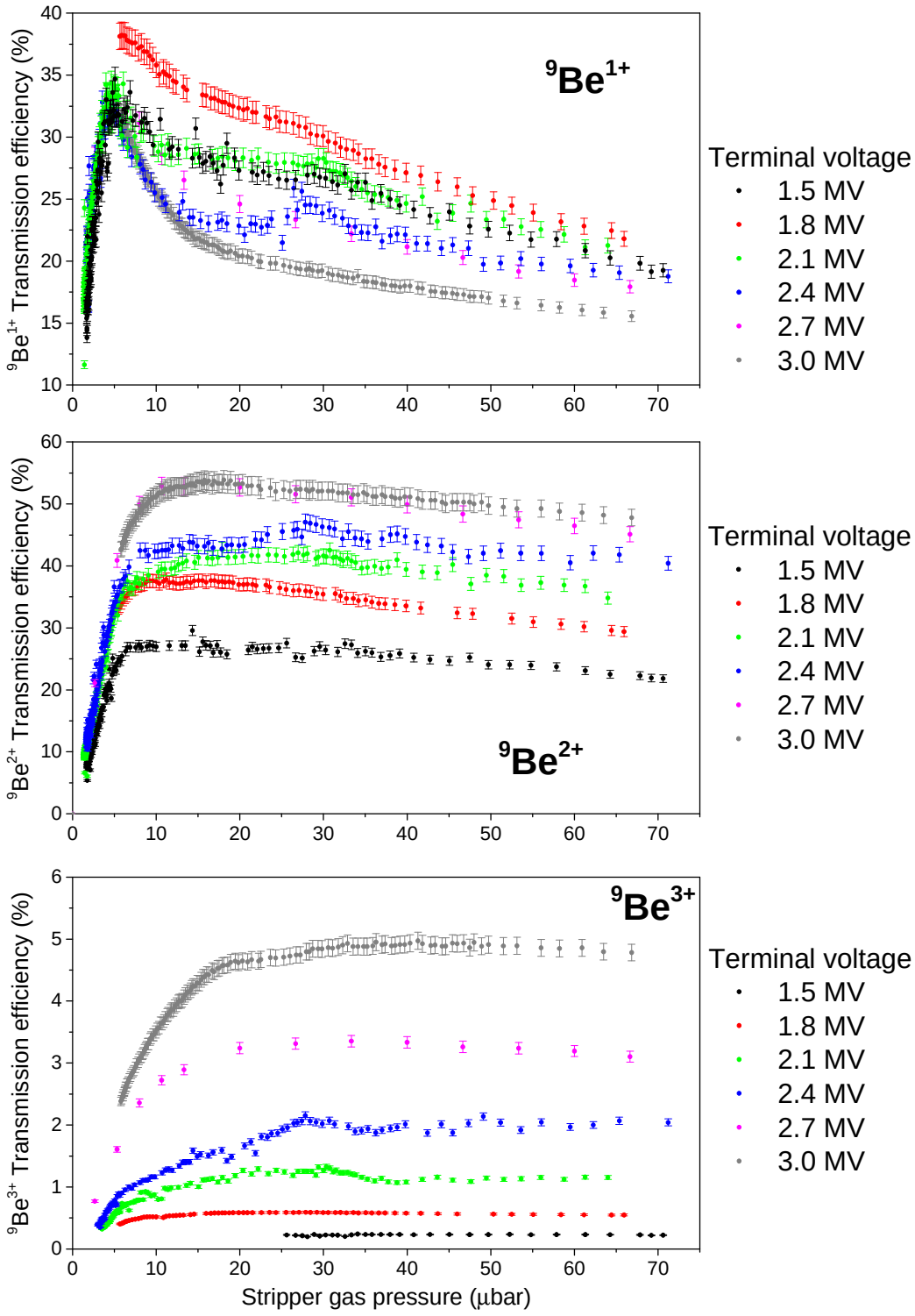

Fig. 42: Beryllium transmission efficiency values for all monitored terminal voltages. The stripper gas pressure scale is the same in all graphs. The transmission efficiency scales are different for individual charge states.

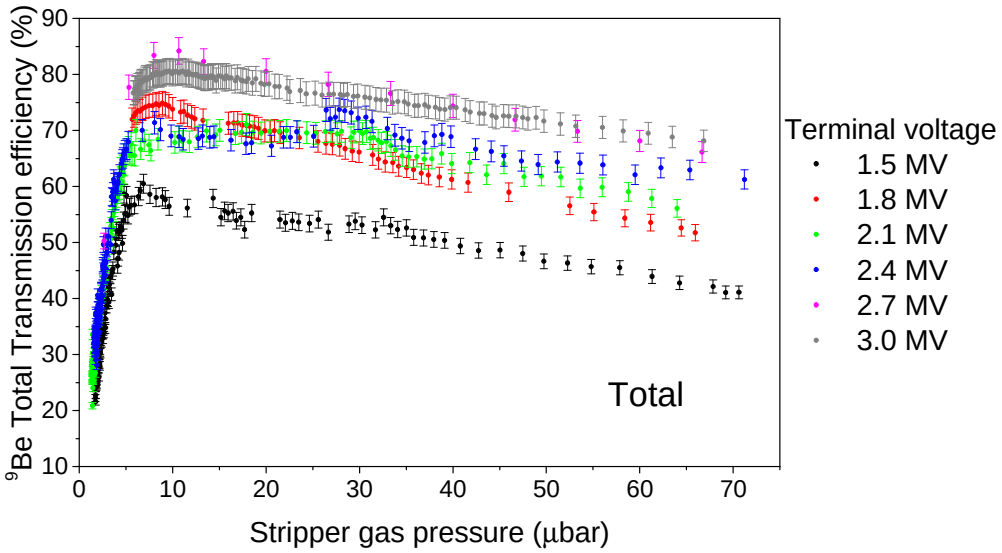

Fig. 43: Total Beryllium transmission efficiency values for all monitored terminal voltages. Each total value represents sum of transmission efficiency values of individual charge states for corresponding stripper pressure level and monitored terminal voltage.

All of the measurements were performed using the script. For each terminal voltage this script ran usually over-night. The script was slowly lowering stripping gas pressure (starting around 70 µbar) and it controlled the switching magnet field intensity to record the Faraday cups' values for each charge state. ^{9}Be transmission efficiency measurements were also performed manually earlier (beginning of 2016). These results can be found in [Zeman, 2016]. The majority of script measurements exhibit satisfying results. Only 2.7 MV script measurement went wrong. The reason is that during the night the Pelletron voltage was not stable, thus these results were unusable. Therefore, values from manual measurements were used in the figures. This is also good for comparison to see that the previous manual measurements more or less follow the script measurements.

The beryllium 1+ charge state transmission efficiency behavior exhibit a rapid increase with increasing stripping gas pressure. At pressure range 4 – 6 µbar this efficiency reaches maximal level ~ 38% for 1.8 MV terminal voltage (Figure 42, top graph). Depending on the terminal voltage level, the efficiency subsequently decreases or increases with pressure increment more rapidly or slowly. For 1.8 MV the transmission efficiency decrement is the lowest, for 1.5 MV and 2.1 MV the decrement is higher and for the rest of monitored voltages is this decrement even higher. The terminal voltage transmission efficiency dependency at ~ 5µbar pressure is shown in the Figure 44.

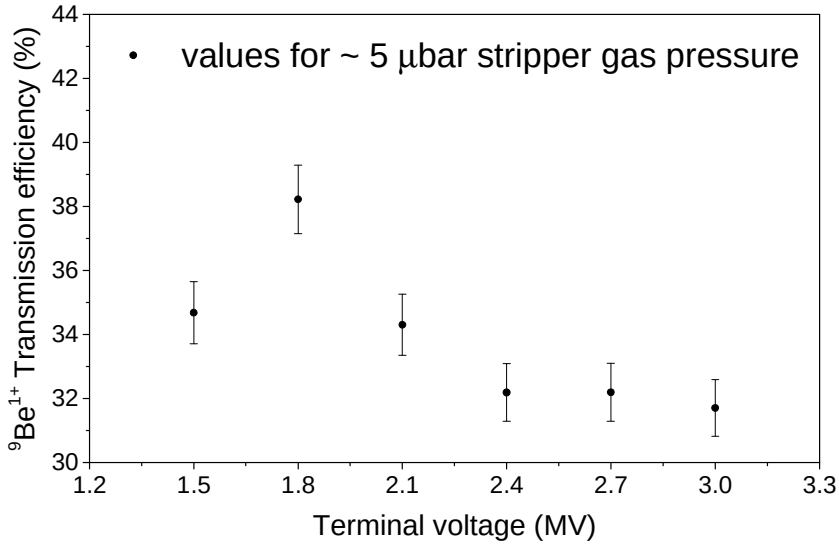

Fig. 44: Dependency of $^{9}Be^{1+}$ transmission efficiency on the terminal voltage at ~ 5 μbar stripper gas pressure. The maximal value was measured for 1.8 MV.

The beryllium 2+ charge state transmission efficiency exhibit different behavior compared to 1+ charge state. The increment with increasing pressure is similar, but not as rapid. For all monitored terminal voltages, the transmission efficiency increases with increasing pressure. On the contrary to 1^{+} charge state the increment reaches the maximal value, and subsequently remains more or less stable for a certain region of pressure. Then the efficiency slowly decreases. The increment reaches its maximal values at different stripping gas pressures. For 1.5 MV this pressure is at ~ 8 μbar, with increasing terminal voltage this pressure rises, ending at ~ 15 μbar for 3.0 MV (Figure 42, middle graph). The transmission efficiency increment with the terminal voltage was observed as well. For 1.5 MV the transmission efficiency reaches ~ 25% level. This level is rising with increasing terminal voltage, reaching ~ 53% for 3.0 MV.

The beryllium 3+ charge state transmission efficiency values were very low. For 1.5MV terminal voltage of the Faraday cup FC05 reached its lower limit (0.1 nA) at 25 μbar of stripping gas pressure. Therefore in the Figures 36 and 42 the values start from this level. Nevertheless, increasing behavior of transmission efficiency was observed with increasing terminal voltage. The efficiency starts at ~ 0.22% level for 1.5 MV (Figure 36, right axis) and increases with terminal voltage to ~ 5% level for 3.0 MV (Figure 42, bottom

graph). Compared to the other 2 monitored charge states, the 3+ charge state transmission efficiency exhibit with increasing pressure slower increment with a long stable plateau.

4.5. Transmission efficiency for ^{12}C ion beam

Measurements and results of ^{12}C ion beam transmission efficiency are included in Appendix B [Zeman, 2016] and also some results for ^{9}Be and ^{12}C were published in [Povinec, 2016], Appendix D.

4.6. Transmission efficiency summary

Maximal values of the transmission efficiencies for ^{1}H, ^{4}He, ^{9}Be and ^{12}C ions are listed in Table 4. Some maximal values were observed for the same charge state at different terminal voltages. These values are recorded both.

Ion	Charge state	Terminal voltage (MV)	Strip. gas pressure (μbar)	Transmission efficiency (%)
^{1}H	1+	1.8	43	53.6 ± 1.5
^{4}He	1+	2.1	9	39.3 ± 1.1
	2+	2.1	51	62.6 ± 1.8
	2+	3.0	60	63.5 ± 1.8
^{9}Be	1+	1.8	6	38.2 ± 1.1
	2+	2.7	13	52.9 ± 1.4
	2+	3.0	16	53.8 ± 1.5
	3+	3.0	41	5.0 ± 0.2
^{12}C	2+	1.8	11	42.3 ± 1.1
	3+	2.7	27	47.7 ± 1.2
	4+	2.7	40	20.5 ± 0.9

Table 4: Maximal measured values of transmission efficiency for individual ion beams.

Values for smooth dependencies were taken from the highest points, but the efficiency was more-less stable at wide range of stripping gas pressure.

5. Ion beam profile simulations at the end of the beam line

Two main ion optics devices installed in the CENTA laboratory at the end of current beam line (Figure 6) are magnetic quadrupole triplet lens (QP) and switching magnet (SM). The aim of simulations is to find out how the transverse beam profile changes at the end of the beam line when passing through the QP and SM. For this purpose SIMION software was used. This program enables user to create a models for ion optics devices for 2D symmetric and/or 3D asymmetric electrostatic and magnetic fields. A specific model consists of individual points in space. A certain electrostatic potential or magnetic field flux density (referred to as B in equations and literature) value can be assigned to each point of this modeled device. The units that are used in SIMION are volts for electrostatic potential and so-called "Mags" for magnetic field flux density (this is special unit used by SIMION which can be easily converted into Gauss or Tesla). The program is capable of creating potential field up to 20.10^9 points (190 GB) while the RAM capacity remains crucial.

More methods of ion optics devices simulation can be used. The SIMION software itself is capable of this modeling, but it is possible to use other software (C++, Perl, Python…). Each modeled device can contain either electrostatic or magnetic field. Combined electromagnetic fields are not supported in SIMION. This fact can be overcome since the simulations run in an environment called "workbench" which enables to combine more models, to set their dimensions, geometry and spatial orientation. A workbench strategy allows positioning, size, and orienting up to 200 instances (3D images) of potential arrays of different grid densities and symmetries to permit the simulation of much larger systems that don't easily fit into a single array. In this way it is possible to model complex systems and also the whole experimental setup.

There are also more options how to define and track the ion movement as well. It is possible to choose between individual and group flight while the trajectories can be visualized as lines or flying dots. The trajectory calculations are guided by user pre-defined field, electrostatic or magnetic. The Runge-Kutta method with relativistic corrections is used for differential and Laplace equations calculations. The values for particle mass, charge, energy and other parameters can be defined precisely or can be distributed with a certain probability density. Once the system is modeled, individual parameters can be

varied “on-line”, i.e., during the ion movement, so it is possible to simulate various effects (RF fields, ion traps, focus, deflection …).

SIMION is also capable of processing ion repulsion what can be used for space-charge effects calculations. It is possible to track flying ions in different layers and cross sections of 3D modeled devices. The program output can be adjusted according to user’s requirements. User can set what parameters to record and when these parameters should be recorded. This enables to monitor the position of a single ion or of a whole ion beam before it enters the device, inside the device (in more positions, if desirable) and in the exit off the device. Depending on the modeled field dimensions, it is possible to track ions in certain distance from the ion optics device and to study various effects on the ion beam.

5.1. Ion optics principles

Electric fields

The movement of particle with charge q in homogenous electric field with electric intensity E is affected by electric force F_e according to the equation (4.):

$$F_E = q\,E \tag{4.}$$

Trajectory of ion passing through the transversal electric field is being curved. This curvature can be calculated using relation between centripetal force F_C and the electric force F_E implementing equation (5.):

$$F_C = \frac{m\,v^2}{R_E} = q\,E = F_E \tag{5.}$$

Implementing the relation for kinetic energy E_K:

$$E_K = \frac{1}{2}\,m\,v^2 \tag{6.}$$

the radius of ion trajectory curvature R_E caused by electric field can be calculated:

$$R_E = \frac{2\,E_K}{q\,E} \tag{7.}$$

Result of the equation (7.) is that electrostatic ion optics devices can be used as filters for ions with the same charge q but different kinetic energy E_K; or for ions with the same kinetic energy but different charge.

Magnetic fields

A charged particle (with charge q) moving in a magnetic field is affected by magnetic force F_M. If the particle's velocity vector v is perpendicular to the magnetic field flux density vector B, then the magnetic force equals to:

$$F_M = q\ v\ B \tag{8.}$$

Trajectory of ion passing through the transversal magnetic field is being curved. This curvature can be calculated using relation between centripetal force F_C and the magnetic force F_M implementing equation (9.):

$$F_C = \frac{m\ v^2}{R_B} = q\ v\ B = F_M \tag{9.}$$

Implementing the relation for momentum $p = m\ v$, the curvature radius in magnetic field R_M can be calculated as follows:

$$R_M = \frac{p}{q\ B} \tag{10.}$$

Result of this equation is that magnetic ion optics elements can be used as filters for ions with the same charge q but different momentum and vice versa (in practice, the momentum filters utilization is more common).

Determining field potentials

The electrostatic or magnetic field potential (e.g. Volts or Mags - SIMION's magnetic potentials) at any point within an electrostatic or static magnetic lens can be found by solving the Laplace equation with the electrodes (or poles) acting as boundary conditions. The Laplace equation assumes that there are no space-charge effects and boundary conditions are sufficiently constrained [SIMION, 2017]. The Laplace equation constrains all electrostatic and static magnetic potential fields to conform to a zero charge volume density assumption (no space-charge). This is the equation that SIMION uses for computing electrostatic and static magnetic potential fields (equation (11.)).

$$\nabla^2 V = \nabla . \nabla \, \mathrm{V} = 0$$

$$\nabla \, \mathrm{V} = \left(\frac{\partial \mathrm{V}}{\partial \mathrm{x}}\right) \mathrm{i} + \left(\frac{\partial \mathrm{V}}{\partial \mathrm{y}}\right) \mathrm{j} + \left(\frac{\partial \mathrm{V}}{\partial \mathrm{z}}\right) \mathrm{k} = \mathrm{E} \qquad (11.)$$

[SIMION, 2017]

$$\nabla^2 \, \mathrm{V} = \nabla . \, \mathrm{E} \, = \frac{\partial E_x}{\partial \mathrm{x}} + \frac{\partial E_y}{\partial \mathrm{y}} + \frac{\partial E_z}{\partial \mathrm{z}} = 0$$

The Poisson equation:

$$\nabla^2 \, V = \nabla . \nabla \, V = \, -\rho_f / \varepsilon \qquad (12.)$$

allows a non-zero charge volume density ρ_f (space-charge). When the density of ions becomes great enough (high beam currents) they will (by their presence) significantly distort the electrostatic potential fields. In these conditions, Poisson's equation should be used (instead of Laplace's) to estimate potential fields. SIMION does not support Poisson solutions to field equations. It does however employ charge repulsion methods that can estimate certain types of space-charge and particle repulsion effects [SIMION, 2017].

5.2. Results of the SIMION simulations

The magnetic quadrupole triplet lens (QP) and the switching magnet (SM) models were created in order to monitor the beam profile at the end of beam line. The devices were modeled using 3D CAD software Autodesk Inventor. These models were “installed” into SIMION’s workbench environment in proper geometry. For this purpose the manufacturer’s (NEC, USA) drawings of QP and SM were used (Figure 45). The SM’s magnetic flux density (B) was set in simulations to bend the trajectory into 45° analyzing beam line. Next, in the distance corresponding to the end of this beam line, a target foil was placed to obtain information about transversal beam profile after ions incidence. For better imagination, this distance was 2085 mm from the exit edge of the SM.

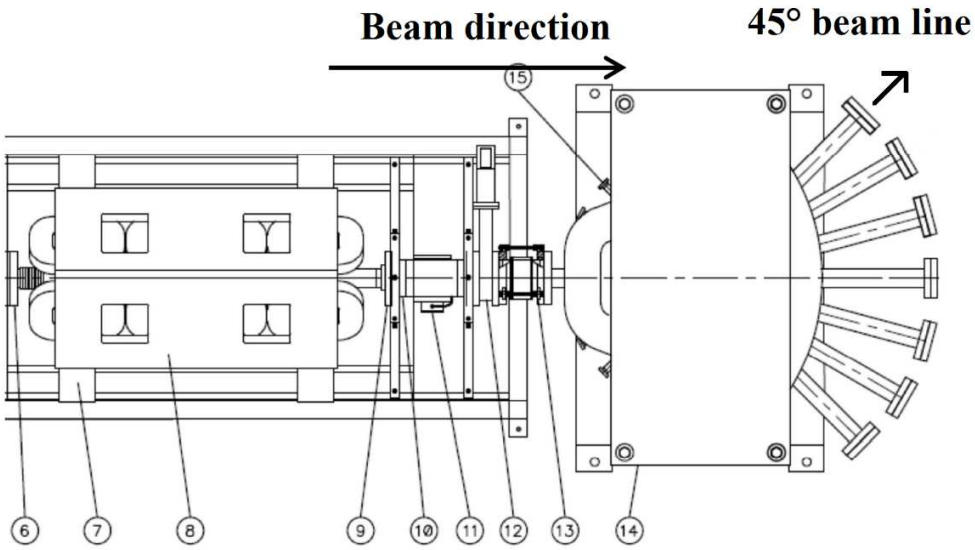

Fig. 45: A top view on the QP and SM [Switch, 2011].

Labels for beam direction and 45° analyzing beam line with arrows were added for better orientation in the figure.

6 – entrance into the QP
7 – QP holder
8 – magnetic quadrupole triplet lens (QP)
9 – zero length reducer
10 – drift tube
11 – magnetic steerer
12 – gate valve
13 – bellows
14 – switching magnet (SM)
15 – flange

Models of SM and QP

Proper SM and QP dimensions were taken from the manufacturer's (NEC, USA) documentation (Figures 46, 47). Note that all dimensions are stated in inches. Beam of $^{4}He^{2+}$ ions was used for simulations. The devices were modelled and placed into SIMION workbench according to the geometry (Fig. 45). Also a target foil was placed into a proper distance corresponding to the real target distance in the 45° analyzing beam line. The purpose of this foil was to monitor the displacement of ions after incidence. SIMION workbench layout for simulations is displayed in the Figure 48. The monitored energy was 3.052 MeV. The initial transversal beam profile was set to symmetrical circular with Gaussian distribution around the center (position 0,0). The FWHM was set to 5 mm. This value was selected because this is the assumption for transversal profile of beam exiting the Pelletron and entering the focusing beam line.

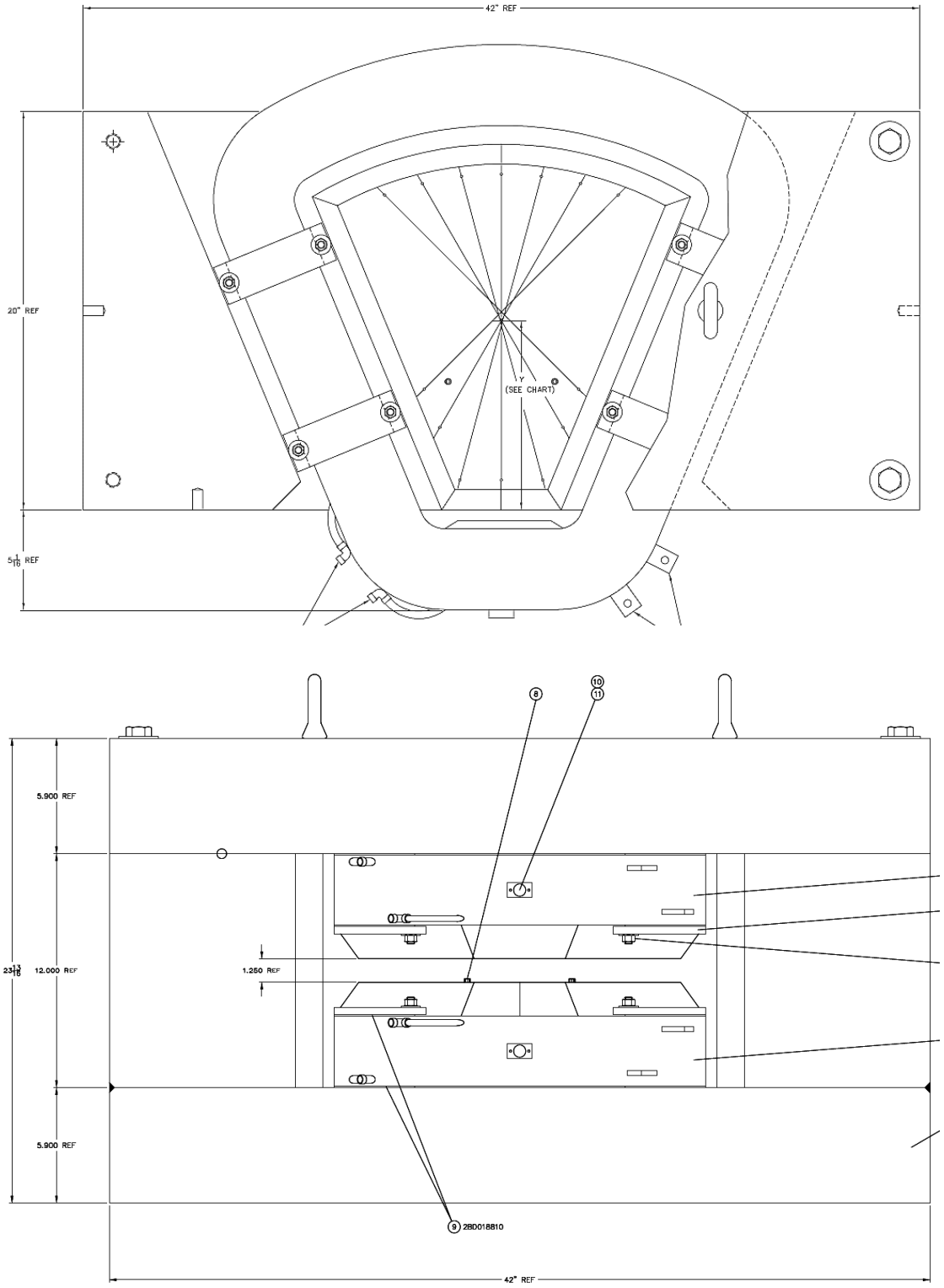

Fig. 46: Schematic view of the Switching Magnet (SM).

Top view and side view as documented by the manufacturer. Dimension are inches [Switch, 2011].

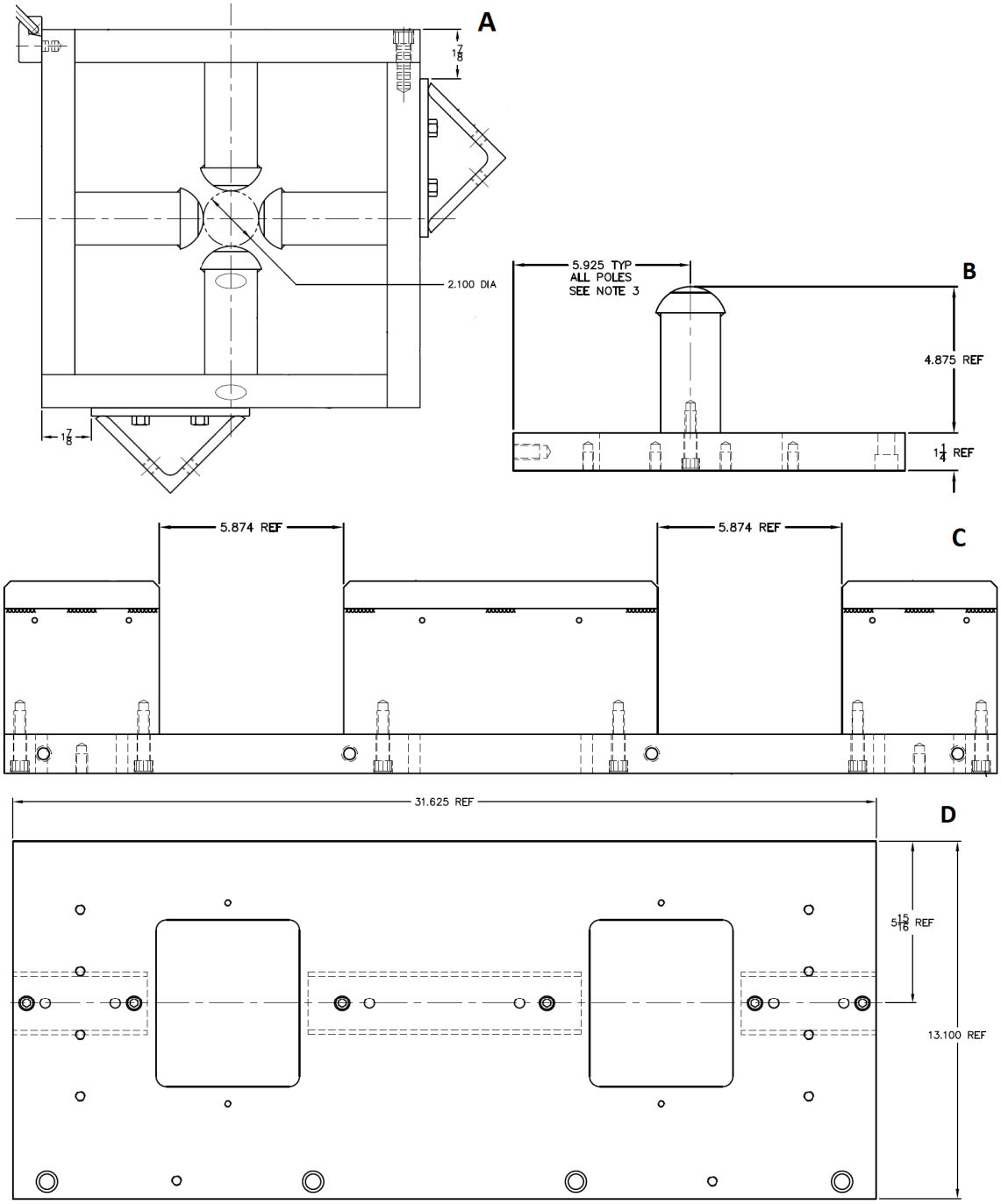

Fig. 47: Schematic view of the magnetic quadrupole triplet lens (QP). Different views are displayed as follows: front view (A), a single pole detail (B), longitudinal section (C), side view (D). Dimension are inches (from the manufacturer's documentation).

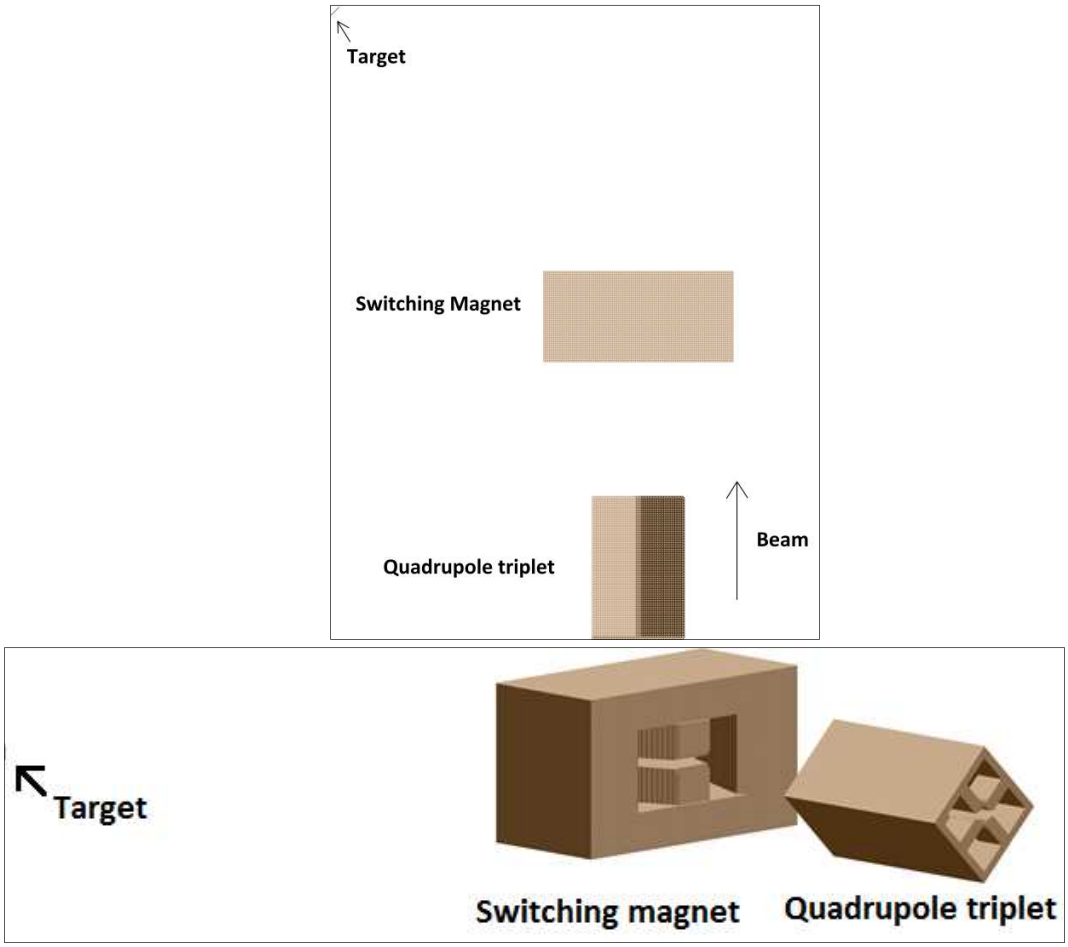

Fig. 48: SIMION workbench layout of simulations for SM and QP. The upper figure shows top view of models; the lower figure is the side view with beam incoming from the right into the QP. The target represents a small plane which was used as target foil where the beam profile was monitored. The target was placed into 2085 mm distance from the exit edge of SM what corresponded to the real target distance in 45° analyzing beam line.

The profile of 3.052 MeV $^{4}He^{2+}$ ion beam can be seen in the Figure 49. The X – axis represents horizontal and the Y – axis vertical dimensions. Each simulation result contains 10 000 ions. Note that the magnetic field flux density unit is Gauss in the SIMION software (1T = 10 000G). Therefore the simulations operate with these units as well.

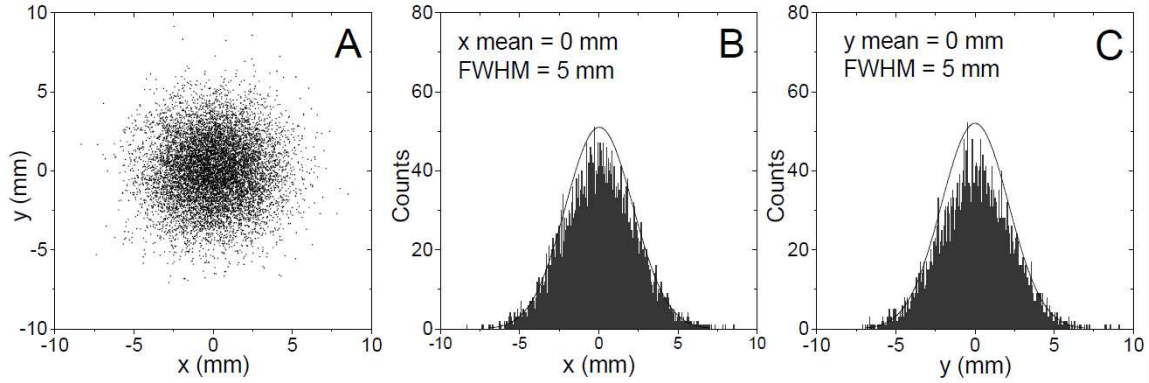

Fig. 49: Transversal profile of $^{4}He^{2+}$ ion beam used in simulations (A), horizontal dimension (B) and vertical dimension (C). Ions in the beam were Gaussian distributed around the center – position (0,0). The FWHM was 5 mm. The amount of ions was 10 000.

The simulations were performed as follows:

1.) Firstly, the proper magnetic field flux density of the SM's magnetic field for ion beam trajectory deflection had to be found. The exit channel was 45° beam line and ions had to hit the middle of the target foil placed at the end of this beam line. For these conditions, the magnetic field flux density of SM was found to be 3914.73 Gauss.

2.) Next, the magnetic field of the QP was varied. The QP consists of 3 magnetic lenses. For performed simulations, symmetric magnetic fields of whole QP were considered. This meant that the magnetic flux density was gradually increased with a 50 Gauss step while the field was keeping symmetrical, i.e., the middle lens was kept stable and the outer ones were varied.

3.) The next step was to perform simulations for switched polarity of QP. The procedure was the same as in the step (2.), i.e., 50 Gauss steps with keeping symmetrical magnetic field.

4.) Finally, the proper adjustment of QP's magnetic field had to be found in order to obtain focused ion beam.

Results of simulation are shown in the next figures. Transversal profile of beam which passed through the system with QP set to 0 Gauss is shown in the Figure 50. Next, the magnetic field of QP was varied with 50 Gauss step, i.e., +50, +100, +150 and +200 Gauss

magnetic field flux densities (B) were simulated (Figures 51 – 54). Then, the same levels of B were used but with changed polarity of QP (Figures 55 – 58). The coordinates were chosen so that the beam is entering the target (from the readers' point of view, the paper). The X – axis represents horizontal direction, the Y – axis represents the vertical direction. The positive X coordinate represents right side of the target foil, negative represents left side. Positive Y coordinate means up from the center and negative down from the center (0,0).

Transversal profile of $^{4}He^{2+}$ ion beam with QP set to 0 Gauss

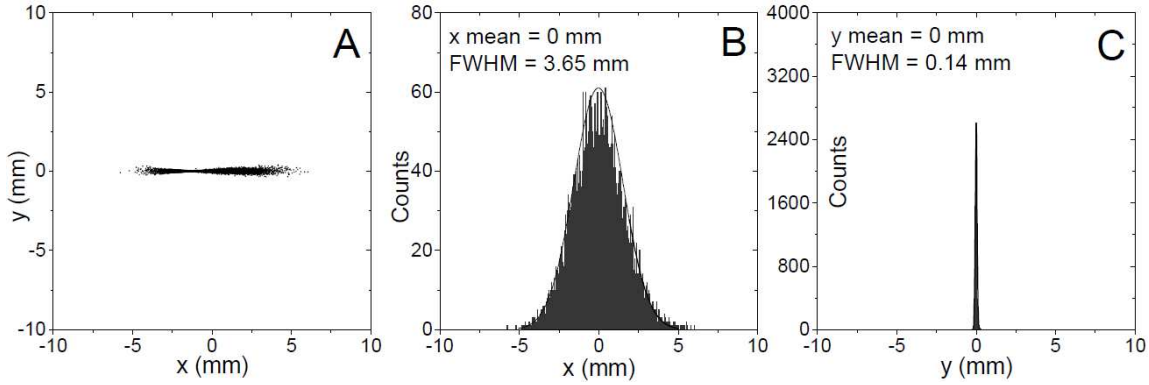

Fig. 50: Transversal profile of $^{4}He^{2+}$ ion beam passed through the SM with QP "turned off". The magnetic field of QP was set to 0 at all lenses. The beam profile was monitored at the target foil.

Profile of $^{4}He^{2+}$ ion beam with QP set to +50 Gauss

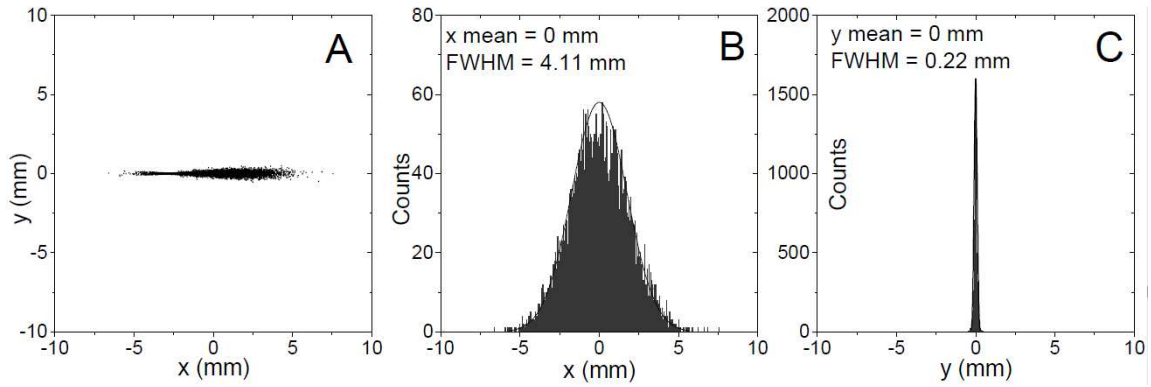

Fig. 51: Transversal profile of $^{4}He^{2+}$ ion beam (A), horizontal (B) and vertical (C) dimension.

Profile of $^{4}He^{2+}$ ion beam with QP set to +100 Gauss

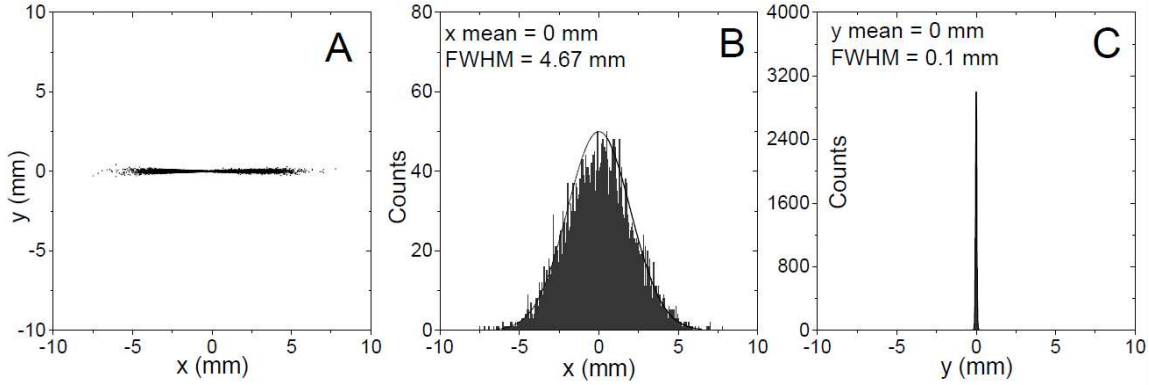

Fig. 52: Transversal profile of $^{4}He^{2+}$ ion beam (A), horizontal (B) and vertical (C) dimension.

Profile of $^{4}He^{2+}$ ion beam with QP set to +150 Gauss

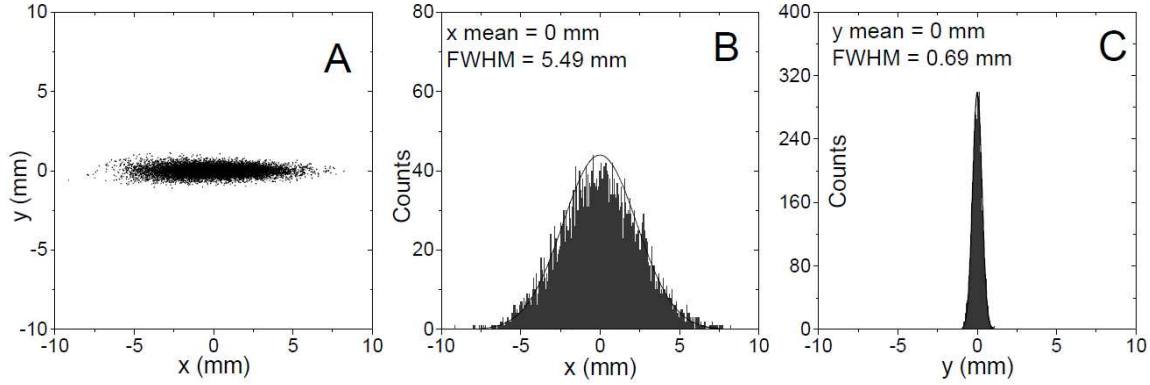

Fig. 53: Transversal profile of $^{4}He^{2+}$ ion beam (A), horizontal (B) and vertical (C) dimension.

Profile of $^{4}He^{2+}$ ion beam with QP set to +200 Gauss

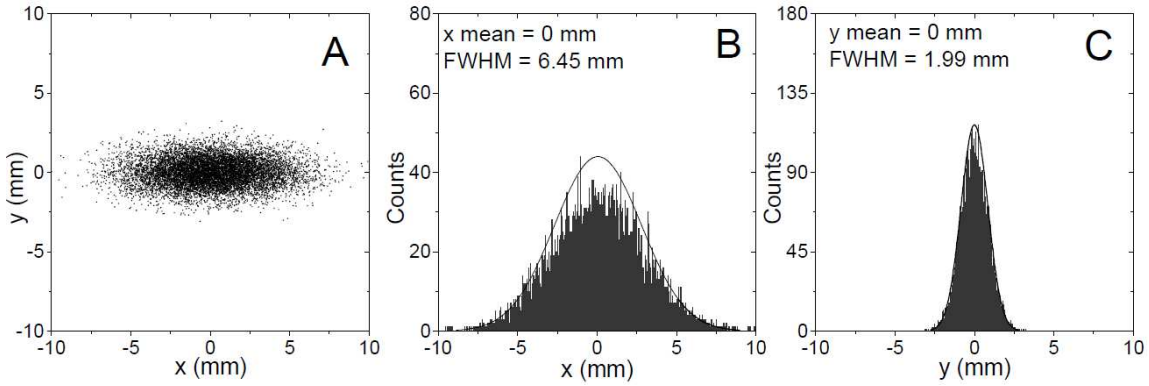

Fig. 54: Transversal profile of $^{4}He^{2+}$ ion beam (A), horizontal (B) and vertical (C) dimension.

Profile of $^{4}He^{2+}$ ion beam with QP set to -50 Gauss

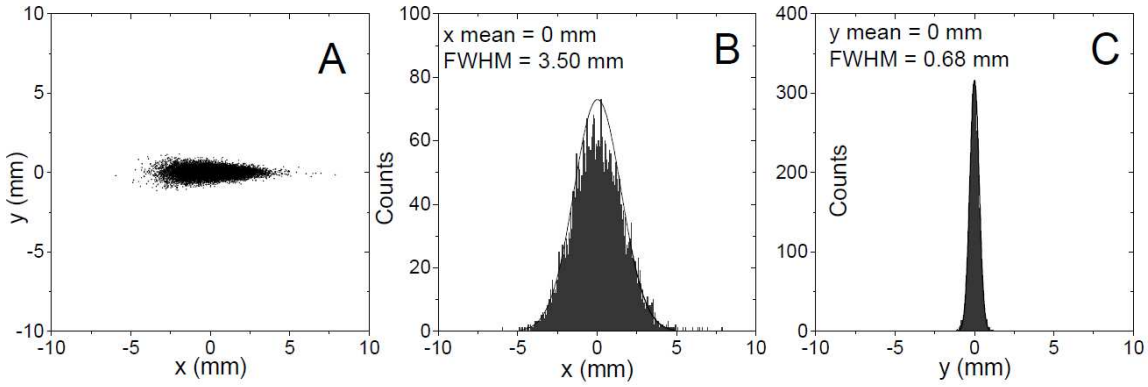

Fig. 55: Transversal profile of $^{4}He^{2+}$ ion beam (A), horizontal (B) and vertical (C) dimension.

Profile of $^{4}He^{2+}$ ion beam with QP set to -100 Gauss

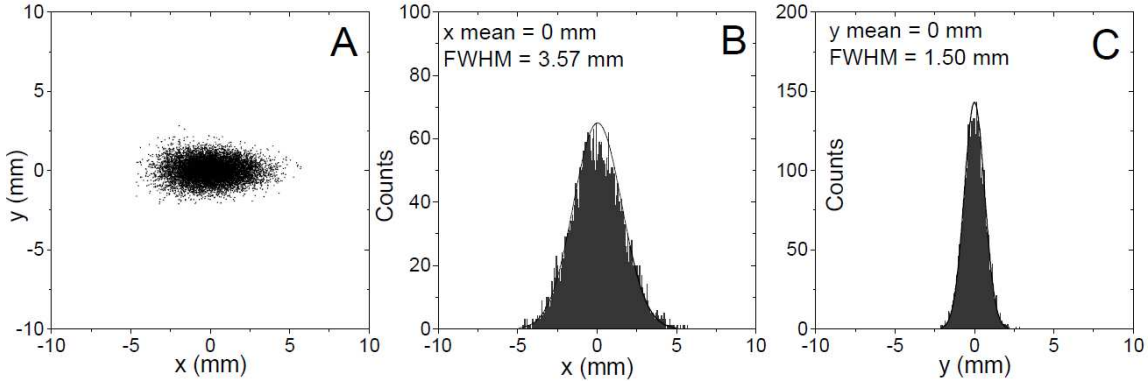

Fig. 56: Transversal profile of $^{4}He^{2+}$ ion beam (A), horizontal (B) and vertical (C) dimension.

Profile of $^{4}He^{2+}$ ion beam with QP set to -150 Gauss

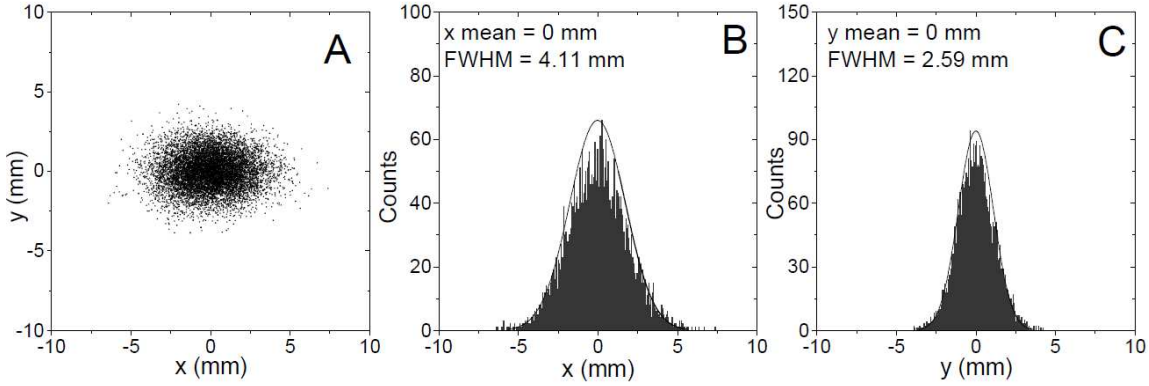

Fig. 57: Transversal profile of $^{4}He^{2+}$ ion beam (A), horizontal (B) and vertical (C) dimension.

Profile of $^4He^{2+}$ ion beam with QP set to -200 Gauss

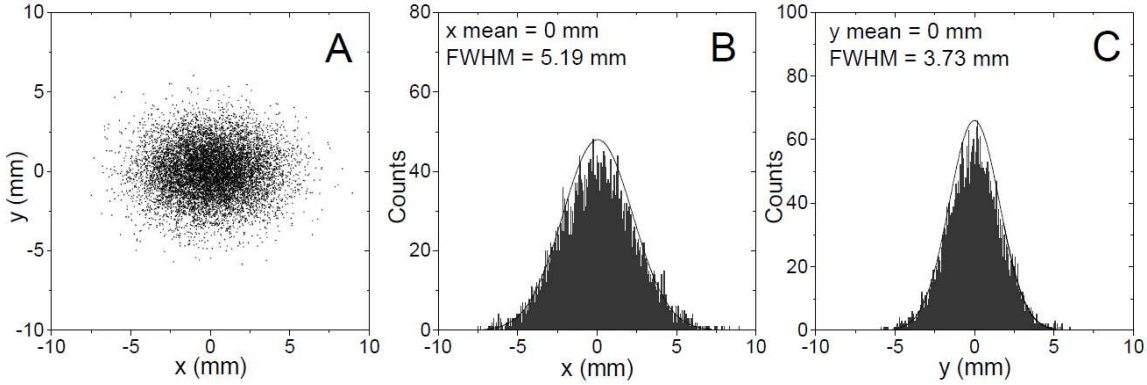

Fig. 58: Transversal profile of $^4He^{2+}$ ion beam (A), horizontal (B) and vertical (C) dimension.

QP settings of symmetrical magnetic fields were not leading to satisfying results for beam focus to small diameter. Some of the settings in simulations exhibit better focus in one direction but the beam was defocused in the opposite one. Some kind of this result was expected, but with better focusing power of symmetrical QP settings. The assumption was that there had to exist a setting for QP which would lead to focused ion beam. In this purpose, another strategy for focused $^4He^{2+}$ beam was used. The whole triplet lens's magnetic field was varied with keeping one of outer quadrupoles at certain level and varying the magnetic fields on the other ones. This procedure was quite long and exhausting. Numerous simulations were performed with more-less zero results. The positive aspect was that during the simulation process, some settings of magnetic field exposed a direction which should be taken.

Profile of $^4He^{2+}$ focused ion beam with non-symmetric QP setting

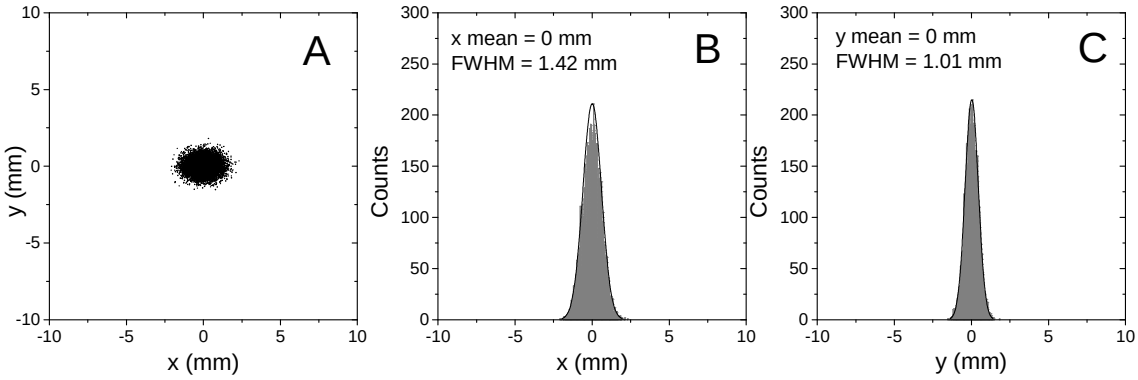

Fig. 59: Transversal profile of $^4He^{2+}$ ion beam (A), horizontal (B) and vertical (C) dimension.

Finally, an appropriate setting of QP's magnetic field flux density was found. Satisfying results are shown in the Figure 59. The original beam with 5 mm diameter was focused into smaller diameter of ~ 1.4 mm. Currently (April 2017), these settings are the best reached. With further adjusting of QP in simulations larger beam diameters were observed.

Comment

Note, that each of simulation figures contains 10 000 points representing 3.052 MeV $^{4}He^{2+}$ *ions which hit the target foil. The density of points is different for individual figures. Therefore, the histograms for X and Y coordinates were added for proper understanding of beam profiles. The dimension scales are the same for each figure intentionally. The histograms were taken from the data for individual directions. The displayed interval from -10 mm to +10 mm was divided into 1000 bins (resulting in 0.02 mm bin thickness). Each bin contains corresponding amount of ions incident on the target foil at a corresponding distance from the foil center. Thus, the count scales are varying depending on the beam dimension in corresponding direction. For focused beam directions (e.g. for vertical, Y focus) the count scales have higher values because more ions hit the foil near the center in that direction compared to the defocused beam direction where count scales exhibit lower values (ions were spread in wider range).*

6. PIXE analysis methods in the CENTA laboratory

A PIXE chamber was installed in the laboratory (September 2015) thanks to the IAEA funding. Details about the chamber can be found in [Zeman, 2016B]. The chamber is equipped with a sample holder capable of mounting four thick samples of about 2×2 cm dimension. The holder can be rotated around its vertical axis, so the angle how the incident beam should hit the sample can be fixed. For the charge collection, digital current integrator (Ortec Model 439) is used. A schematic top view of the chamber is shown in the Figure 60. The chamber itself is formed by a 6-way cross, where BEGe detector (CANBERRA) and a sample holder (NEC) are placed (detector endcap can be seen in Fig. 60 on the right photography). The detector has a carbon window (0.6 mm thickness). The detector is used for detection of emitted X-rays. It covers the energy range from 3 keV to 3 MeV, with energy resolution of 390 eV for 5.9 keV (^{55}Fe) and 1.8 keV for 1332 keV (^{60}Co). Necessary vacuum components (gate valves, turbo pump…) are installed as well.

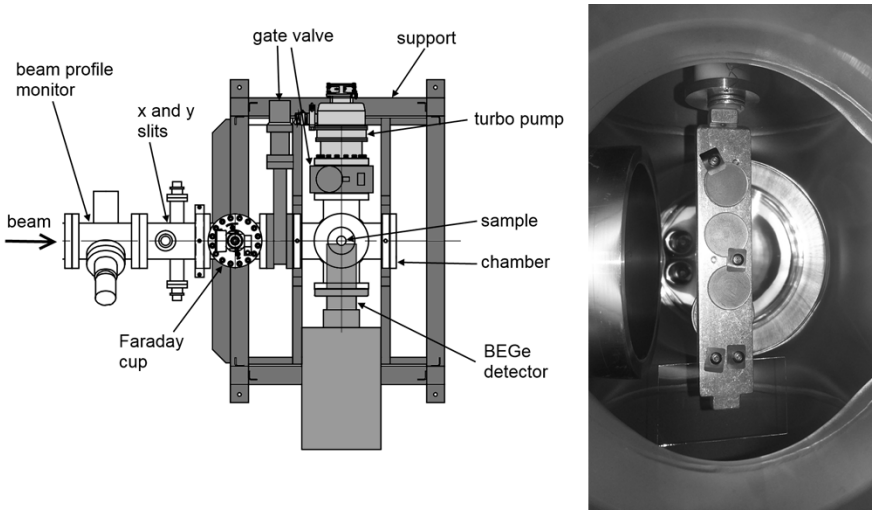

Fig. 60: Top view of the PIXE/PIGE chamber (left), and mounted pressed metallic powder samples inside the chamber (right) [Zeman, 2016B].

The original installation of detector was changed later in summer 2016. The detector was shifted outside from the chamber using additional pipe. The purpose was to improve the detector background. At PIXE measurements, depending on the parameters of used beam (ion type, energy, intensity), and also on the target angle to the incident beam, various background was observed in BEGe detector. The majority of this unwanted background

originates from the bremsstrahlung. The idea was to reduce this effect by shifting the detector further from the interaction point. This geometry is shown in the Figure 61.

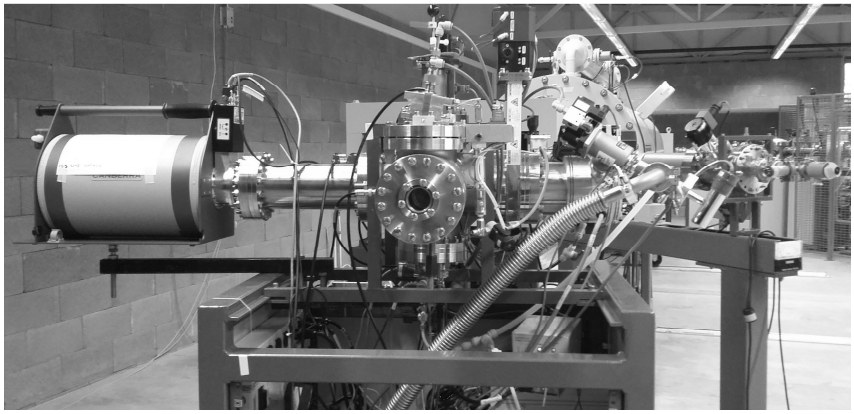

Fig. 61: BEGe detector shifted using additional pipe. The endcap distance from the center of PIXE chamber increased to 25 cm.

This shift had a positive effect on the background reduction (Figure 62). The same beam (3 MeV protons, for the same time as after the shift) used before, created on the glass sample higher background compared to the shifted situation. The increased distance, on the other hand, resulted in detection efficiency loss. This loss is acceptable, since the reduction of background brought better resolution for low energies. In Fig. 62, the gray spectrum (corresponding to BEGe shift) exhibit better resolution, so peaks in the beginning could be resolved better. Additional aluminum plates were mounted on the inner walls of the extension pipe. Their purpose is to shield the material from unwanted X – ray production by scattered beam in the pipe material (steel). Aluminum X – rays energies are below the BEGe detector sensitivity (3 keV). These plates are partially visible in the Figure 65.

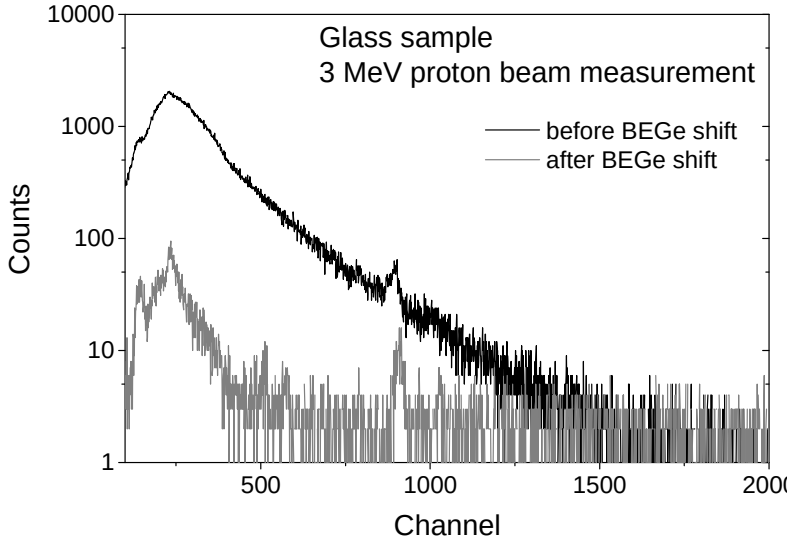

Fig. 62: Background spectra before (black) and after (gray) the BEGe detector shift.

The very important role in the PIXE measurements plays the sample holder. For analytical purposes, the total amount of ions which induce the X – ray (or gamma) emission have to be known precisely. This is obtained via the charge collection from the sample holder. The holder is electrically insulated from the chamber (there is a ceramic insulator, which can be seen in Fig. 60 on the right photography on the top of the sample holder). But a thin wire mounted to the sample holder is transferring the signal through the feedthrough on the top of the chamber. The incident ions bring a positive charge, which is collected by this wire. The signal is processed by Ortec digital current integrator with inaccuracy 1.81 % for low beam current (1 –2 nA). Depending on the charge state of incident ions, their amount can be calculated.

The qualitative PIXE analyzes do not require a knowledge of amount of incident ions, detector efficiency, additional sample – detector geometry information or information about sample structure. For qualitative purposes, simply an energy calibration of the detector is needed and an ion beam of certain energy (usually above 1 MeV) and intensity (~ nA) which is inducing the X–ray emission. Properly calibrated energy spectra can be interpreted in a way that certain elements are present in the specimen.

The quantitative PIXE analyzes are much more complicated. The knowledge of detection efficiency, geometry, sample structure and amount of incident ions is crucial. In contrast to classical gamma spectrometry, where peak areas can be directly converted into activities (if the detection efficiency is known), in PIXE measurements the spectra analyzes

are more complex and even ambiguous. Presence of elements with overlapping X – ray lines (e.g. K lines of lighter elements and L – lines of heavier ones) cannot be confirmed or disapproved and the qualitative analysis of such sample should be done with another technique for better understanding of its composition. Detailed information can be found e.g. in [Nastasi, 2015].

In the CENTA laboratory, after the PIXE/PIGE beamline installation, the technique development proceeded in 3 steps:

1.) BEGe detector calibration and efficiency determination
2.) Additional adjustment for proper charge collection
3.) PIXE spectra interpretation

6.1. BEGe detector calibration and efficiency determination

BEGe detector calibration was performed using calibrated X – ray variable sources and gamma ray sources. The calibration was performed for energy range up to ~ 60 keV. The range was selected in order to observe X – ray lines from the lower energy spectrum. In PIXE measurements, only X – ray lines up to 30 keV have been observed. The MCA was set to 2048 channels. More details are given further. The linear calibration curve is displayed in the Figure 62. The constants *A* and *B* play important role in samples analyzes using GUPIXWIN software for PIXE measurements evaluation (chapter 7).

The detector efficiency was determined using point sources measurements and detector efficiency modeled using DETMC software (created by The Guelph PIXE Group, Department of Physics, University of Guelph, Canada). This software was supplied with the GUPIXWIN software, which was a part of PIXE/PIGE beamline package. The DETMC program is a Monte Carlo tool for calculating Si(Li), SDD, and Ge detector efficiency. The detector dimensions, source – detector geometry and other information must be given into the software calculations. Software enables to define the source geometry for non-point sources as well. The efficiency for point source was in our interest. The point source detector efficiency output of the DETMC is displayed in the Figure 63 as a gray line. The output from the DETMC program contains values for both absolute and intrinsic efficiency

of BEGe detector. The intrinsic efficiency is important in PIXE spectra concentration evaluation process (section 6.4.).

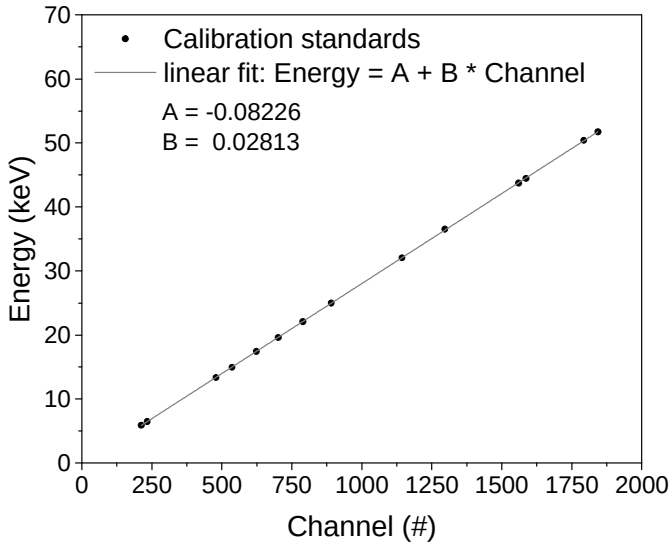

Fig. 63: BEGe detector energy calibration for 0 – 60 keV range

Calibrated point sources (with known activities) were placed at 25 cm distance from the detector endcap. Each point source was measured individually and spectra were analyzed in order to determine peak areas and then calculate the absolute efficiency. List of energies used for detector efficiency calculation is given in the Table 5. Unfortunately, the sources' energies that were at disposition started at ~ 30 keV, thus the efficiency for lower energies can be taken only from the model. At energy 11.1 keV the efficiency drops because of germanium K-absorption edge. Energy of photon in close proximity to this value is more likely to be absorbed.

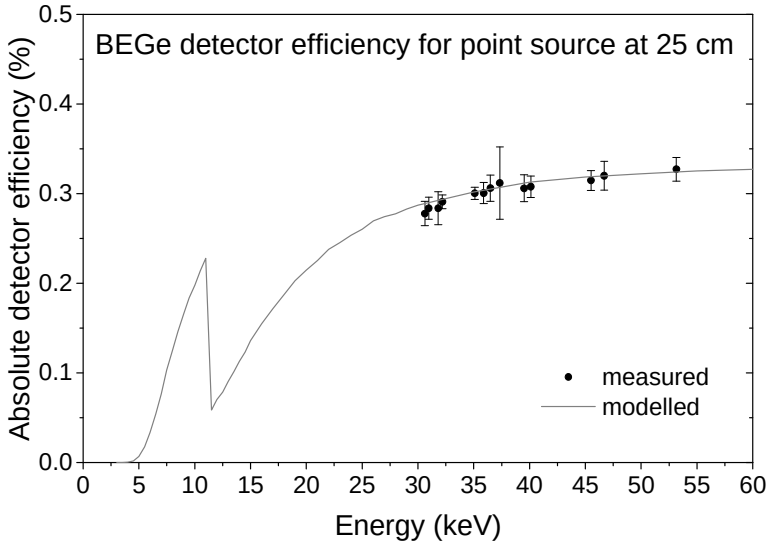

Fig. 64: BEGe detector efficiency for point source at 25 cm distance. The gray line represents the modelled values (DETMC program). The black dots are calculated efficiencies from measurements. Areas of some peaks used for evaluation were small, therefore some values exhibit higher uncertainties (e.g. 37.35 keV).

	Energy (keV)	Efficiency (%)	Uncertainty (%)
^{152}Eu	30.63	0.28	0.01
^{152}Eu	30.97	0.28	0.01
^{137}Cs	31.82	0.28	0.02
^{137}Cs	32.19	0.29	0.01
^{133}Ba	35.09	0.30	0.01
^{133}Ba	35.90	0.30	0.01
^{137}Cs	36.49	0.31	0.02
^{137}Cs	37.35	0.31	0.04
^{152}Eu	39.52	0.31	0.02
^{152}Eu	40.12	0.31	0.01
^{152}Eu	45.51	0.32	0.01
^{152}Eu	46.69	0.32	0.02
^{133}Ba	53.16	0.33	0.01

Table 5: List of energies used for detector efficiency determination with calculated efficiencies

The general fall in X-ray absorption coefficient with increasing energy of incident photon is interrupted by a sharp rise when the energy is equal to the binding energy of an

electron shell (K, L, M, etc.) in the absorber (Fig. 64). In our case the absorbing material is germanium. The least energy at which a vacancy can be created in the particular shell is referred to as “edge” or critical excitation energy. At this energy for germanium (11.1 keV) the efficiency drops because of this effect. Characteristic X-ray lines are generated when an ‘initial’ vacancy in an inner shell, created by X-ray or electron excitation, is filled by transfer of an electron from another shell, thus leaving a ‘final’ vacancy in that shell; the energy of the line is equal to the difference in binding energies of the shells with the ‘initial’ and ‘final’ vacancies.”

6.2. Additional adjustment for proper charge collection

As mentioned previously, the information about accurate amount of particles which induce the X–ray emission have to be known precisely in order to perform quantitative analysis. Incident ions interact with the sample which is mounted on a sample holder inside the PIXE chamber. The sample holder is conductively connected via thin spring wire with digital current integrator (DCI). The DCI is connected with the software which collects the data during the measurements (spectra, time period, settings of MCA …). The total amount of ions is important in element concentration calculations. This process is explained later, in section 6.4.

First PIXE measurements (starting in September 2015) were performed without charge collection in order to obtain information about qualitative composition of selected materials. Results can be found in [Zeman, 2016B] (Appendix A).

For quantitative analyzes, the charge collection had to be done precisely. The original setup for sample holder inside the chamber (Fig. 60, right photography) did not include system for secondary electron suppression. This phenomenon plays important (and negative) role in the charge collection process. Impact of positive ions causes emission of secondary electrons. In this process, as the result of electrostatic induction, the irradiated material is charged positively. This excess of positive charge is collected by the DCI together with the positive charge brought by the incident ion beam. Therefore, after conversion of collected charge, it seems that the beam is formed by more particles than it really is. Consequently, misleading results are obtained from sample composition analysis.

The negative effect of secondary electrons emission can be suppressed using more methods. In the CENTA laboratory, option for secondary electrons suppression electrode was chosen.

Secondary emitted electrons suppression electrode

The idea of this device is to suppress the secondary emission of electrons from the target material in order to obtain proper information about amount of incident particles. The electrode was designed so that the beam could freely reach the sample. Copper was used as structure material and the whole electrode is formed by one rod bend into desired shape. The electrode design is shown in the Figure 65. The photographs were taken during the electrode installation into the chamber. The electrode was painted with carbon paint (suitable for vacuum conditions). Purpose of this paint is to avoid the scattered beam to induce X – ray emission from the electrode's material. Since the BEGe detector is not sensitive to X – rays below 3 keV, the carbon from the paint is not visible in measured spectra.

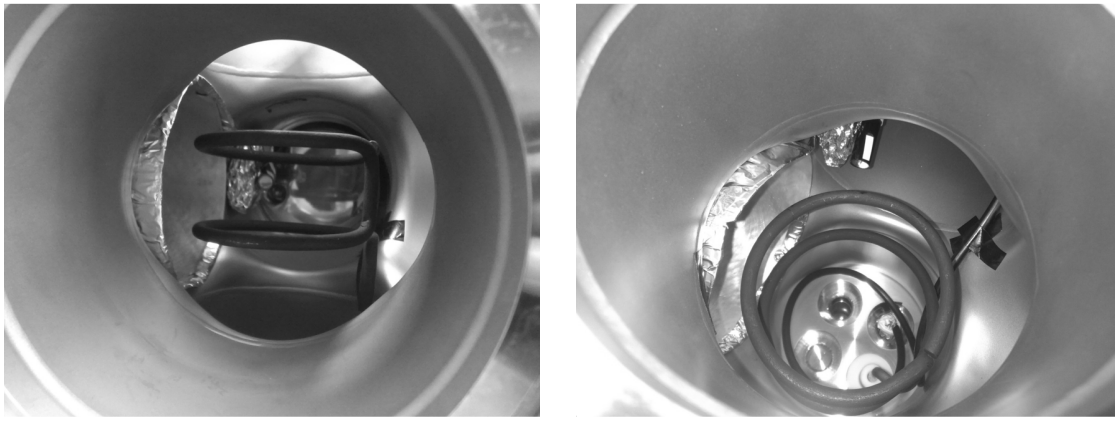

Fig. 65: Front and top view of the suppressor electrode as it was installed into the chamber

The design of this suppressor electrode is based on SIMION simulations. More combinations of rod thickness, diameter of the rings and vertical distance of the 2 rings were simulated. Finally, 5mm thick rod, 80 mm diameter of rings and their vertical distance of 30 mm came out as the most suitable solution for the chamber conditions. The SIMION model and results of simulations are shown in the Figure 66.

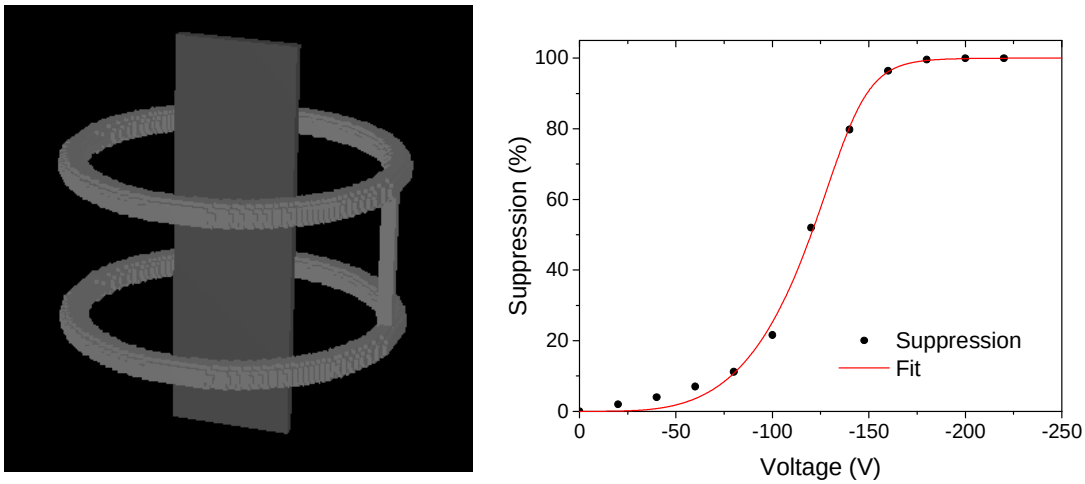

Fig. 66: SIMION model of secondary electrons suppression electrode. The model in 3D SIMION view (left) and result of simulations for electrons suppression depending on the voltage of the electrode (right). The suppression was calculated as ratio of difference between amount of created electrons and escaped electrons to amount of created electrons.

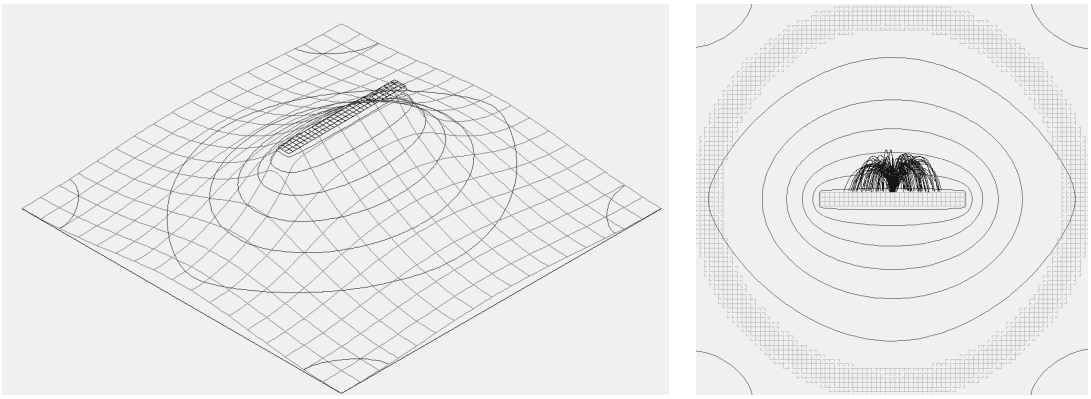

Fig. 67: SIMION electrostatic potential field surrounding the sample holder. The electrostatic potential of the suppressor electrode was -400V. 3D side view with sample holder in the middle at 0 V (left) and top view with rings surrounding the sample holder in the middle with emitting electrons (right). Electrons (energy 100 eV) were produced in the middle of the sample holder. The suppressor field forced them to turn back on the sample holder ("fountain" trajectory).

The electrostatic potential field inside of the rings was, more-less, independent on the vertical straight rod, thus this rod was omitted from the model. Secondary electrons were simulated as source of electrons in the middle of the sample holder. The energy of secondary electrons was set to 100 eV. This value was overestimated. Considering Figure 68 [Dapor, 2016], the amount of electrons with higher energy rapidly drops. The energy of

simulated electrons was simulated with quite wide Gaussian distribution (mean 100 eV, FWHM = 30 eV). The source position had also Gaussian distribution (1 mm FWHM).

The electrostatic potential fields are shown in the Figure 67. The equipotential levels are displayed as deformed circles around the sample holder. In the left figure, the side sectional view is displayed with grounded sample holder in the middle (0 Volts), and suppressor rings around are forming decreasing electrostatic field down to -400 Volts. On the right, the top view of the system is shown. The electrons were produced in the middle of the sample holder under condition mentioned before. The repulsive electrostatic potential curved their trajectories, so the electrons got back to the sample holder (the trajectories look like a fountain, black lines in the middle of the figure).

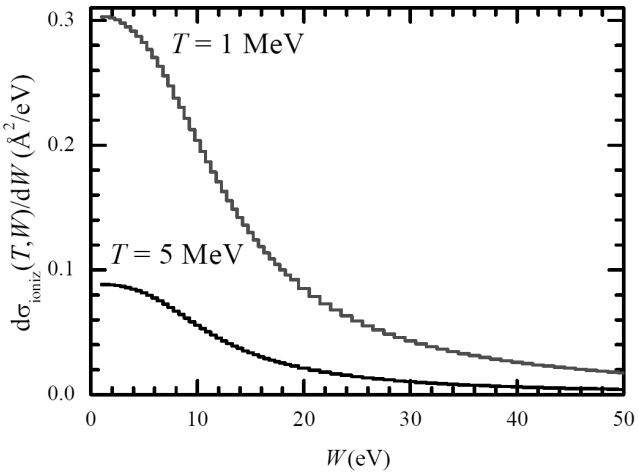

Fig. 68: Energy distribution of secondary electrons produced by 1 MeV and 5 MeV protons in PMMA [Dapor, 2016].

6.3. PIXE spectra interpretation

In the CENTA laboratory the PIXE measurements are being performed using proton or helium beam. Energy of protons is chosen as 3.052 MeV (TV = 1.5 MV, 1+ charge state) and energy of helium 4.552 MeV (TV = 1.5 MV, 2+ charge state). The intensity of beam is rather low (hundreds of pA to 20 nA as maximum) for the purpose of suppressing bremsstrahlung. The low intensity of beam is better for resolution as well. The collected charge for a single measurement is usually ~ 2 μC or less, depending on the actual sample. The sample tilt angle is adjustable in horizontal direction and 2 positions are preferred; 10°

and 45°. This is the angle between the sample normal and the beam axis. Option for one of positions depends on the specimen.

X – Rays are detected by BEGe detector and the signals are processed through preamplifier into MCA and software which collects the data. Measured spectra are analyzed using software GUPIXWIN, which was developed in University of Guelph, Canada [Maxwell, 1989], [Maxwell, 1995], [Campbell, 2000], [Campbell, 2010]. GUPIXWIN is a program for the non-linear least-squares fitting of PIXE spectra and the subsequent derivation of element concentrations from the areas of X-ray peaks in the spectrum. The output from the program can be seen in the Figure 69 (exemplary figure).

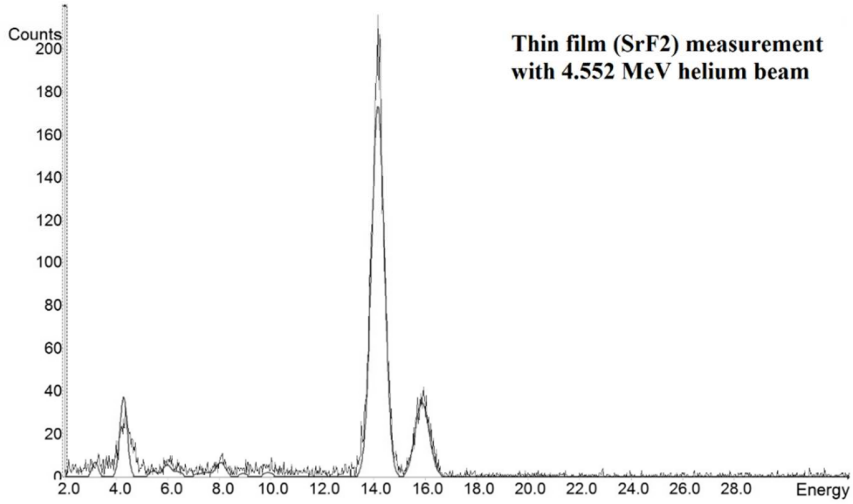

Fig. 69: GUPIXWIN fit of thin film (SrF_2) measured spectrum

The GUPIXWIN fit the spectrum considering many factors. The database includes: X-ray energies and emission rates, element densities and atomic weights, ion induced X-ray production cross-sections, proton stopping powers, photoelectric cross-sections and X-ray mass attenuation coefficients. Within the calculations, GUPIXWIN computes also corrections for escape and summation peaks.

A special file with information about detector have to be created (or modified) by user. The BEGe detector dimensions, materials and structure information have been used to create such file for GUPIXWIN. The software calculates the line shape for use in fitting the spectrum, the detector's relative efficiency, which is needed both in spectrum fitting and in determining concentrations; the weighting scheme to be used in the least- squares fit of the spectrum.

6.4. PIXE concentration calculation

Peak areas could be converted to element concentrations in absolute way, i.e., without standards, if the aspects of the analyzing system (solid angle, detector thickness, beam proportions, etc.) are given into GUPIXWIN. That is a "fundamental parameters" approach. Alternatively all analyses could be conducted relative to single-element standards or to standard matrices containing various trace elements. The X-ray intensity or yield (principal X-ray line), *Y (Z,M)* for an element *Z* in a matrix *M* can be written:

$$Y\ (Z, M) = Y_{1t}\ (Z, M) * \ C_Z * Q * f_q * \ \Omega * \varepsilon * T \qquad (13.)$$

where:

Y_{1t} is the theoretical (from GUPIXWIN database) intensity or yield per micro- Coulomb of charge per unit concentration per steradian;

C_z is the actual concentration of element *Z* in matrix M;

Q is the measured beam charge or quantity proportional thereto; if the latter, then f_q converts the *Q* to micro- Coulombs; if the former then f_q is 1.0 assuming proper electron suppression at the target;

Ω is the detector front face solid angle in steradians;

ε is the intrinsic efficiency of the BEGe detector;

T is the transmission through any filters or absorbers between target and detector.

The equation (13.) includes multiple possible factors which influence the final element's concentration. In the CENTA laboratory, no filters are used between the sample holder and detector, thus *T* equals to 1.0. Parameters f_q and Ω can be combined into an instrumental constant *H*, which characterizes the PIXE detection system. The approach taken in GUPIXWIN employs the physics database together with a single quantity of H value. Depending on the system characterization this H value is a constant or it is function of X-ray energy. Implementing these facts, the element concentration using the equation (13.) can be calculated as follows:

$$C_Z = \frac{Y\ (Z, M)}{Y_{1t}\ (Z, M)\ * \ H * Q * \ \varepsilon} \qquad (14.)$$

Measured X-ray yield is converted to concentration for all elements fitted. The detector efficiency was determined in chapter 6.1. In the laboratory, both thin and thick samples are being analyzed. Thin samples are considered as samples with thickness insufficient to stop the beam completely. Incident particles (in our case protons or helium ions) can penetrate through the sample. These ions have to be collected as well, so a Faraday cup was placed at the end of the beam line. For thin samples, this Faraday cup's and sample holder's charge signals were collected by the current integrator. Thickness of thick samples is sufficient to stop the beam, thus no ions penetrate through these samples and the whole charge is collected from the sample holder. The necessity of secondary electrons suppression is described in section 6.2.

The H values for thin samples were determined using thin standards ordered from the MICROMATTER ™ Company [MicroM, 2017]. Thin films deposited on Mylar foils with known concentration of elements forming these films were analyzed. The H values for thick samples were determined using samples prepared in our laboratory. These samples consist of pressed clean metallic powders (supplied by Alfa Aesar®). Single – element samples were prepared from Fe, Cu, Zn, Ag powders (purity more than 99.9 %). Each metallic powder sample was prepared using a pneumatic press to form flat, coin-like, pellets. This samples were analyzed using proton beam and determining the H value for thick samples. Results for thin and thick samples are summarized in the next chapter.

In well-defined system the H value is a constant. However, small Z dependences of H value can arise from database imperfections or from imperfect knowledge of filters or absorbers or detector efficiency. In GUPIXWIN, it is possible to use a file of pre-prepared H versus X-ray energy values. The software then uses this file to interpolate an appropriate H value for each element Z. Consequently, the concentration C_Z of element present in the sample can be determined using GUPIXWIN. The software assigns corresponding $Y(Z,M)$ and $Y_{1t}(Z,M)$ values to measured peak areas for individual X-rays emitting by elements forming the measured sample.

7. Results of the analyzes

7.1. Qualitative analysis of Slovak coins

The very first PIXE analyzes were performed on Slovak coins. There were no adjustments of the PIXE chamber within these analyzes, thus results were preliminary, containing information on the presence of elements in the investigated samples. For the purpose of these analyzes, pressed samples of powders comprising of multiple elements were prepared which have been used as PIXE laboratory standards. The standards used clean metallic powders, supplied by Alfa Aesar®, and they were used throughout the measurements. The samples were prepared by mixing Ti, Fe, Cu, Zn and Ag powders in various proportions. The purity of the powders was as follows: Ti (99.99 %), Fe ([99 %), Cu (99.9 %), Zn (99.9 %) and Ag (99.9 %). Each metallic powder mixture was prepared using a pneumatic press to form flat, coin-like, pellets. A relative elemental concentration of each sample was calculated as a ratio of the element powder mass to the total mass of the mixture. The relative concentrations of elements are presented in Table 6.

Sample		m (mg)	Ratio (%)
PIXE2	Fe	1367.36	62.19
	Cu	831.43	37.81
PIXE3	Ti	287.64	18.65
	Fe	694.57	45.03
	Cu	282.03	18.29
	Ag	278.10	18.03
PIXE4	Fe	326.06	19.56
	Cu	1107.75	66.45
	Zn	233.34	14.00

Table 6: Composition of prepared pressed metallic powders.

For each sample, labeled as PIXE2, PIXE3 and PIXE4, at first, powders were weighed on digital scale. Then they were mixed to form 3 individual samples. Each mixture was afterwards pressed by pneumatic press to form flat, coin-like, pellet. Relative elemental concentration of each sample was calculated as ratio of the element powder mass to total mass of the mixture.

These samples served as a reference material for comparison of further PIXE qualitative analyzes. Details can be found in Appendix A [Zeman, 2016B]. Results of PIXE analyzes of Slovak coins are shown in Figure 70.

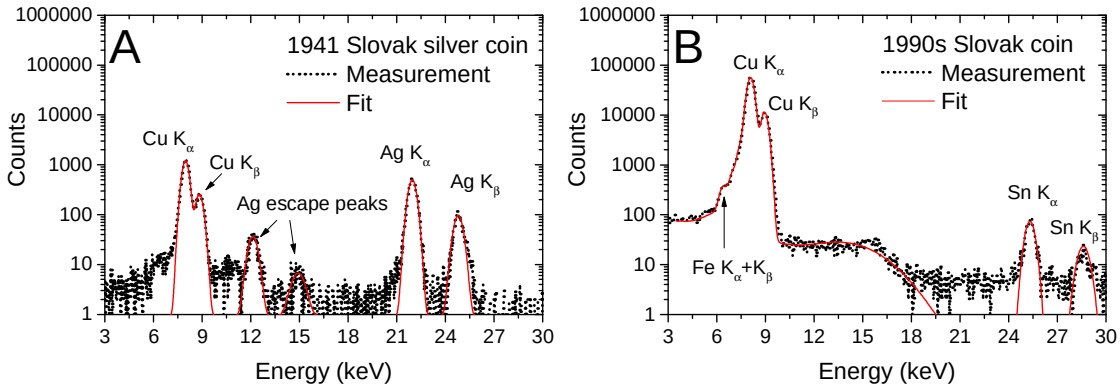

Fig. 70: PIXE analyzes of Slovak coins. Older silver coin from 1941, and a younger one from 1990s were analyzed. The spectra show presence of marked elements [Zeman, 2016B].

Measurements of two Slovak coins using 4.5 MeV helium beam were performed. A silver Slovak coin of nominal value 20 crowns which was issued in 1941 during the Slovak State, and a Slovak coin of nominal value 1 crown which was used as a former currency (from 1993 to 2004) in the Slovak Republic were analyzed. GUPIXWIN was used for the composition determination of these coins. The 1941 Slovak silver coin was measured using 50 pA beam intensity for 10 min (Fig. 70A). The measurement showed presence of silver and copper characteristic X-ray lines. Since the concentration of silver in this coin was higher than 50 %, two escape peaks were observed in the spectra. The copper Kα and Kβ lines were sufficiently resolved. There was an indication of iron occurrence. At 6.4 keV, which corresponds to the iron Kα line, possible peak appeared, but the presence of iron in the spectrum is questionable. The measurement of 1990s Slovak coin (Fig. 70B) proved presence of copper, tin and small amount of iron. This coin was measured using higher beam intensity (200 pA), and the measurement time was 20 min. The bremsstrahlung background was more than an order of magnitude higher than for the silver coin measurement. The estimated concentration of silver in the Slovak silver coin was 65 ± 5 %, and the rest was copper. The Slovak coin from 1990 had a dominating copper concentration of 85 ± 5 %, and the rest was tin (14 %) and iron (<1 %) [Zeman, 2016B].

7.2. Determination of H values for thin and thick samples

The H values for thin samples were determined from measurements of thin films supplied by MICROMATTER™ Company. All MICROMATTER™ standards are prepared by vacuum deposition resulting in a highly uniform deposit. The analyzed films were deposited on a 3.5 micron Mylar® polyester film. The individual films' thicknesses are recorded in Table 7. The manufacturer declares the thickness (in μg/cm^2) with 5.0 % accuracy. For better imagination, these values were converted into nanometers, as well. The geometry setup scheme for the measurements is displayed in Figure 71. The figure displays a top view of the chamber with sample holder, beam direction and BEGe detector position. The measurements were performed using the 3.052 MeV proton beam, and later using 4.552 MeV $^4He^{2+}$ ion beam. The intensities of the beams could have been quite high, 2 – 5 nA (comparing to the thick targets), because the beams were penetrating through the films keeping the undesired effects low.

film	Fe	Cu	Ga	Sr	Cd	Sn
Thickness (μg/cm^2)	49.8	48.8	23.4	54.9	45.3	52.4
Thickness (nm)	63.2	54.5	39.6	208	52.4	72.1

Table 7*:* The thickness of thin films stated by the manufacturer with 5.0 % accuracy (μg/cm^2) and calculated values in nanometers.

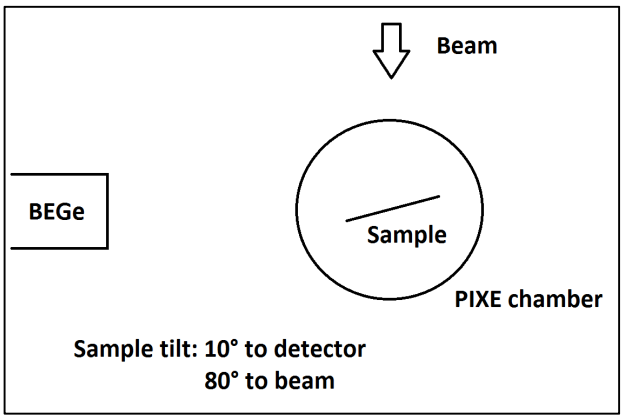

Fig. 71: A scheme of the geometry setup for thin film measurements (a top view).

For the purpose of H value determination, the thin films were analyzed several times with different charge collection (from 0.5 to 2.0 µC (Coulomb). The aim was to compare results from more than just one measurement of a single film. The exemplary PIXE spectra of thin Sn film measurement with 3.052 MeV protons are displayed in Figure 73. The collected charge was 1.0 µC. Measurements with helium beam were performed with doubled charge collection to obtain X–ray spectra induced by the same amount of particles, i.e., for the Sn film analysis with helium beam, 2.0 µC were collected. The charge was collected both from Faraday cup placed at the end of beam line and the sample holder. Since the samples are thin the beam penetrates through the material and charge of such particles has to be collected in order to know the amount of particles which induced X–ray emission in the specimen.

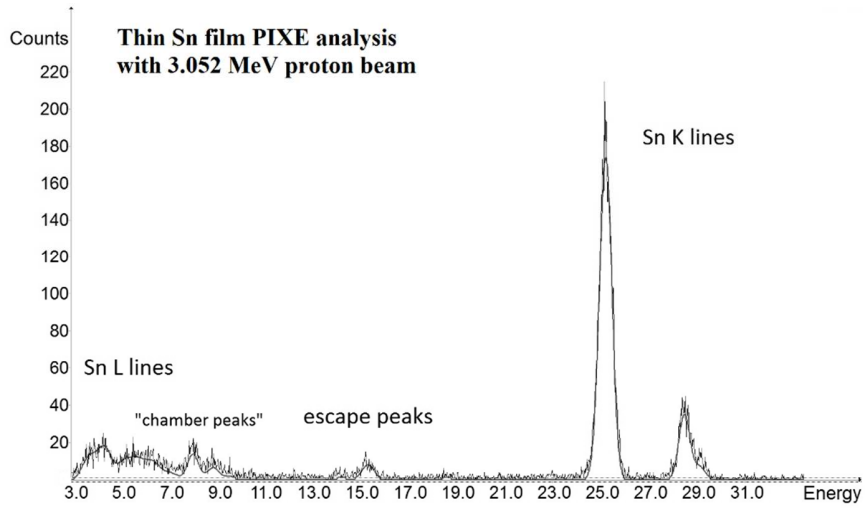

Fig. 72: Example of PIXE spectra and fit processed by GUPIXWIN for thin pure Sn film analysis with protons. The total charge collected was 1.0 μC. The "chamber peaks" originate from X–rays produced by scattered beam. Protons scatter on the sample, and they consequently interact with the chamber construction material (mostly Fe, Cu and their mixtures).

Figure 63 in section 6.1 displays energy calibration of the BEGe detector. Constants *A* and *B* were used as input for spectra calibration in GUPIXWIN. A file with intrinsic efficiency suitable for GUPIXWIN was created using DETMC values. According to the equation 14 (section 6.4.), for known intrinsic efficiency of BEGe detector and collected charge, the H value can be determined for samples with known concentration.

The PIXE spectra of thin films were analyzed by GUPIXWIN in a way that the spectra were fitted so the concentration (layer thickness) of the element corresponded to the

manufacturer's declaration (Table 7). This was done by looking for proper H value for each spectrum obtained from measurements of individual films. Values from multiple measurements of the same film were averaged and corresponding uncertainties were calculated. The total uncertainty consists of charge collection and tilt angle uncertainty (3.5%) and fitting uncertainty (~ 2–6 %) varying for individual spectra.

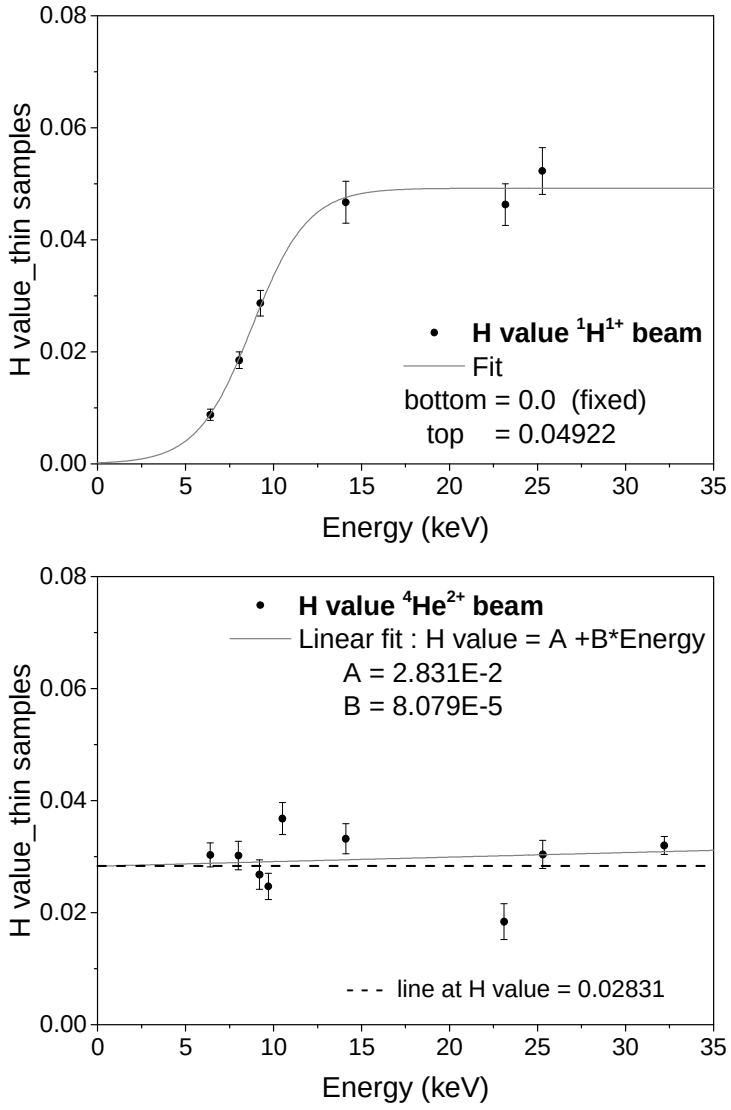

Fig. 73: Results of H value determination for thin standards using 3. 052 MeV proton and 4.552 MeV $^{4}He^{2+}$ beams. For the proton beam the energy dependency was measured as can be seen in the upper figure. The helium analyzes exhibit more-less constant H value. A dash line at H value = 0.02831 was added to observe the difference between the fit and the constant value.

H values for thick samples were determined from PIXE analyzes of the pressed powder samples prepared in our laboratory. The weights of pure Fe, Cu, Zn, Ag powders (purity more than 99.9 %) used in individual samples are listed in Table 8. Each powder was consequently pressed into small pellets with 1.5 cm diameter. The thickness of the pellets has been varying by ~3 mm, depending on the amount of used material and power of the hydraulic press (~15 tons).

Powder	Fe	Cu	Zn	Ag
Weight (g)	2.07	2.08	1.35	1.52

Table 8: Weights of powders used for preparation of thick-pressed samples.

PIXE analysis of such prepared pellets was carried out using 3.061 MeV proton beam. The thickness of thick samples was sufficient to stop the beam, thus the beam charge was collected only from the sample holder to obtain the information about amount of protons which caused X–ray emission. The GUPIXWIN fitting procedure was the same as for thin samples, i.e., H value was varying until the proper concentration in each sample was reached. Samples were measured more times and average H values for individual K–line energies are shown in Figure 74.

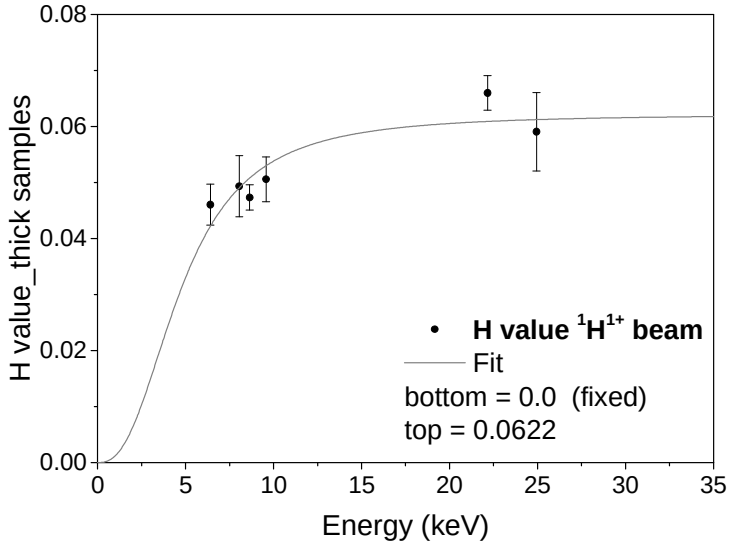

Fig. 74: Results of H value determination using 3.061 MeV proton beam.

The H value uncertainties are little bit higher comparing to thin samples. One of the reasons is that H values (e.g. for 6.4 keV iron K_α line) from individual measurements were more spread comparing to the thin samples. The other reason is that the thick H values were determined also for K_β lines (9.572 keV zinc and 24.942 keV silver) which exhibit higher uncertainties in fitting procedure (lower peak areas). The uncertainties in Figure 74 vary between 5–12 %.

The reason that the thick H values are determined from 3.061 MeV proton measurements is that there were some difficulties with Alphatross source. The proton beam (used for pressed powders analyzes) was produced with MC-SNICS from TiH target. The ion source has different settings of injection energy therefore the energy slightly differs from the 3.052 MeV value from the Alphatross. The Alphatross maintenance problems caused that the thick samples have not been analyzed yet with helium beam (April 2017). Hopefully these issues will be overcome soon.

Results for proton beam measurements are compared in Figure 75. The thick samples exhibit higher H values. A possible explanation can be in different X–ray self-absorption by samples. The GUPIXWIN in calculations for thick samples uses standard values for density of material. The thick samples have different densities since the material was pressed a by hydraulic press. This difference could lead to different X–ray yields used in equation 14 for element concentration calculation.

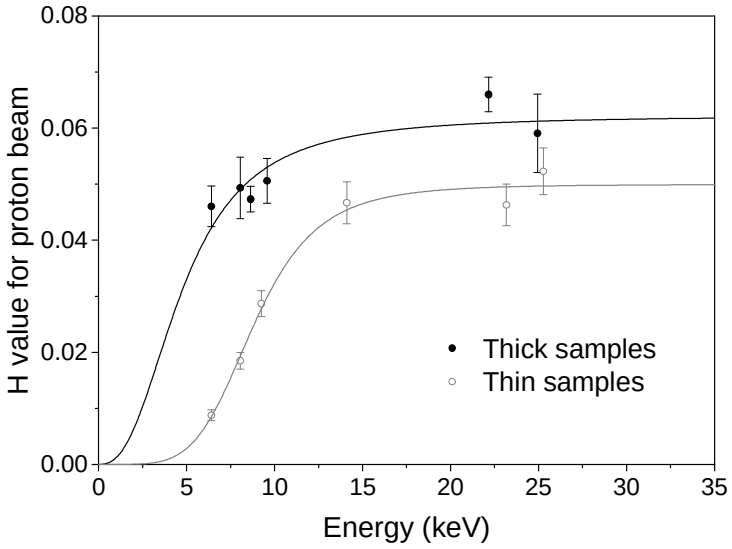

Fig. 75: Comparison of H values for thick and thin samples using proton beam for PIXE.

7.1. Concentration of iron in a rat brain sample

The CENTA laboratory has already been cooperating with several research institutions. In cooperation with Medical faculties of the Comenius University in Bratislava and Martin a rat brain slice was received to determine iron concentrations and map its distribution in the slice. The aim of this study has been to evaluate concentrations of iron in this slice on various spots. It is expected that the iron in the rat brain was produced by electromagnetic radiation similar to one generated in mobile telephones. The observed effects in the brain tissue may be due to electromagnetic radiation, which causes agglomeration of iron in the tissue. A map of iron distribution with measured concentration (which may be regarded as a simple nuclear microscopy map) should provide important information for further medical research. At present it is not well understood how this iron agglomerates in the brain tissue, but there are hypotheses that the electromagnetic radiation may cause this effect, [Terzi, 2016], [Kaplan, 2016], [Kostoff, 2013].

A thin slice of the rat brain (~5μm) was prepared for investigation. The slice was attached on a thick silicon wafer. Consequently, due to SEM measurements, a thin gold layer (~ 30 nm) was deposited on the surface of the tissue. The sample was then inserted into the PIXE chamber of the CENTA laboratory for investigations.

The rat slice represents a special type of intermediate sample which can be handled by the GUPIXWIN software. The brain slice with a thin gold layer on the top and mounted on a thick substrate can be specified in GUPIXWIN's input parameters. The concentration of elements present in the sample can be evaluated by measuring the number of X–ray inducing particles (charge collection) and by knowledge of H value for such sample (equation 14). For the layered samples (a similar to the slice) the H value has not been, however, determined. For this purpose, a layered standard material (of known elemental composition in each layer) was prepared and analyzed so a proper H value dependency on the energy of X–rays could be determined.

For the rat brain analysis it was decided to follow special procedures. Several standard samples were prepared and analyzed by PIXE using the 3 MeV proton beam. Samples were prepared in a way so that they copy the properties of the rat brain slice sample. Firstly, solutions with known concentrations of iron were prepared. Next, droplets of solutions were dropped on a silicon wafer. After drying, these samples were analyzed in PIXE

chamber. Consequently, the measured spectra of standard layered samples were processed by the GUPIXWIN software. Important information on the peak areas was obtained and a dependency of these areas on the element concentration in each sample was plotted. Finally, the concentration of iron in the rat brain was determined using these values. To each Fe Kα peak area (from multiple measurements of the rat brain slice on different spots) a concentration from standard samples measurement was assigned. Results are shown in Fig. 76.

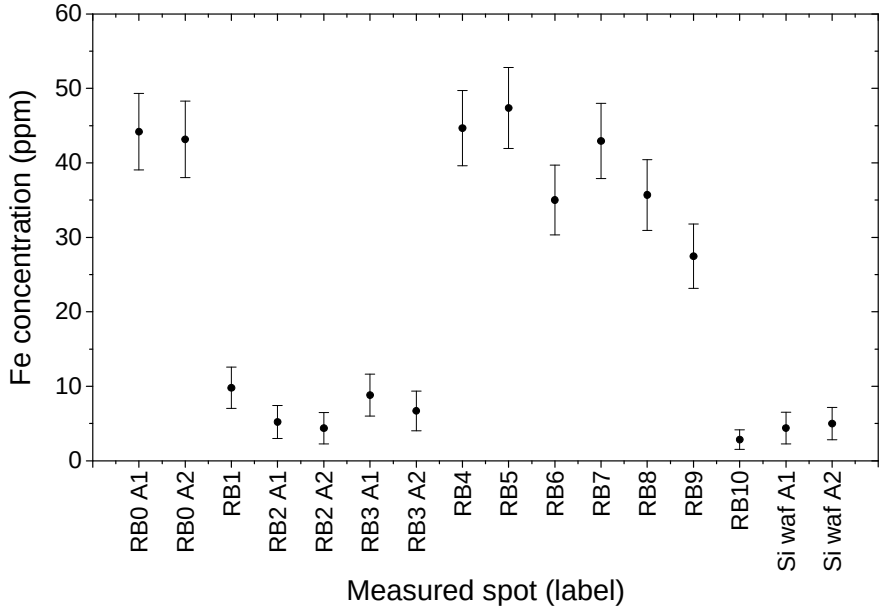

Fig. 76: Iron (Fe) concentration in rat brain sample. Measured spots on the sample are labelled as RB0 - RB10, Si wafer was measured as well. Some of the positions were analyzed twice (A1 and A2 labels). The evaluated Fe concentration for corresponding spots exhibits the same values.

All spots were analyzed under the same beam and charge collection conditions. The beam intensity was 0.5 nA, charge collection was set to 0.2 μC, and the geometry was the same as in Figure 71. The incident proton beam diameter was ~1.5 mm. This was achieved by careful and tedious setting of whole beam line and ion optics devices. During the measurements the sample was moved in the vertical position. The horizontal position of the beam spot was adjusted in a way that the sample was removed from the chamber, manually shifted on the sample holder and put back inside the chamber for further analysis. The exemplary spectrum from measurements is shown in Fig. 77. Table 9 contains values for determined Fe concentrations. The uncertainties for individual spots were calculated and evaluated. The main source of uncertainties was the statistics in the fitting process. Some

spots, especially with low Fe concentrations (<10 ppm), positions RB1 – RB3, RB10 and Si wafer, have uncertainties from 28% to 48%.

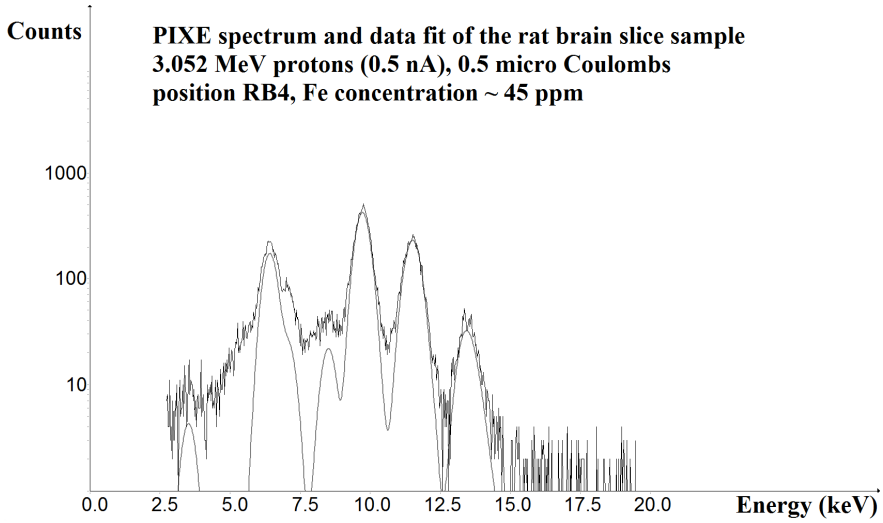

Fig. 77: Measured PIXE spectrum of rat brain slice sample (position denoted as RB4). The output from GUPIXWIN contains spectrum data (black line) and fit values (gray line). Au L lines (9.7, 11.4 and 13.4 keV) and Fe K lines (6.4 and 7.1 keV) were observed together with 3.3 keV escape line (from 13.4 keV Au L line) and 8.6 keV escape line (from 9.7 keV Au L line).

Measured spot	Fe concentration (ppm)	Uncertainty (ppm)
RB0 A1	44.19	5.13
RB0 A2	43.16	5.15
RB1	9.79	2.77
RB2 A1	5.21	2.21
RB2 A2	4.36	2.10
RB3 A1	8.81	2.80
RB3 A2	6.70	2.66
RB4	44.68	5.05
RB5	47.38	5.43
RB6	35.02	4.70
RB7	42.94	5.05
RB8	35.70	4.74
RB9	27.46	4.33
RB10	2.83	1.32
Si waf A1	4.38	2.12
Si waf A2	4.98	2.15

Table 9: Values of iron (Fe) concentration in rat brain slice on different spots. Concentration determined by PIXE measurement with proton beam. Uncertainties are displayed in ppm and % for better imagination. All spots were analyzed under the same conditions. Therefore low concentration are determined with higher inaccuracy (low peak areas).

The values for concentrations above 25 ppm were calculated with 11 – 15 % uncertainties. For better statistics, a different set of measurements with higher charge collection should be performed in order to determine the concentration with better accuracy.

A map of surface iron displacement is plotted in Fig. 78. Important note is that only 12 different spots on total sample area ~ 4 cm^2 were analyzed. The map was done by computer simulation with regard to determined concentrations of measured spots. For a more precise surface distribution of Fe in the sample, more spots should be analyzed using a raster scan device for sample positioning. Currently, the vertical sample position is adjusted by manual manipulation with sample holder rod (from the top of the PIXE chamber). The sample cannot be moved in the horizontal direction at present (April 2017). The horizontal "movement" was achieved by a manual sample shifting. Nevertheless, the results are quite interesting, clearly showing a gradient, i.e. a non-uniform iron displacement in the investigated rat brain slice. Surprisingly the observed Fe concentrations are quite high. Medical evaluations are in progress, as well as preparations of new brain slice samples.

The obtained results have confirmed that the PIXE beam line in the CENTA laboratory can be used for nuclear microprobe research in the near future.

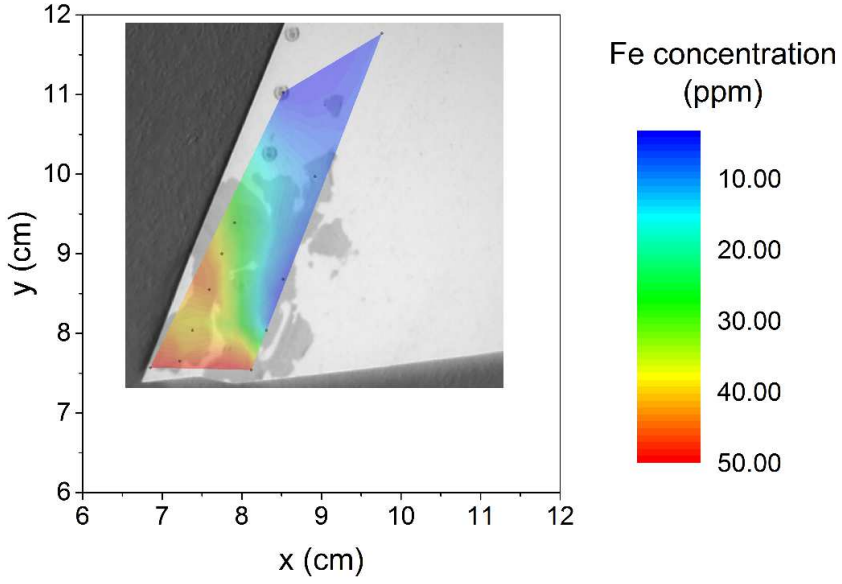

Fig. 78: Fe concentration map of the rat brain slice. The sample photograph (converted into negative and grayscale) is shown in the background. Si wafer is bright and the brain slice forms darker areas. Although only 12 different spots (in mutual distance of several millimeters, black dots) were analyzed, the picture shows a clear gradient in the Fe distribution in the sample. The scale is displayed from 6 to 12 cm in both directions. The coordinates are chosen with regard to sample holder position.

7.2. Ongoing experiments

Many more samples were analyzed in the laboratory using the PIXE system. Some of the spectra were obtained before the mentioned adjustments (detector shift, electrode installation). These experiments are ongoing, and the samples will have to be measured again. Only some qualitative information about samples' composition can be retrieved from current status of these analyzes (April 2017).

PIXE analysis of meteorites

Canyon Diablo iron meteorite from Arizona was analyzed by helium PIXE beam. Iron and copper peaks are well visible. New analyses are in preparation with adjusted geometry and lower beam intensity to suppress the background. Plan is to perform PIXE measurement in new condition in the chamber with proper charge collection and lower background to possibly observe more elements. Absolute concentration of individual elements will be hopefully determined after applying H values for thick samples (chapter 7.2.).

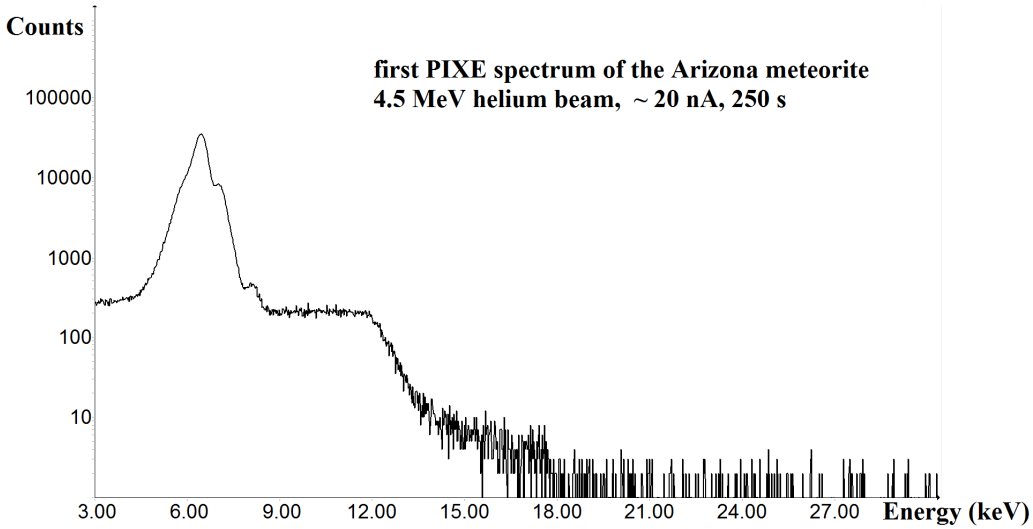

Fig. 79: First PIXE spectrum of the Canyon Diablo iron meteorite from Arizona. PIXE conditions as described in figure. The measurement was performed with high beam intensity without charge collection and before the adjustments in the PIXE chamber.

Meteorites are included into the group of rare samples, therefore a non-destructive analysis is preferred to retrieve more information about their elemental composition. Both PIXE and PIGE techniques can bring more light into this area. On the other hand, the necessity for proper setting of detection system is evident as well as proper handling the

data acquired via such measurements. Therefore the whole procedure with determination of the H values and the detector efficiency had to be performed carefully (chapters 6.1. and 7.2.).

PIXE analysis of uranium in zirconium mineral

Zirconium mineral was analyzed by PIXE using the proton beam. The GUPIXWIN spectrum is shown in Figure 80. Plausible presence of more elements is described in the figure comment. This material is being analyzed in order to test whether via PIXE technique it would be possible to determine uranium content in this mineral. The idea is to detect low concentrations of this element in various geological samples as well as in reactor fuel materials (fast measurements in the case of uranium smuggling). The recent measurements showed that GUPIXWIN was able to find uranium peak in the measured spectrum, however, it has not been possible yet to calculate its concentration because uranium L-lines lie in the region of zirconium K-line energies. It seems that a different approach should be taken in order to search for uranium in zirconium minerals, namely a use of a high resolution Si detector for low-energy X-rays.

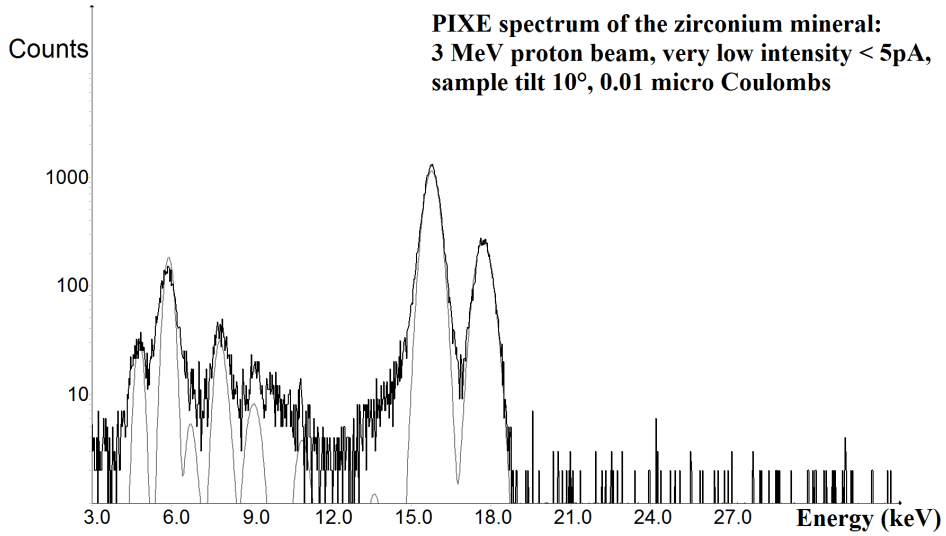

Fig. 80: PIXE spectrum of zirconium mineral. The PIXE conditions as described in the figure. The GUPIXWIN output with data and fit is displayed. Zirconium Kα lines are well visible together with escape peaks. Small amount of Hf can be visible as well (L-lines at 7.9, 9.0 and 10.5 keV). Problematic is overlapping with Zr escape peaks. Possible Ti presence in 4.5 – 4.9 keV region, but more probable is it a Zr escape peak. Presence of U is very plausible. GUPIXWIN found its Lα line at 13.6 keV, but it lies in the "tail" of Zr Kα line. The other uranium L lines lie in the Zr K lines, region; 15.7 – 17.7 keV.

PIGE measurements

Although the beam line is equipped with PIXE/PIGE detector, because of the absence of the radiation shield around the PIXE/PIGE chamber against neutrons, detail PIGE investigations have not been carried out yet, just very preliminary estimations. It is planned the all beam lines after the switching magnet will be shifted to the bunker so reactions with production of neutrons could be carried out as well.

First PIGE spectrum was measured from Teflon tape, which is rich on fluorine (Teflon – PTFE). 3 MeV proton beam was used for this measurement, spectrum displayed in Fig. 79. Protons were non-elastically scattered on the fluorine nuclei what can be seen from spectrum and visible lines at 110, 197, 1236 and 1349 keV. Reactions with protons took place ^{19}F (p, p'γ) [Kiss, 1985]. Possibly other materials with suitable proton reactions will be analyzed.

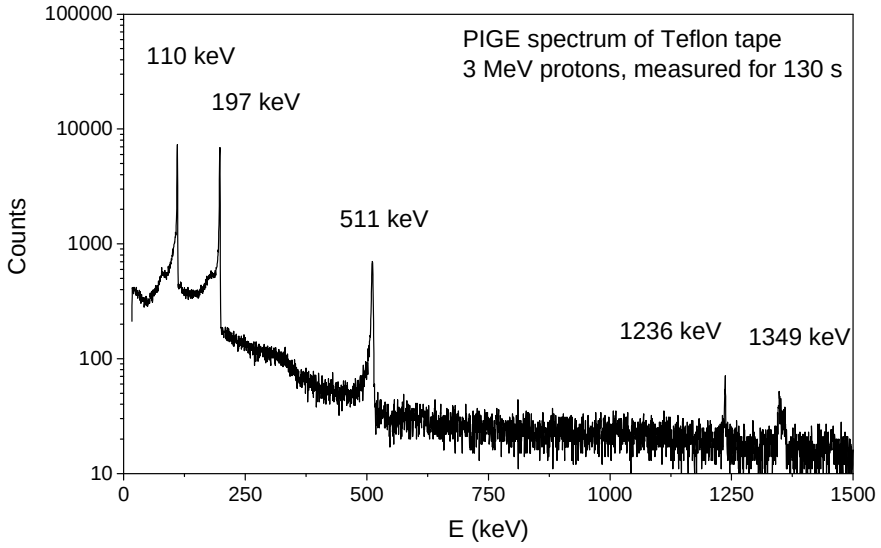

Fig. 81: PIGE spectrum of Teflon (PTFE) tape.

Detected gamma lines with energies 110, 197, 1236 and 1349 keV indicate ^{19}F (p, p'γ) reactions. 511 keV annihilation line was detected as well. PIGE analyzes have not been performed yet, only some spectra were measured in order to test the detector for possible further PIGE analyzes.

Conclusions

The main results achieved in this thesis can be summarized as follows:

Transmission efficiencies for ^{1}H, ^{4}He, ^{9}Be and ^{12}C ions were determined for different values of terminal voltage, and their dependence on the stripper gas pressure was observed. Individual ions exhibit different behavior, depending on the charge state, terminal voltage and nitrogen pressure (the stripping gas). A common feature of all dependencies is a successive increase of the transmission efficiency with increasing stripper gas pressure to a certain point followed by a decrease of the transmission efficiency towards higher stripper gas pressures. This decrease is stronger for lower charge states ($^{4}He^{1+}$, $^{9}Be^{1+}$ and $^{12}C^{2+}$). Towards to higher charge states this decrease is less evident and becomes more flat (charge states $^{4}He^{2+}$, $^{9}Be^{2+}$ and even more for $^{9}Be^{3+}$ and for $^{12}C^{4+}$). The reason for such behavior is that with increasing the stripper gas pressure, both the electron stripping (which affects the transmission efficiency) and the ion scattering on molecules of the stripper gas are rising. Each ion has a combination of charge state, energy (guided by the terminal voltage of the tandem accelerator) and a certain value of stripper gas pressure at which the scattering process starts to reduce the final transmission efficiency. The smooth decrease of transmission efficiency for higher charge can be used for better stability of ion beams at these regions of stripper gas pressure for various applications, e.g. for ion irradiation or for applications of IBA techniques, which require stable ion beams. Working in these stable regions, the transmission efficiency is not affected by slight changes in the stripper gas pressure.

Simulations of $^{4}He^{2+}$ ion beam transversal profile were performed using SIMION software. The beam trajectories through the magnetic quadrupole triplet lens (QP) and the switching magnet (SM) were simulated. The final beam profile was monitored at the target distance (~2 m from the SM exit) in 45° channel. Models of these devices were created using the 3DCAD software Autodesk Inventor. Such models were placed into SIMION's workbench and the ions were flown through the system. The initial beam profile was circular with Gaussian distribution (5×5 mm FWHM), and the beam trajectory was in the axis of the beam line. Magnetic field of SM was simulated so the beam hit the center of target foil. For 3.052 MeV $^{4}He^{2+}$ ion beam the SM's magnetic field flux density was 3914.7

Gauss. Different setting of QP was simulated in order to obtain focused beam at the target distance. Various settings of QP exhibited both focusing as well as defocusing effects on the beam profile. Finally, proper setting of QP was found and focused $^{4}He^{2+}$ ion beam with 1.4 mm diameter was simulated.

The PIXE chamber was installed in September 2015. Firstly, the BEGe detector was calibrated using point radioactive sources covering the energy spectrum of the detector. Three different settings of MCA's amplifier were calibrated; for low energies (up to ~ 60 keV), for medium energies (up to 500 keV) and for high energies (up to 3 MeV). Only results for low energies are stated in this work because the other are not important for purposes of PIXE measurements performed in the laboratory (they will be used for PIGE analyzes). First PIXE analyzes were performed on Slovak coins and laboratory PIXE standards consisting of pressed clean metallic powders (Ti, Fe, Cu, Zn and Ag). Each metallic powder mixture was prepared using a pneumatic press to form flat, coin-like, pellets. These analyzes had mostly qualitative character; we were able to observe a presence of elements in the samples and estimate the possible concentration comparing with the pressed powders standard samples. As we have found out later, the composition of such prepared mixtures is not uniform. We performed multiple PIXE measurements on different spots of each mixed powder sample and observed different relative concentrations of elements present in one sample depending on the measured spot. Therefore, for thick samples, another pressed powders samples were created using only single element powder to form pressed pellets. Nevertheless, the very first PIXE analyzes of Slovak coins taught us how to interpret the measured PIXE spectra and also how important is the knowledge of detector specifications.

For further fully quantitative PIXE analyzes, some adjustments in PIXE chamber had to be done. At first, in Slovak coins analyzed we observed high bremsstrahlung background. Therefore the BEGe detector was shifted into larger distance from the interaction point (center of the PIXE chamber). The new distance from this center increased from original 2.5 cm to 25 cm with impact on the background suppression. This distance was chosen for further analyzes, and is used currently (April 2017), as well. Next, additional electrode was installed into the PIXE chamber. Its purpose is to suppress the secondary emission of electrons after ion impact on the sample surface. This is important

for quantitative PIXE analyzes due to proper charge collection process. SIMION simulations were used to find the proper dimensions of this electrode. The final shape and dimensions had to be suitable into the inside of the chamber and satisfy the SIMION simulations as well.

Quantitative PIXE analyzes require knowledge of the precise detector efficiency in order to retrieve information about absolute concentrations of element constituting monitored samples. For this purpose, BEGe detector efficiency was both measured and modelled. The measurements were performed using point sources of known activities placed in 25 cm distance from the detector endcap on the detector axis. The efficiency of BEGe detector was modelled using DETMC program. Detector characteristics (from manufacturer's datasheet) were used. Distance of point source was chosen the same (25 cm) and energy range from 2 – 60 keV was monitored. in Fig.The modelled efficiency below 5 keV drops below a reasonable value. Therefore, quantitative analyzes of X–rays below 5 keV is complicated. This means that direct quantitative PIXE analysis can be performed starting with vanadium for K lines (4.952 keV) and praseodymium for L lines (5.033 keV). However, employing special strategies in sample treatment and spectra evaluation can reach lower X–ray energies, and even the detector efficiency can be "bypassed" using well-defined standard samples.

For direct quantitative analyzes a knowledge of H value is crucial together with detector efficiency. Depending on the detection system characterization, the energy dependency of H value can be observed. In well-defined system, the H value should be constant, independent on the X–ray energy. Any missing parameter or misinterpreted parameter can lead to dependency on the energy. In CENTA laboratory, H values for thin and thick targets were determined separately. Individual values were determined using pure elemental standards. For thin samples (ion beam can penetrate through the sample) this values were determined from analyzes of thin film standards (MICROMATTER™). Both, proton and helium beams were monitored and final H values for individual X–ray energies were determined using GUPIXWIN software. For thin samples, H value for protons exhibits energy dependency, but H value for helium beam is more-less constant. For thick samples, only H values for protons were determined because of technical issues (difficulties with Alphatross ion source). These H values exhibits energy dependency similar to thin

samples measurements. Determined H values can be used for further PIXE analysis of different materials. Depending on the structure of monitored samples (whether it is thick or thin), these H values can be used in GUPIXWIN calculations of element concentration.

A special sample of rat brain slice was analyzed using the PIXE technique. This sample forms a special layered system of material which could have been analyzed by GUPIXWIN. The 3 MeV proton beam with 1.5 mm diameter was utilized for this analysis. The rat brain slice mounted on a silicon wafer and covered by thin gold film was placed into the PIXE chamber, and thin proton beam PIXE analyzes were performed on 12 different spots across the sample surface. The goal was to determine the iron concentration in this sample. For this purpose, special samples were prepared in the laboratory. Iron solutions of known concentrations were dropped on several silicon wafers to form individual samples. After drying these samples were installed into PIXE chamber and analyzed under the same conditions as the rat brain sample. GUPIXWIN was used for all analyzes. Comparing Fe Kα areas in laboratory samples' spectra with Kα areas from multiple measurements of rat brain sample spots, the final concentrations of iron in rat brain slice were determined on monitored positions with values up to 50 ppm, showing a clear gradient of .concentrations.

Achieved results concerning development and utilization of IBA techniques show the range of taken effort to obtain reliable conclusions. Only 4 years before the laboratory hall was built (February 2013), then it was equipped with tandem accelerator and other units, so first calibration and optimization measurements could be carried out. Ion sources settings were adjusted to optimize yields for individual types of ions. Pelletron transmission efficiency was determined for different ion beams and various stripping gas pressures. Ion beam irradiation effects were monitored firstly in one channel on a target foils. Later, in September 2015, a new PIXE/PIGE beam line was installed and PIXE analyzes began. Several adjustments were done in the PIXE chamber to maximize the utilization of PIXE technique. The fact, that an iron concentration in a biological sample was determined reveals potential use of this technique, and next steps are directed to nuclear microprobe utilization.

Future of IBA techniques in the CENTA laboratory is aimed at PIXE analyzes performed on atmosphere using glass capillaries to extract the beam from vacuum have a strong potential. Research of precious and biological samples can be developed in novel dimensions. The crucial basis of PIXE analyzes have been handled successfully and current effort is aimed to this objective - raster scans of samples. Several laboratories have already settled up this research worldwide, but the range of this area is so wide and unexplored, that investigation of samples can bring interesting and important results. Precious samples such as paintings, sculptures, meteorites and various biological materials (which cannot be exposed to vacuum) can be analyzed within few minutes. Depending on the range of desired information about specimen, various dependencies can be investigated including depth profiles, surface distribution of elements, etc. which can lead to better understanding of investigated sample origins or possible contamination from outer sources (e.g. piece of art manipulation or falsification).

References

[Alph, 2011] National Electrostatics Corp., Instruction manual No. 2JT002110 for RF Charge Exchange Ion Source. Middleton, 2011.

[Bend, 2011] National Electrostatics Corp., Instruction manual No. 2BA020240 for Analyzing magnet injection beamline. Middleton, 2011.

[Borysiuk, 2014] Borysiuk M. et al., Evaluation of a setup for pNRA at LIBAF for applications in geosciences, Nuclear Instruments and Methods in Physics Research B, vol. 332, p. 202–206, Elsevier, 2014.

[BPM, 2011] National Electrostatics Corp., Instruction Manual No. 2ET908110 for Operation and Service of Beam profile monitor model BPM81 (Integral collector). Middleton, 2011.

[Bykov, 2012] Bykov I. et al., Investigation of tritium analysis methods for ion microbeam application, Nuclear Instruments and Methods in Physics Research B, vol. 273, p. 251. Elsevier, 2012.

[Calligaro, 2001] Calligaro T. et al., ERDA with an external helium ion micro beam: Advantages and potential applications, Nuclear Instruments and Methods in Physics Research B, vol. 181, p. 180, Elsevier, 2001.

[Campbell, 2000] Campbell J.L., Hopman T.L., Maxwell J.A., Nejedly Z., The Guelph PIXE software package III: Alternative proton database, Nuclear Instruments and Methods in Physics Research B, vol. 170, p. 193 – 204. Elsevier, 2000.

[Campbell, 2010] Campbell J.L., Boyd N.I., Grassi N., Bonnick P., Maxwell J.A., The Guelph PIXE software package IV, Nuclear Instruments and Methods in Physics Research B, vol. 268, p. 3356–3363. Elsevier, 2010.

[Carella, 2014] Nuclear reaction analysis as a tool for the ^{3}He thermal evolution in Li_2TiO_3 ceramics, Nuclear Instruments and Methods in Physics Research B, vol. 332, p. 85–89, Elsevier, 2014.

[Calzolai, 2015] Calzolai G. et al., Improvements in PIXE analysis of hourly particulate matter samples, Nuclear Instruments and Methods in Physics Research B, vol. 363, p. 99–104, Elsevier, 2015.

[Chêne, 2012] Chêne G. et al., New external beam and particle detection set-up of Liège cyclotron – First applications of high energy beams to cultural heritage, Nuclear Instruments and Methods in Physics Research B, vol. 273, p. 209. Elsevier, 2012.

[Chu, 1978] Chu W.-K., Mayer J. W., Nicolet M.-A., Backscattering spectrometry, Academic Press, Inc., San Diego, 1978.

[Dapor, 2016] Dapor M., Abril I., de Vera P., Garcia-Molina R., Energy Deposited by Secondary Electrons Generated by Swift Proton Beams through Polymethylmethacrylate, International Journal of Chemical, Molecular, Nuclear, Materials and Metallurgical Engineering, vol. 10 (8), p. 992. World Academy of Science, Engineering and Technology, 2016.

[Denker, 2005] Denker A. et al., High-energy PIXE using very energetic protons: quantitative analysis and cross-sections, X-Ray Spectrom., vol. 34, p. 376–380, Wiley, 2005.

[EL1, 2017] online: http://en.wikipedia.org/wiki/Einzel_lens

[EL2, 2011] National Electrostatics Corp., Instruction Manual No. 2ET067180 for Operation and Service of EINZEL LENS Model EL76-60. Middleton, 2011.

[ERDA, 2016] online: http://www.spirit-ion.eu/v1/Project/Techniques/ERDA.html

[ESA, 2011] National Electrostatics Corp., Instruction manual No. 2EA071000 for ESA, INJECTOR. Middleton, 2011.

[ESXY, 2011] National Electrostatics Corp., Instruction Manual No. 2ET903100 for Operation of Electrostatic steerers. Middleton, 2011.

[FC50, 2011] National Electrostatics Corp., Instruction manual No. 2ET952300 for Faraday cup model no. FC50. Middleton, 2011.

[Guillou, 2014] Thermal behavior of deuterium implanted into nuclear graphite studied by NRA, Nuclear Instruments and Methods in Physics Research B, vol. 332, p. 90–94, Elsevier, 2014.

[Kaplan, 2016] Kaplan S. et al., Electromagnetic field and brain development, Journal of Chemical Neuroanatomy, vol. 75, p. 52–61. Elsevier, 2016.

[Karydas, 2014] Karydas A. G. et al., In-depth elemental characterization of $Cu(In,Ga)Se_2$ thin film solar cells by means of RBS and PIXE techniques, Nuclear Instruments and Methods in Physics Research B, vol. 331, p. 93–95, Elsevier, 2014.

[Kiss, 1985] Kiss Á. Z. et al., Measurements of relative thick target yields for PIGE analysis on light element in the proton energy interval 2.4 – 4.2 MeV, J Radioanal Nucl Chem, vol. 89, p. 123-141. Springer, 1985.

[Kostoff, 2013] Kostoff R.N., Lau G.Y.C., Combined biological and health effects of electromagnetic fields and other agents in the published literature, Technological Forecasting & Social Change, vol. 80, p. 1331–1349. Elsevier, 2013.

[NPL, 2017] available online at National Physical laboratory webpage: http://www.kayelaby.npl.co.uk/atomic_and_nuclear_physics/4_2/4_2_1.html

[Magalhães, 2012] Magalhães S. et al., High precision determination of the InN content of $Al_{1-\chi}$ $In_\chi N$ thin films by Rutherford backscattering spectrometry, Nuclear Instruments and Methods in Physics Research B, vol. 273, p. 105. Elsevier, 2012.

[Manuel, 2014] Manuel J.E. et al., Fish gelatin thin film standards for biological application of PIXE, Nuclear Instruments and Methods in Physics Research B, vol. 332, p. 37–41, Elsevier, 2014.

[Martin, 2012] Martin G. et al., Irradiation damage effects on helium migration in sintered uranium dioxide, Nuclear Instruments and Methods in Physics Research B, vol. 273, p. 123. Elsevier, 2012.

[Martin, 2003] Martin J. W. et al., The Local Chemical Analysis of Materials, Pergamon Materials Series, vol. 9, p. 112. Elsevier, 2003.

[Mathayan, 2016] Mathayan V., Balakrishnan S., Panigrahi B., Lattice location of O^{18} in ion implanted Fe crystals by Rutherford backscattering spectrometry, channeling and nuclear reaction analysis, Nuclear Instruments and Methods in Physics Research B, vol. 383, p. 47–51, Elsevier, 2016.

[Maxeiner, 2015] Maxeiner S. et al., Simulation of ion beam scattering in a gas stripper, Nuclear Instruments and Methods in Physics Research B, vol. 361, p. 242, Elsevier, 2015.

[Maxwell, 1989] Maxwell J.A., Campbell J.L., Teesdale W.J., The Guelph PIXE software package, Nuclear Instruments and Methods in Physics Research B, vol. 42, p. 218 – 230. Elsevier, 1989.

[Maxwell, 1995] Maxwell J.A., Teesdale W.J., Campbell J.L., The Guelph PIXE software package II, Nuclear Instruments and Methods in Physics Research B, vol. 95, p. 407 – 421. Elsevier, 1995.

[Mayer, 2012] Mayer M. et al., Rutherford backscattering analysis of porous thin TiO2 films, Nuclear Instruments and Methods in Physics Research B, vol. 273, p. 83. Elsevier, 2012.

[MicroM, 2017] webpage of the company: http://www.micromatter.com/xrf.php

[Morilla, 2012] Morilla Y. et al., Developing the IBA equipment to increase the versatility of the CNA, Nuclear Instruments and Methods in Physics Research B, vol. 273, p. 221. Elsevier, 2012.

[Msimanga, 2012] Msimanga M. et al., Heavy ion energy loss straggling data from Time of Flight stopping force measurements, Nuclear Instruments and Methods in Physics Research B, vol. 273, p. 6. Elsevier, 2012.

[MS-Y, 2011] MS-Y] National Electrostatics Corp., Instruction manual No. 2EA032940 for Magnetic Steerer. Middleton, 2011.

[Nakai, 2015] Nakai K. et al., Boron analysis for neutron capture therapy using particle-induced gamma-ray emission, Applied Radiation and Isotopes, vol. 106, p. 166–170, Elsevier, 2015.

[Nastasi, 2015] Nastasi M., Mayer J.W., Wang Y., Ion beam analysis: fundamentals and applications. CRC Press, Boca Raton, 2015.

[NRA, 2016] online: http://www.spirit-ion.eu/v1/Project/Techniques/NRA.html

[Ortega, 2010] Ortega-Feliu I. et al., A comparative study of PIXE and XRF corrected by Gamma-Ray Transmission for the non-destructive characterization of a gilded roman railing, Nuclear Instruments and Methods in Physics Research B, vol. 268, p. 1920–1923, Elsevier, 2010.

[Paneta, 2014] Paneta V. et al., Study of the ^{24}Mg (d, $p_{0, 1, 2}$) reactions at energies and angles relevant to NRA, Nuclear Instruments and Methods in Physics Research B, vol. 319, p. 34–38, Elsevier, 2014.

[Patronis, 2014] Patronis N. et al., Study of ^{nat}Mg(d,d_0) reaction at detector angles between 90° and 170°, for the energy range $E_{d,lab}$=1660–1990 keV, Nuclear Instruments and Methods in Physics Research B, vol. 337, p. 97–101, Elsevier, 2014.

[Pellegrino, 2012] Pellegrino S. et al., The JANNUS Saclay facility: A new platform for materials irradiation, implantation and ion beam analysis, Nuclear Instruments and Methods in Physics Research B, vol. 273, p. 216. Elsevier, 2012.

[Pelletron1, 2017] online: http://www.pelletron.com/tutor.htm

[Pelletron2, 2017] online: http://www.pelletron.com/negion.htm

[Pelletron3, 2017] online: http://www.pelletron.com/charging.htm

[Petersson, 2012] Petersson P. et al., Nuclear reaction and heavy ion ERD analysis of wall materials from controlled fusion devices: Deuterium and nitrogen-15 studies, Nuclear Instruments and Methods in Physics Research B, vol. 273, p. 113. Elsevier, 2012.

[Pichon, 2010] Pichon L., Beck L., Walter Ph., Moignard B., Guillou T., A new mapping acquisition and processing system for simultaneous PIXE-RBS analysis with external beam, Nuclear Instruments and Methods in Physics Research B, vol. 268, p. 2028–2033, Elsevier, 2010.

[Povinec, 2015] Povinec P. et al., A new IBA-AMS laboratory at the Comenius University in Bratislava (Slovakia), Nuclear Instruments and Methods in Physics Research B, vol. 342, p. 324. Elsevier, 2015.

[Povinec, 2015B] Povinec P. et al., Development of the Accelerator Mass Spectrometry technology at the Comenius University in Bratislava, Nuclear Instruments and Methods in Physics Research B, vol. 361, p. 88. Elsevier, 2015.

[Povinec, 2016] Povinec P.P., Masarik J., Ješkovský M., Breier R., Kaizer J., Pánik J., Richtáriková M., Staníček J., Šivo A., Zeman J., Recent results from the AMS/IBA laboratory at the Comenius University in Bratislava: preparation of targets and optimization of ion sources, J Radioanal Nucl Chem, vol 307, p. 2101–2108. Springer, 2016.

[Reiche, 2006] Reiche I. et al., Analyses of hydrogen in quartz and in sapphire using depth profiling by ERDA at atmospheric pressure: Comparison with resonant NRA and SIMS, Nuclear Instruments and Methods in Physics Research B, vol. 249, p. 609. Elsevier, 2006.

[Sério, 2012] Sério S. et al., Incorporation of N in TiO2 films grown by DC-reactive magnetron sputtering, Nuclear Instruments and Methods in Physics Research B, vol. 273, p. 110. Elsevier, 2012.

[SIMION, 2017] SIMION 8.0 user manual, chapter 2 – SIMION Basics, available online: http://simion.com/manual/chap2.html

[Steier, 2000] Steier P., Exploring the limits of VERA: A universal facility for accelerator mass spectrometry, dissertation, p. 57-64, Institut für Isotopenforchung und Kernphysik, VERA Labor, Vienna, 2000.

[Suárez, 2011] Moreno-Suárez A. I. et al., Combining non-destructive nuclear techniques to study Roman leaded copper coins from Ilipa (II–I centuries B.C.), Nuclear Instruments and Methods in Physics Research B, vol. 269, p. 3098–3101, Elsevier, 2011.

[Switch, 2011] National Electrostatics Corp., Instruction manual No. 2BA017470 for Switching magnet. Middleton, 2011.

[Terzi, 2016] Terzi M., Ozberk B., Deniz O.G., Kaplan S., The role of electromagnetic fields in neurological disorders, Journal of Chemical Neuroanatomy, vol. 75, p. 77–84. Elsevier, 2016.

[Tripathy, 2010] Tripathy B.B., Rautray T. R., Rautray A. C., Vijayan V., Elemental analysis of silver coins by PIXE technique, Applied Radiation and Isotopes, vol. 68, p. 454–458, Elsevier, 2010.

[Wiedemann, 2015] Wiedemann H., Particle accelerator physics, 4th edition, Graduate text in physics, p. 12, Springer, 2015.

[Winkler, 2015] Winkler S. R. et al., He stripping for AMS of 236U and other actinides using a 3 MV tandem accelerator, Nuclear Instruments and Methods in Physics Research B, vol. 361, p. 461, Elsevier, 2015.

[Založnik, 2016] Založnik A. et al., In situ hydrogen isotope detection by ion beam methods ERDA and NRA, Nuclear Instruments and Methods in Physics Research B, vol. 371, p. 167–173, Elsevier, 2016.

[Zeman, 2016] Zeman J., Ješkovský M., Pánik J., Staníček J., Povinec P.P., Pelletron transmission efficiency measurements for ^{9}Be and ^{12}C ions at the CENTA laboratory, Acta Physica Universitatis Comenianae, vol. 53, p. 95–100, Bratislava, 2016.

[Zeman, 2016B] Zeman J., Ješkovský M., Kaiser R., Kaizer J., Povinec P.P., Staníček J., PIXE beam line at the CENTA facility of the Comenius University in Bratislava: first results, J Radioanal Nucl Chem, vol. 309, DOI 10.1007/s10967-016-5004-1. Springer, 2016.

[Zucchiatti, 2015] Zucchiatti A. et al., Building a fingerprint database for modern art materials: PIXE analysis of commercial painting and drawing media, Nuclear Instruments and Methods in Physics Research B, vol. 363, p. 150–155, Elsevier, 2015.

List of publications

Appendix A:

Zeman J., Ješkovský M., Kaiser R., Kaizer J., Povinec P.P., Staníček J., PIXE beam line at the CENTA facility of the Comenius University in Bratislava: first results, J Radioanal Nucl Chem, vol. 309, DOI 10.1007/s10967-016-5004-1. Springer, 2016.

Appendix B:

Zeman J., Ješkovský M., Pánik J., Staníček J., Povinec P.P., Pelletron transmission efficiency measurements for ^{9}Be and ^{12}C ions at the CENTA laboratory, Acta Physica Universitatis Comenianae, vol. 53, p. 95–100, Bratislava, 2016.

Appendix C:

Povinec P.P., Masarik J., Ješkovský M., Kaizer J., Šivo A., Breier R., Pánik J., Staníček J., Richtáriková M., Zahoran M., **Zeman J.**, Development of the Accelerator Mass Spectrometry technology at the Comenius University in Bratislava, Nuclear Instruments and Methods in Physics Research B, vol. 361, p. 87–94. Elsevier, 2015.

Appendix D:

Povinec P.P., Masarik J., Ješkovský M., Breier R., Kaizer J., Pánik J., Richtáriková M., Staníček J., Šivo A., **Zeman J.**, Recent results from the AMS/IBA laboratory at the Comenius University in Bratislava: preparation of targets and optimization of ion sources, J Radioanal Nucl Chem, vol 307, p. 2101–2108. Springer, 2016.

Appendix A

PIXE beam line at the CENTA facility of the Comenius University in Bratislava: first results

J Radioanal Nucl Chem
DOI 10.1007/s10967-016-5004-1

PIXE beam line at the CENTA facility of the Comenius University in Bratislava: first results

Jakub Zeman[1] · Miroslav Ješkovský[1] · Ralf Kaiser[2] · Jakub Kaizer[1] · Pavel P. Povinec[1] · Jaroslav Staníček[1]

Received: 15 June 2016

Abstract Optimization of the proton and helium beams from the alphatross ion source through the injection beamline, the 3 MV Pelletron tandem accelerator, the high-energy analyzer and the PIXE chamber were carried out. Results obtained with the ^{4}He ion beam showed better detection limits when compared with protons of the same energy and beam intensity. For detection of produced X-rays, a BEGe detector has been used, covering the energy range from 3 keV to 3 MeV. First measurements with ^{4}He ions of 3.5 MeV energy included calibration runs with PIXE laboratory standards, as well as analyses of old silver coins.

Keywords PIXE · X-ray spectra · Elemental analysis · PIXE standards · Silver coins

Introduction

Particle-induced X-ray emission (PIXE) is one of the leading analytical technique for determination of the element occurrence in variety of samples. One of the major PIXE advantages is that this technique is non-destructive. Therefore, it is possible to carry out analysis of samples, which have high cultural, historical or social value, and destructive analysis of such samples could not be considered. Such samples include paintings, statues, archeological artifacts, etc. For materials of this importance non-destructive method for analysis is crucial, and the PIXE is one of them used worldwide for this purpose.

PIXE technique is based on ejection of inner-shell electrons from target atoms by the energetic incident particle impact, and subsequent registration of emitted X-rays during their de-excitations. Evolution of the PIXE has a long history, but as an analytical tool with wide applications can be dated back to 1976, when a review article dealing with X-ray emission induced by charged particles and the use of this process as an analytical technique has been published [1]. Principles of the PIXE technique have been discussed by several authors and the most recent summary can be found in [2]. The main advantage of the PIXE method, e.g. for analysis of material and environmental samples, is in its higher sensitivity when compared with other X-ray analysis techniques. For calculation of the limit of detection for the PIXE method usually an X-ray peak is declared to be detectable if it exceeds three standard deviations of the underlying background. Therefore in X-ray spectrometry the treatment of peak background is essential. The background contributions are from different sources such as bremsstrahlung, low energy gamma-rays from nuclear reactions, overlapping X-rays, etc. Another issue in the treatment of X-ray spectra is an occurrence of artificial peaks, which should be well classified and their origin should be known [3]. The analysis of real X-ray spectra affected by a background and presence of artificial peaks influence the final evaluations of results with impact on the calculation of element concentration in specimen.

Energy dispersive X-ray spectroscopy (denoted as EDS or EDX) compared to PIXE technique suffers higher background since in the EDS electrons are inducing

✉ Pavel P. Povinec
pavel.povinec@uniba.sk

[1] Department of Nuclear Physics and Biophysics, Faculty of Mathematics, Physics and Informatics, Centre for Nuclear and Accelerator Technologies (CENTA), Comenius University, 84248 Bratislava, Slovakia

[2] Department of Nuclear Sciences and Applications, International Atomic Energy Agency, Vienna, Austria

Published online: 29 August 2016

production of X-rays, while in the PIXE method only protons or heavier particles are used for X-ray production. Background in the PIXE measurements is approximately by two orders of magnitude lower than in the EDS measurements [4]. This background suppression depends on a particular sample material and can vary within certain limits, but generally, this means that PIXE is one hundred times more sensitive than EDX.

Another method similar to PIXE is an X-ray fluorescence spectroscopy (XRF). Both methods can reach the region of sensitivity down to ppm levels. The XRF method can be preferred for large samples as it is cheaper and easier to operate, but for small samples or microprobe applications, the PIXE is more advantageous technique. The difference is due to the fact that PIXE is a near surface technique due to small penetration of incident particles (protons, alphas and heavier nuclei), and a smaller absorption of characteristic X-rays. Although the incident X-rays which are used in XRF analyses have a greater range in the material than particles used in PIXE, both the characteristic and the inducing X-rays are attenuated in the XRF method [5]. The PIXE compared to XRF has another advantage in analysis of bulk samples, where in the PIXE method the thickness reachable by particles is relatively constant, while for XRF there is usually a wide variation.

Another important parameter for PIXE applications depends on particles, which are being used for X-ray production in sample material. Protons are mainly used, but other, heavier particles show different features, and depending on a specimen, different detection limits can be reached. In principle, heavier ions produce less gamma-background through nuclear reactions within the analyzed material. Thus obtained detection limits are better with alphas than with protons. The energy of incident beam has to be within reasonable limits. On one hand, the lower the energy of incident ions is, the lower background in spectrum is achieved. But, with decreasing energy of particles the ionization cross-section for X-ray production decreases, and for sufficient statistics the measurement have to be very long so the specimen heating could become an issue. On the other hand, with increasing beam energy ionization cross section rises so the production of X-rays is higher, and thus the measurements can be swift. But, the higher the energy of incident particles, the higher the gamma-background from nuclear reactions, and thus the detection limit is worse. For this reasons, energy of protons from 1.8 to 3 MeV, and energies around 5 MeV for alphas are recommended. Explanatory examples for detection limits using different ions of various energies can be found in [6]. Under these conditions, detection limits below 0.1 ppm are reachable with PIXE technique using 5 MeV alphas.

Very interesting upgrade in the PIXE technique represents a micro-PIXE [7–9]. This modification of the standard PIXE method involves very small and well-defined beam spots, which are used for sample analysis. Depending on a specific micro-PIXE design, spots of several micrometers to tens of micrometers can be created, and via a precise beam movement over the sample, raster images can be produced. There are two common ways how this small beam spots are achieved. Firstly, micro-capillaries are used for beam collimation, secondly, the beam is focused to small spots using electromagnetic lenses. Using a special sample positioning system, it is possible to make raster scans over specimen, and thus obtain element concentration maps.

There are large varieties of samples that can be investigated by the PIXE technique, one group of samples that are being analyzed worldwide are coins [10–12]. PIXE non-destructive analyses of historical coins are usually conducted, when an elemental composition of samples with high precision can be obtained. The next group of samples that are being widely investigated are aerosols. The chemical composition of aerosols collected at lower layers of the atmosphere is helpful for studying various effects on human health and the environment. Aerosols are usually collected by impactors, and depending on specific measurement conditions, different sampling times are used. They are being deposited on different materials, mostly foils (Kapton, Teflon, Nuclepore) or nitrocellulose filters. Investigation of aerosol pollution, e.g. due to emissions from industry, vehicles, ships, as well as analysis of clean air samples from mountains has been carried out by several laboratories [13–17]. Biological materials are also frequently analyzed samples using the PIXE technique, focusing usually on the presence of heavy metals in human or animal tissues [18–21].

The aim of the present work has been to optimize the proton and helium beams from the alphatross ion source through the injection beam-line, the 3 MV Pelletron tandem accelerator, the high-energy analyzer and finally at the PIXE chamber. First measurements with ^{4}He ions of 3.5 MeV energy included calibration runs with PIXE laboratory standards, as well as analyses of old silver coins.

Methods

A Centre for Nuclear and Accelerator technologies (CENTA) has been established recently at the Comenius University in Bratislava (Slovakia) comprising of a state-of-the art tandem accelerator laboratory designed for ion beam analysis (PIXE and PIGE), nuclear reaction analysis, ion beam modification and accelerator mass spectrometry studies [22]. The laboratory is consisting of three main parts: ion sources for gas and solid targets, injection system of ions, Pelletron tandem accelerator, and analyzer of

accelerated ions. The equipment has been supplied by National Electrostatic Corp. (USA). Proton and helium ion beams are produced in an alphatross ion source (Fig. 1). Alphatross is a radio frequency (RF) ion source, which produces positive ions. A gas or gas mixture is bled into a quartz bottle; an RF oscillator connected to the quartz bottle dissociates the neutral gas. A voltage difference (usually about 2–6 kV) is used to push the ions out of the chamber through the exit aperture, making a continuous beam. To produce a negative ion beam for the tandem accelerator, the positive beam in the alphatross is injected into a rubidium charge exchange cell [23].

The ions after passing the injection system consisting of an electrostatic deflector and an injection magnet are injected into 3 MV linear tandem accelerator 9SDH-2 Pelletron, which is used for acceleration of selected ions to desired energy. The maximal possible energy for proton beam is 6 MeV, for ^{4}He (2^{+} charge state) ion beam this energy is 9 MeV. The accelerated ions are then focused in a quadrupole down to the diameter of 1 mm, and passing through the switching magnet they are introduced into the PIXE chamber (Fig. 2). A magnetic steerer in front of the PIXE chamber is used for beam shifts. The measurements were performed with sample holder at the 45° angle to the beam line. Characteristic X-rays were detected at the 45° angle by the broad energy germanium (BEGe) detector (the endcap with carbon window is visible on the left side of the image in Fig. 3).

The chamber is equipped with a sample holder capable of mounting four thick samples of about 2×2 cm dimension. The holder can be rotated around its vertical axis, so the angle how the incident beam should hit the sample can be fixed (Fig. 3). For the charge collection, digital current integrator (Ortec Model 439) is used. BEGe detector with carbon window (0.6 mm thickness) from CANBERRA is used for detection of emitted X-rays. The BEGe detector covers the energy range from 3 keV to 3 MeV, with energy resolution of 390 eV for 5.9 keV (^{55}Fe) and 1.8 keV for 1332 keV (^{60}Co).

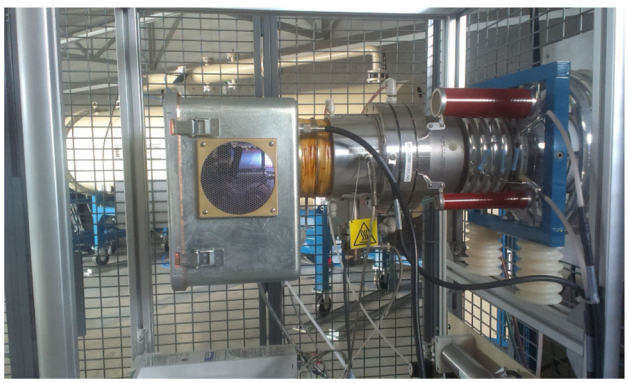

Fig. 1 Alphatross ion source with helium plasma inside

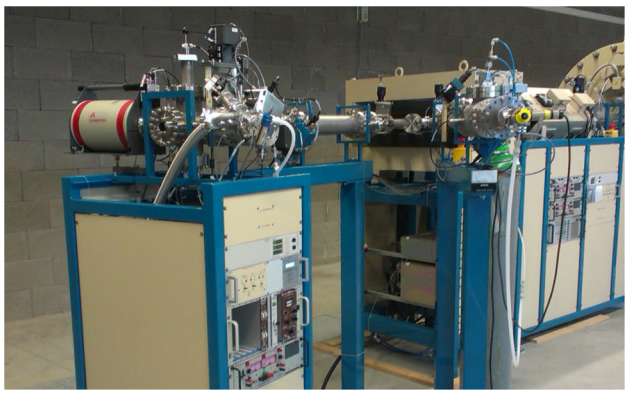

Fig. 2 PIXE beam line (*left*) at the CENTA laboratory

Laboratory PIXE standards consisting of pressed clean metallic powders (supplied by Alfa Aesar®) were used throughout the measurements. The samples were prepared by mixing Ti, Fe, Cu, Zn and Ag powders in various proportions. The purity of the powders was as follows: Ti (99.99 %), Fe (>99 %), Cu (99.9 %), Zn (99.9 %) and Ag (99.9 %). Each metallic powder mixture was prepared using a pneumatic press to form flat, coin-like, pellets. A relative elemental concentration of each sample was calculated as a ratio of the element powder mass to the total mass of the mixture. The relative concentrations of elements are presented in Table 1.

Samples were mounted on the sample holder and placed into the PIXE chamber (Fig. 3). Each sample was measured both with proton and helium beams, the energy of incident ions was 3 and 4.5 MeV, respectively. Since high levels of bremsstrahlung were measured by the BEGe detector, the intensity of the beam had to be pulled down below 1 nA, so peaks with sufficient resolution (400–500 eV for 6.4 keV K_{α} peak from iron) could be observed. The time for spectra acquisition was varying from 5 to 12 min. Digital pulse processor DP5 OEM supplied by Amptek® was used for data acquisition. Measured PIXE spectra were processed by software package GUPIXWIN [24].

Results and discussion

Measured PIXE spectra and fits of characteristic X-ray lines are displayed in Fig. 4. Proton and helium beam measurements for each sample are showing similar peak-area ratios. The main difference is in the bremsstrahlung background. The proton-induced X-ray spectra indicate higher levels of background compared to the helium

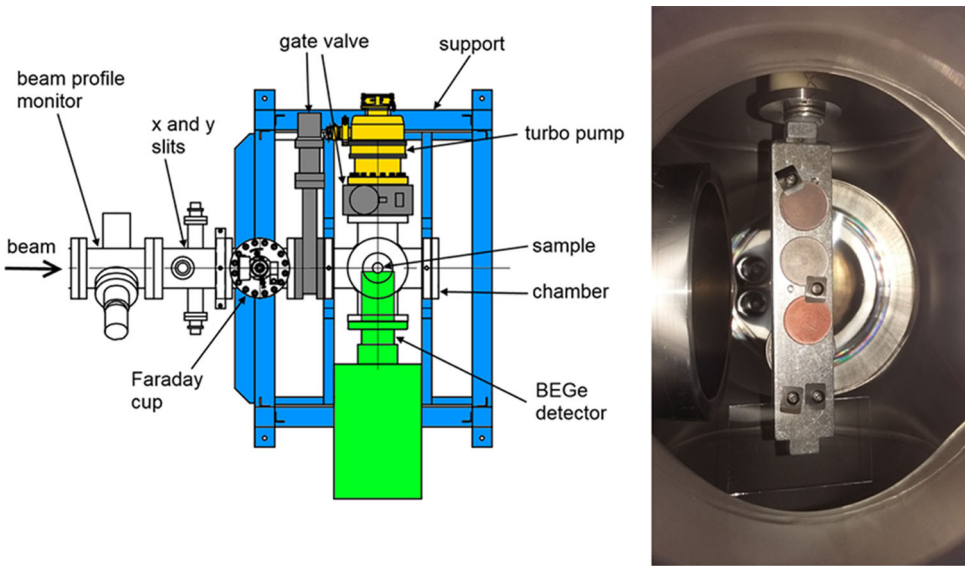

Fig. 3 Scheme of the PIXE/PIGE chamber with sample holder (*left*), and mounted pressed metallic powder samples (*right*)

Table 1 Composition of laboratory PIXE standards

Standard	Element	Mass (mg)	Ratio (%)
PIXE2	Fe	1367.36	62.19
	Cu	831.43	37.81
PIXE3	Ti	287.64	18.65
	Fe	694.57	45.03
	Cu	282.03	18.29
	Ag	278.10	18.03
PIXE4	Fe	326.06	19.56
	Cu	1107.75	66.45
	Zn	233.34	14.00

measurements. This phenomenon is more obvious because of the significant difference in charge collection within proton and helium beams. Measurements with proton beam were performed using approximately ten times lower integrated beam charge compared to measurements with the helium beam (Table 2).

Due to different elemental composition of laboratory standards various effects were observed in the measured spectra. For PIXE2 sample, which consisted only of iron and copper (Table 1), the K_α and K_β peaks were sufficiently resolved (Fig. 4). This resolution was approximately the same for proton and helium beam measurements. The PIXE3 sample measurement showed a slight difference in the measured X-ray spectra. The titanium K_α and K_β peaks were better resolved in the helium than proton beam measurements. The same region (from 4.5 to 5 keV approximately) in proton-induced spectra exhibits a worse resolution of these peaks. Possible explanation could be in a higher bremsstrahlung background, or that the sample contained some impurities such as chromium or manganese (or both), and corresponding characteristic X-ray lines (5.4 keV from Mn and 5.9 keV from Cr) are contributing to this energy region. Both, proton and helium-induced spectra had a tail to the lower energies from 6.4 keV K_α line of iron. Because of high iron concentration in the PIXE3 sample (Table 1), possible low concentration of Mn or Cr is questionable. Similar situation is presented in PIXE4 measurement. This sample contained iron, copper and zinc (Table 1). Compared to the PIXE2 sample, the concentration of copper in the mixture was higher. This resulted in a worse resolution of K_α and K_β peaks from iron in both spectra. In addition, a separation of zinc characteristic X-rays (8.6 and 9.6 keV) was not possible. The zinc K_α line was between the copper K_α and K_β lines (8.1 and 8.9 keV). This decreased the resolution of the copper K_α and K_β lines compared to the PIXE2 sample.

Integrated beam charge was measured by digital current integrator. Since there was no suppression of secondary electron emission, the charge collection by current integrator was ambiguous. Measurement conditions concerning the duration of each sample with corresponding measured integrated beam charge are shown in Table 2. Because of high bremsstrahlung radiation background the intensity of beam had to be decreased to pA level. The estimated uncertainty of charge integration was about 30 %. For the absolute element concentration calculations a knowledge of this value is crucial [25–29].

The detector efficiency was determined using calibrated gamma-ray sources with energies from 15 keV to 1.5 MeV. Due to large uncertainties in the integrated beam charge

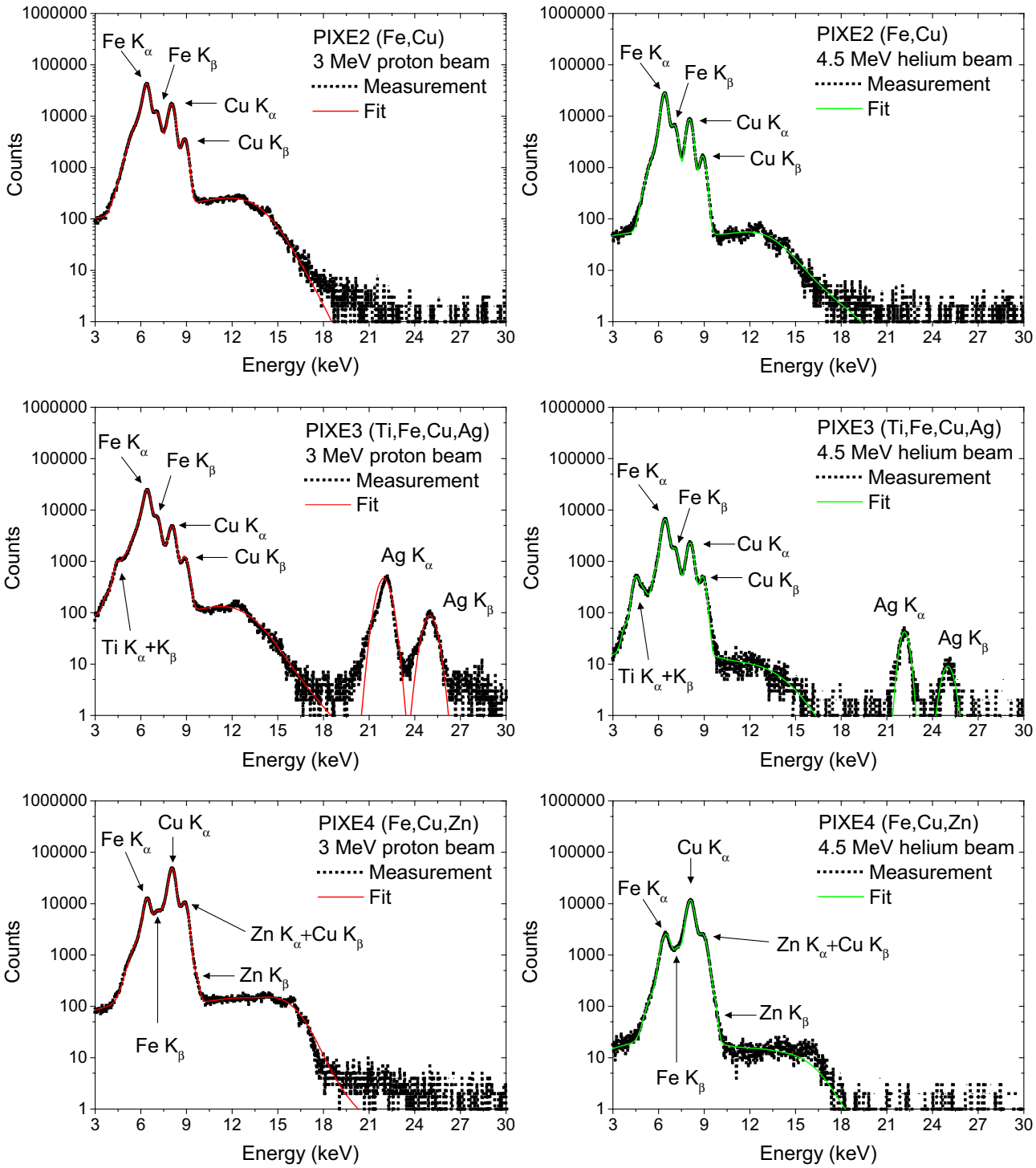

Fig. 4 Measured and fitted X-ray spectra of laboratory standards PIXE2, PIXE3 and PIXE4 (each sample was measured using proton and helium beams)

measurements and in the determination detection efficiency below 15 keV, the precision of data presented in Table 2 is still not satisfactory, and it should be improved in the near future. Using the present set of parameters, the elemental composition of standards listed in Table 1 could be reproduced with relative standard deviations of about 10 %.

PIXE measurements of two Slovak coins using 4.5 MeV helium beam were performed (Fig. 5a). A silver Slovak coin of nominal value 20 crowns which was issued in 1941 during the Slovak state, and a Slovak coin of nominal value 1 crown which was used as a former currency (from 1993 to 2004) in the Slovak Republic were analyzed. GUPIX-WIN was used for the composition determination of these coins. The 1941 Slovak silver coin was measured using 50 pA beam intensity for 10 min. The measurement showed presence of silver and copper characteristic X-ray lines. Since the concentration of silver in this coin was higher than 50 %, two escape peaks were observed in the spectra. The copper K_α and K_β lines were sufficiently resolved. There was an indication of iron occurrence. At 6.4 keV, which corresponds to the iron K_α line, possible peak appeared, but the presence of iron in the spectrum is questionable. The measurement of 1990s Slovak coin (Fig. 5b) proved presence of copper, tin and small amount of iron. This coin was measured using higher beam intensity (200 pA), and the measurement time was 20 min. The bremsstrahlung background was more than an order of magnitude higher than for the silver coin measurement. The calculated concentration of silver in the Slovak silver coin was 65 ± 5 %, and the rest was copper. The Slovak coin from 1990 had a dominating copper concentration of 85 ± 5 %, and the rest was tin (14 %) and iron (<1 %).

Table 2 Parameters of ion beam during PIXE analysis of laboratory standards

Sample	Ion beam	Time (s)	Charge (nC)	Current (pA)
PIXE2	Proton	500	1.3 ± 0.4	2.6 ± 0.8
	Helium	700	9.6 ± 2.9	13.7 ± 4.1
PIXE3	Proton	325	2.0 ± 0.6	6.2 ± 1.9
	Helium	302	20 ± 6	66 ± 20
PIXE 4	Proton	716	2.0 ± 0.6	2.8 ± 0.8
	Helium	506	20 ± 6	40 ± 12

Conclusions

First results obtained with the PIXE beam line installed at the Bratislava CENTA tandem accelerator facility are presented. The PIXE reaction chamber is equipped with a vertically movable sample holder for positioning of up to eight samples depending on their dimensions. The holder is capable of rotation around its vertical axis to adjust the angle how the incident beam should hit the sample. Proton and ^{4}He ion beams produced in the alphatross ion source and accelerated in the 3 MV Pelletron were used in the investigations. Optimization of the proton and helium beams from the alphatross ion source through the injection beam-line, the Pelletron tandem accelerator, the high-energy analyzer and the PIXE beam line were carried out. Results obtained with the ^{4}He ion beam were showing better detection limits when compared with protons of the same energy and beam intensity. For detection of produced X-rays, a BEGe detector has been used, covering the energy range from 3 keV to 3 MeV. Analyses of PIXE laboratory standards and old silver coins with ^{4}He ions of 3.5 MeV energy showed reproducible results, however, the uncertainties of single measurements were about 10 % that requires further improvements.

Further plans at the CENTA laboratory include developments of the PIXE technique for aerosol analysis, and a nuclear capillary microprobe [30] line for analysis of biological and historical samples.

Acknowledgments A support provided by the EU Research and Development Operational Program funded by the ERDF (projects 26240120012, 26240120026 and 26240220004) and by the

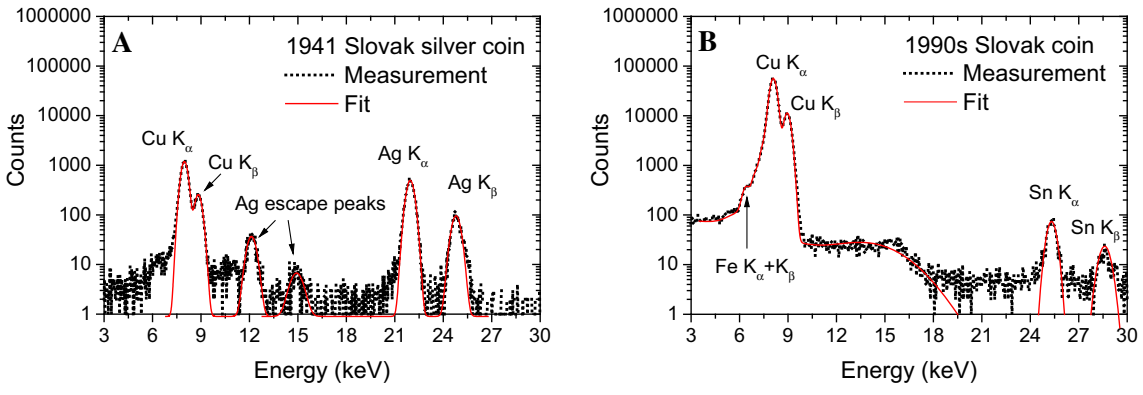

Fig. 5 PIXE analysis of two Slovak coins

International Atomic Energy Agency (project SLK 0/008) is highly acknowledged.

References

1. Johansson SAE, Johansson TB (1976) Nucl Instrum Method 137:473–516
2. Nastasi M, Meyer JW, Wang Y (2015) Ion beam analysis: fundamentals and applications. CRC Press, Boca Raton
3. Tanaka R, Yuge K, Kawai J, Alawadhi H (2016) Artificial peaks in energy dispersive X-ray spectra: sum peaks, escape peaks, and diffraction peaks. X-Ray Spectrom. doi:10.1002/xrs.2697
4. ETH Ion Beam Physics Website (2016). https://www1.ethz.ch/ams/research/material/iba/pixe
5. Cohen DD, Clayton E (1989) Ion beams for materials analysis. Academic Press, New York
6. Johansson SAE (1992) Int J PIXE 2:33
7. Simon MJ, Döbeli M, Müller AM, Synal HA (2012) Nucl Instrum Meth Phys Res B 273:237–240
8. Zhong L, Zhuang W, Shen H, Mi Y, Wu Y, Liu B, Yang M, Cheng H (2007) Nucl Instrum Meth Phys Res B 260:109–113
9. Lyubenova L, Pongrac P, Vogel-Mikuš K, Mezek GK, Vavpetič P, Grlj N, Regvar M, Pelicon P, Schröder P (2013) J Hazard Mater 248–249:371–378
10. Linke R, Schreiner M, Demortier G (2004) Nucl Instrum Meth Phys Res B 226:172–178
11. Ben Abdelouahed H, Gharbi F, Roumié M, Baccouche S, Ben Romdhane K, Nsouli B, Trabelsi A (2010) Mater Charact 61:59–64
12. Roumié M, Nsouli B, Chalhoub G, Hamdan M (2010) Nucl Instrum Meth Phys Res B 268:1916–1919
13. Tripathy BB, Rautray TR, Rautray AC, Vijayan V (2010) Appl Radiat Isot 68:454–458
14. Calzolai G, Chiari M, Lucarelli F, Nava S, Taccetti F, Becagli S, Frosini D, Traversi R, Udisti R (2014) Nucl Instrum Meth Res B 318:125–129
15. Ivošević T, Orlić I, Radović IB (2015) Nucl Instrum Meth Res B 363:119–123
16. Micheletti MI, Murruni LG, Debray ME, Rosenbusch M, Graf M, Cadena GA, Vitale P, Davidson J, Somacal H (2012) Nucl Instrum Meth Phys Res B 288:10–17
17. Saitoh K, Sera K, Shirai T (2008) Atmos Res 89:324–329
18. Silverthorn DU (2012) Human physiology: an integrated approach. Pearson, Boston
19. Fiedler A, Reinert T, Morawski M, Brückner G, Arendt T, Butz T (2007) Nucl Instrum Meth Phys Res B 260:153–158
20. Manuel JE, Rout B, Szilasi SZ, Bohara G, Deaton J, Luyombya H, Briski KP, Glass GA (2014) Nucl Instrum Meth Phys Res B 332:37–41
21. Watt F, Rajendran R, Ren MQ, Tan BKH, Halliwell B (2006) Nucl Instrum Meth Phys Res B 249:646–652
22. Povinec PP, Masarik J, Ješkovský M, Kaizer J, Šivo A, Breier R, Pánik J, Staníček J, Richtáriková M, Zahoran M, Zeman J (2015) Nucl Instrum Meth Phys Res B 361:84–87
23. NEC Website (2016) Ion sources tutorial. http://www.pelletron.com/tutor.htm
24. Campbell JL, Boyd NI, Grassi N, Bonnick P, Maxwell JA (2010) Nucl Instrum Meth Phy Res B 268:3356–3363
25. Heirwegh CM, Campbell JL, Czamanske GK (2016) Nucl Instrum Meth Phys Res B 366:40–50
26. Campbell JL, Czamanske GK, MacDonald L, Teesdale WJ (1977) Nucl Instrum Meth Phys Res B 130:608–616
27. Ebrahim AM, Etayeb MA, Khalid H, Noun M, Roumié M, Michalke B (2014) Appl Radiat Isot 90:218–224
28. Ortega-Feliu I, Moreno-Suárez AI, Gómez-Tubío B, Ager FJ, Respaldiza MA, García-Dils S, Rodríguez-Gutiérrez O (2010) Nucl Instrum Meth Phys Res B 268:1920–1923
29. Calligaro T, Gonzalez V, Pichon L (2015) Nucl Instrum Meth Phys Res B 363:135–143
30. Simon MJ, Döbeli M, Müller AM, Synal H-A (2012) Nucl Instrum Meth Phy Res B 273:237–240

Appendix B

Pelletron transmission efficiency measurements for ^{9}Be and ^{12}C ions at the CENTA laboratory

Acta Physica Universitatis Comenianae
Volume LIII (2016) 95–100

Pelletron Transmission Efficiency Measurements for ^{9}Be and ^{12}C Ions at the CENTA Laboratory*

J. Zeman, M. Ješkovský, J. Pánik, J. Staníček, P. P. Povinec

Centre for Nuclear and Accelerator Technologies, Department of Nuclear Physics and Biophysics, Faculty of Mathematics, Physics and Informatics, Comenius University, 842 48, Bratislava, Slovakia

Abstract: A new CENTA (Centre for Nuclear and Accelerator Technologies) laboratory was established at the Faculty of Mathematics, Physics and Informatics of the Comenius University in Bratislava. The research field of this facility can be divided in two main parts: Accelerator Mass Spectrometry (AMS), and ion beam applications, which include Ion Beam Analysis (IBA) and Ion Beam Modification (IBM) techniques. Transmission efficiency calculations and measurements for ^{9}Be and ^{12}C ions accelerated by the Pelletron tandem are presented. Measurements were done for different terminal voltage and stripper gas pressures of the tandem accelerator.

1. Introduction

The principal device of the CENTA laboratory is linear tandem accelerator Pelletron with two ion sources and several ion optics devices for ion beam manipulation. For proper functionality of the whole system many calibration and optimization measurements were elaborated. Tandem accelerator transmission efficiency for various ions is one of the key features of this system. Further development of ion beam applications depends on the determination of this property. For tandem accelerators is crucial the usage of negative ions which are being stripped in acceleration process inside the Pelletron.

Tandem acceleration in Pelletron proceeds in two steps: firstly, negative ions are accelerated towards the positive potential of the terminal electrode (where ions change their charge in the stripping process) and secondly, positive ions are accelerated by positive potential of the terminal electrode. In this way the energy gained in tandem acceleration is doubled compared to a single acceleration process using the same potential voltage on terminal electrode.

Stripping is being done by introducing either foils or stripper gas into acceleration tube inside the volume of the terminal electrode, which is held on a positive potential. The quality of the stripping process determines the amount of ions, which change their electric charge from negative to positive. CENTA's Pelletron system incorporates gas-stripping technology with nitrogen as stripper gas.

Negative ions are produced in ion source where they gain certain injection energy (tens of keV). Using ion optics devices for beam transmission through the system, certain type of ions can be selected and injected into the Pelletron. These ions are accelerated to energies of several MeV, separated using high-energy ion optics devices and detected in the end of the beam line detector.

*) Dedicated to Prof. V. Martišovitš 75-th anniversary

The quality of stripping process is defined by transmission efficiency. In literature it is possible to find different terms such as stripping efficiency or stripping yield [1], or charge state fraction [2], or transmission efficiency [3], but all of them describe the same quantity. Transmission efficiency is used for description of stripping process effectivity for different ions and different charge states of a certain ion. Negative ions enter stripping channel, i.e., volume of beam line which contains stripper gas. Via interactions with gas molecules, electrons are being stripped from negative ions so the ions become positive. Depending on the ion mass, the stripper gas pressure and the energy of ions, various final charge states of positive ions are being accelerated in the second phase of the tandem acceleration process. Consequently, ions gain various amount of acceleration so they are leaving the Pelletron at different energies. Knowledge of the quality of the stripping process is very important for analysis of ions and for further applications.

2. Experimental

The CENTA laboratory has been equipped with these main units:

(i) MC-SNICS ion source for solid targets
(ii) Alphatross ion source for gaseous targets
(iii) Ion injection system with electrostatic and electromagnetic analyzers
(iv) Tandem Pelletron accelerator
(v) High-energy analyzers with switching magnet and beam-line detectors.

All equipment has been supplied by National Electrostatic Corp. (USA).

3. Transmission efficiency calculation

For the production of ^{9}Be and ^{12}C ion beams the MC-SNICS ion source has been used [4]. The injected energy from the source was set at 61 keV. Pelletron is designed for maximal terminal voltage of 3 MV. Measurements were done for 4 values of terminal voltage: 1.8 MV, 2.1 MV, 2.4 MV and 2.7 MV. For Pelletron transmission efficiency determination we measured intensities of ion beams before the acceleration in the Pelletron (at a low energy side) and after the acceleration at the end of the beam line. Consequently, for the transmission efficiency calculation we used the equation:

$$T = \frac{I_{out}/n}{I_{in}} 100\ [\%] \qquad (1)$$

where I_{out} is the beam electric current at the end of the beam line measured by Faraday cup, denoted as FC05 [5], the $n = 1, 2, 3 \ldots$ is the charge state of ions presented in the beam, and I_{in} is the beam electric current measured by Faraday cup, denoted as FC02 [6], before the acceleration. Our aim was to determine the dependency of the transmission efficiency from the gas pressure in stripping channel of the Pelletron.

We also determined a stripping gas pressure dependency of the transmission efficiency for ^{9}Be and ^{12}C ions. The pressure of stripping gas was slowly increased in several steps from the starting point at 2 μbar up to the end point at 70 μbar. For each value of this pressure we measured values of electric currents in Faraday cups FC02 and FC05 for calculation of transmission efficiencies.

3.1. Transmission efficiency for ^{9}Be ion beam

As a source material for ^{9}Be ion beam we used beryllium oxide (BeO). Beryllium was extracted from the ion source MC-SNICS [7] in a form of molecular ions BeO^{-}. These ions then formed an ion beam, which was accelerated in Pelletron at different values of terminal voltage. Molecular ions BeO^{-} passing through the stripping channel are dissociated into atomic ions of ^{9}Be and ^{16}O. In the stripping process most of these ions gain certain positive charge, and according to this charge state they gain certain acceleration in the electrostatic field of the terminal electrode, which is held at high positive voltage. The energy of such accelerated ions can be calculated using the equation:

$$E = \frac{m}{M}(E_i + e\,TV) + n e\,TV \tag{2}$$

where m is the atomic mass of accelerated ions, M is the atomic mass of molecular ions entering the accelerator, E_i is the injection energy of ions entering the accelerator, e is the elementary electric charge, TV is the terminal voltage and n is the charge state of accelerated ions. We were interested in ^{9}Be ions, so m = 9 and M = 25. After acceleration we observed charge states 1^{+}, 2^{+} and 3^{+} of ^{9}Be ions. Fully stripped ions, i.e., charge state 4^{+}, were not measured because Faraday cups' lower limit is 0.1 nA, and the intensity of $^{9}Be^{4+}$ beam was below this value. Table 1 shows the energies of ^{9}Be ions according to the charge state and terminal voltage used for transmission efficiency measurements and calculations. Stripper gas pressure dependency of ^{9}Be transmission efficiency is shown in Figure 1. Notice that the transmission efficiency for 3^{+} charge state has a different scale on the right axis.

Table 1. Energy of ^{9}Be ions depending on the terminal voltage and the charge state. Energy of ions was calculated using the Equation (2).

Ion	Terminal voltage (MV)			
	1.8	**2.1**	**2.4**	**2.7**
$^{9}Be^{1+}$	2.47 MeV	2.88 MeV	3.29 MeV	3.69 MeV
$^{9}Be^{2+}$	4.27 MeV	4.98 MeV	5.69 MeV	6.39 MeV
$^{9}Be^{3+}$	6.07 MeV	7.08 MeV	8.09 MeV	9.09 MeV

3.2. Transmission efficiency for ^{12}C ion beam

For the ^{12}C ion beam produced in the MC-SNICS ion source we used a target in the form of graphite deposited on iron powder. C-ion beam was extracted from this source. The energy of accelerated ^{12}C ions was calculated using the equation:

$$E = E_i + (n+1)\,e\,TV \tag{3}$$

where E_i is the injection energy of ions entering the accelerator, n is the charge state of accelerated ions, e is the elementary charge and TV is the terminal voltage.

After the acceleration we observed only these charge states of ^{12}C ions: 2^{+}, 3^{+} and 4^{+}. We were not able to measure charge state 1^{+}. The reason was that the switching magnet [8] which deflects the beam to 45°beam line, where all charge states were measured, was not able to deflect the $^{12}C^{1+}$ beam at 1.8 MV of terminal voltage. For this mass, the charge state and the energy of ions, the magnetic induction of the switching magnet should be around

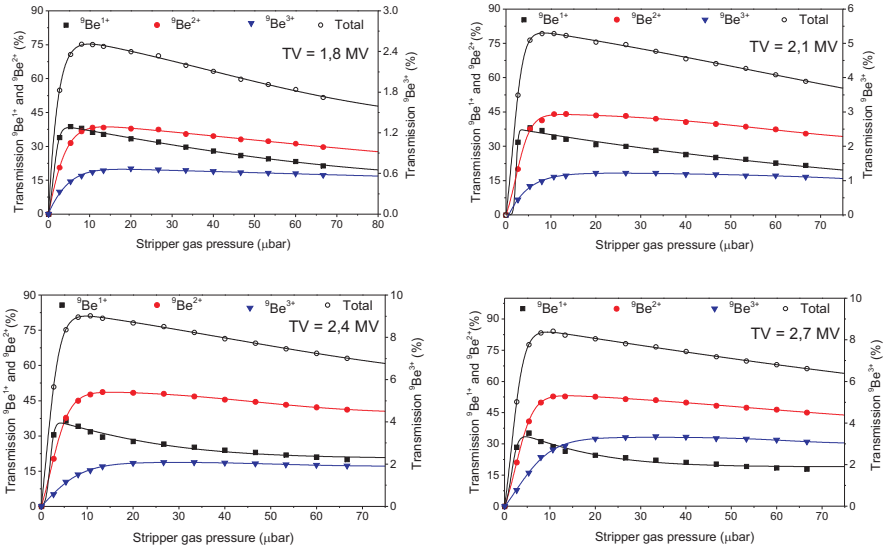

Fig. 1. ^{9}Be transmission efficiency for 1.8 MV, 2.1 MV, 2.4 MV and 2.7 MV terminal voltage. There are shown values for each charge state and the total transmission efficiency (i.e., the sum of transmission efficiencies of individual charge states).

1.5 T, but the maximum value of the magnetic induction that is switching magnet capable to reach is only around 1.4 T. Charge states 5^{+} and 6^{+} were not observed because of Faraday cup's lower detection limit at 0.1 nA, so we were not able to determine the transmission efficiency for these ions. Table 2 shows calculated energies for ^{12}C charge states according to the terminal voltage used for tandem acceleration. The energy values were obtained using the equation (3).

Table 2. Energy of ^{12}C ions depending on the terminal voltage and the charge state. Values of energy were calculated using the equation (3).

Ion	Terminal voltage (MV)			
	1.8	2.1	2.4	2.7
$^{12}C^{2+}$	5.46 MeV	6.36 MeV	7.26 MeV	8.16 MeV
$^{12}C^{3+}$	7.26 MeV	8.46 MeV	9.66 MeV	10.86 MeV
$^{12}C^{4+}$	9.06 MeV	10.56 MeV	12.06 MeV	13.56 MeV

Transmission efficiencies for ^{12}C ions dependent on stripper gas pressure are shown in Fig. 2. Values of transmission efficiency for 4^{+} charge state has different scale on the right axis.

For the ^{9}Be ions, the maximal transmission efficiency was measured at 2.7 MV terminal voltage for 2^{+} charge state at a region of stripper gas pressures from 10 to 20 μbar. The energy of these ions at this terminal voltage was 6.39 MeV, and the transmission efficiency was roughly 53 %. Maximal transmission efficiency for ^{12}C ions was achieved at terminal voltage of 2.7 MV for 3^{+} charge state at a region of stripper gas pressures from 20 to 33 μbar. The energy of these ions was 10.86 MeV, and the transmission efficiency reached almost 48 % (Table 3).

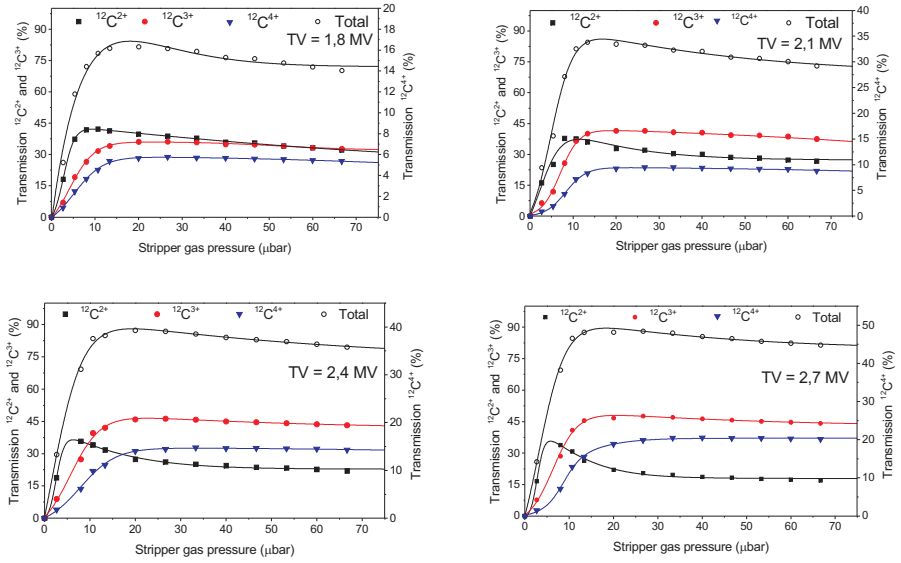

Fig. 2. ^{12}C Transmission efficiency for 1.8 MV, 2.1 MV, 2.4 MV and 2.7 MV terminal voltage. There are shown values for each charge state and the Total transmission efficiency, i.e., the sum of transmission efficiencies of individual charge states.

Table 3. Maximal values of transmission efficiencies measured for ^{9}Be and ^{12}C ions. These values were obtained at 2.7 MV terminal voltage. The energy of ions was calculated using the equations (2) and (3).

Parameters	$^{9}Be^{2+}$, E = 6.39 MeV			$^{12}C^{3+}$, E = 10.86 MeV		
Stripper gas pressure [μbar]	10.67	13.33	20.00	20.00	26.66	33.33
Transmission efficiency [%]	52.88	52.86	52.68	46.71	47.72	47.08
Standard deviation [%]	1.32	1.32	1.32	1.17	1.19	1.18

4. Conclusions

Transmission efficiencies for ^{9}Be and ^{12}C ions were determined for four values of terminal voltage and their dependence on the stripper gas pressure. A successive increase of the transmission efficiency with increasing stripper gas pressure to a certain point was observed, followed by a decrease of the transmission efficiency towards higher stripper gas pressures. The reason for such behavior is that with increasing the stripper gas pressure, both the electron stripping (which affects the transmission efficiency) and ion scattering on molecules of the stripper gas have been rising. Each ion has a combination of charge state and energy (guided by the terminal voltage of the tandem accelerator) that at a certain value of stripper gas pressure the scattering process starts to reduce the final transmission efficiency. This decrease is stronger for lower charge states, $^{9}Be^{1+}$ and $^{12}C^{2+}$, than for their higher charge states. The decrease of transmission efficiency for higher charge states is much smoother which can be used for better stability of ion beams at these regions of stripper gas pressure for various applications, e.g. for ion irradiation or for

applications of IBA techniques, which require stable ion beams. Working in these stable regions of transmission efficiency is not affected by slight changes in the stripper gas pressure.

Acknowledgements

A support provided by the EU Research and Development Operational Program funded by the ERDF (projects Nos. 26240120012, 26240120026 and 26240220004) has been crucial for establishing the CENTA laboratory. The authors are also acknowledging support from the Technical Cooperation Program of the International Atomic Energy Agency (project No. SLR008). They are thankful to the staff of the Faculty of Mathematics, Physics and Informatics for assistance during various stages of preparation and building of the CENTA facility.

References

[1] P. Steier Exploring the Limits of VERA: A Universal Facility for Accelerator Mass Spectrometry, Dissertation, p. 57–64, Institut für Isotopenforchung und Kernphysik, VERA Labor, Vienna, 2000.
[2] S. R. Winkler et al. He Stripping for AMS of ^{236}U and Other Actinides Using a 3 MV Tandem Accelerator, Nuclear Instruments and Methods in Physics Research **B 361** (2015) 461.
[3] S. Maxeiner et al., Simulation of Ion Beam Scattering in a Gas Stripper, Nuclear Instruments and Methods in Physics Research **B 361** (2015) 242.
[4] National Electrostatics Corp., Instruction Manual No. 2JT045500 for MC-SNICS Ion Source. Middleton, 2011.
[5] National Electrostatics Corp., Instruction Manual No. 2ET925001 for Faraday Cup Model no. FC18. Middleton, 2011.
[6] National Electrostatics Corp., Instruction Manual No. 2ET952300 for Faraday Cup Model no. FC50. Middleton, 2011.
[7] *http://www.pelletron.com/negion.htm*
[8] National Electrostatics Corp., Instruction Manual No. 2BA017470 for Switching Magnet. Middleton, 2011.

Appendix C

Development of the Accelerator Mass Spectrometry technology at the Comenius University in Bratislava

Nuclear Instruments and Methods in Physics Research B 361 (2015) 87–94

Contents lists available at ScienceDirect

Nuclear Instruments and Methods in Physics Research B

journal homepage: www.elsevier.com/locate/nimb

Development of the Accelerator Mass Spectrometry technology at the Comenius University in Bratislava

Pavel P. Povinec *, Jozef Masarik, Miroslav Ješkovský, Jakub Kaizer, Alexander Šivo, Robert Breier, Ján Pánik, Jaroslav Staníček, Marta Richtáriková, Miroslav Zahoran, Jakub Zeman

Comenius University, Faculty of Mathematics, Physics and Informatics, SK-84248 Bratislava, Slovakia

ARTICLE INFO

Article history:
Received 25 November 2014
Received in revised form 7 February 2015
Accepted 8 February 2015
Available online 16 March 2015

Keywords:
Accelerator Mass Spectrometry (AMS)
Pelletron
SNICS ion source
^{14}C line
CENTA

ABSTRACT

An Accelerator Mass Spectrometry (AMS) laboratory has been established at the Centre for Nuclear and Accelerator Technologies (CENTA) at the Comenius University in Bratislava comprising of a MC-SNICS ion source, 3 MV Pelletron tandem accelerator, and an analyzer of accelerated ions. The preparation of targets for ^{14}C and ^{129}I AMS measurements is described in detail. The development of AMS techniques for potassium, uranium and thorium analysis in radiopure materials required for ultra-low background underground experiments is briefly mentioned.

1. Introduction

Radiocarbon [1–5] and gamma-ray spectrometry laboratories [6–9] have been in operation at the Comenius University in Bratislava for over forty years focusing on investigations of long-lived cosmogenic radionuclides (e.g. in wine samples [10,11], in tree-rings [12,13], in lunar samples and meteorites [14–18]), as well as studying anthropogenic radionuclides in the environment [19,20]. We have been collaborating with several AMS laboratories on the analysis and evaluation of cosmogenic and anthropogenic radionuclides (^{10}Be, ^{14}C, ^{129}I, uranium and plutonium isotopes) in different matrices, including atmospheric aerosols, rainwater, seawater, and marine sediments [21–33]. Knowing the benefits of AMS for ultra low-level isotope analyses, it was therefore very natural that this technology has been of great interest for our future developments.

Following our previous experience and close cooperation with AMS laboratories in Tucson [34], Toronto [35] and Vienna [36] with a wide range of AMS applications, we have focused on a development of a tandem accelerator complex, which could cover a wide range of applications. A Centre for Nuclear and Accelerator Technologies (CENTA) has been established recently at the Comenius University in Bratislava (Slovakia) comprising of a state-of-the art tandem accelerator laboratory designed for ion beam studies and AMS [37]. In this paper, we focus on the laboratory design for AMS studies, preparation of targets, and discussion of the main characteristics.

2. Tandem accelerator laboratory

The present laboratory design for AMS was due to limited financial support restricted to an ion source for solid targets, the injection system, the 3 MV tandem accelerator, and a simple high energy analyzer with ion beam end station (Fig. 1). All available equipment was supplied by the National Electrostatics Corporation (NEC, Middleton, USA). The installation, which we expect to be completed in the near future, will include a fully equipped AMS line with 90°magnet, an electrostatic spectrometer, and the end of the line detector. A dedicated hall to accommodate the tandem accelerator laboratory has been built at the Comenius University campus at Mlynská dolina. The hall design separates the AMS line (the large magnet will be placed just after the Pelletron) from the ion beam channels (which will be shifted together with the switching magnet into a bunker covered by soil), enabling work in different radiation environments (Fig. 1). A detail description of the tandem accelerator laboratory is given in [37], here we present only the main characteristics.

The MC-SNICS source (MultiCathode Source of Negative Ions by Cesium Sputtering) to be used in AMS measurements has a wheel

* Corresponding author. Tel.: +421 260295544; fax: +421 265425882.
E-mail address: povinec@fmph.uniba.sk (P.P. Povinec).

http://dx.doi.org/10.1016/j.nimb.2015.02.021
0168-583X/

accommodating up to 40 solid targets [38]. A wide range of elements (from lithium to transuranics) can be used in the SNICS ion source (Figs. 1 and 2). After the production and extraction of ions from the SNICS source, the first E/q separation of the ions is made by an electrostatic analyzer (ESA) with electrodes of radius 300 mm, mounted on a rotatable platform. The momentum analysis (ME/q^2) and separation of ions before acceleration in the Pelletron is made by a double focusing 90° magnet with bending radius of 0.4572 m. The mass resolution of the injection magnet is $m/\Delta m = 305$. After the proper mass is selected, set of slits is used for parameterization of the beam, and a Faraday cup is used for measurements of ion currents. Negative ions are then injected into the tandem accelerator. The 3 MV tandem electrostatic accelerator (NEC Model 9SDH-2 Pelletron) [39] is used for accelerating ions over a broad range of energies (Figs. 1 and 2). The terminal has a nitrogen gas stripping system. After acceleration, ions are analyzed by the switching magnet ($ME/Z^2 = 300$ amu-MeV @ ± 15°), which is equipped with seven ports at ±45°, ±30°, ±15°, and 0° with respect to the accelerator. The beam line at +45° is currently equipped with slits, *X–Y* electromagnetic steerers, Faraday cups for current measurements and with beam profile monitor. A dedicated beam line for AMS analysis consisting of a 90° magnet ($ME/Z^2 = 170$ amu-MeV), will be installed soon just after the Pelletron, followed by an electrostatic analyzer, and the end of the line detector.

The first AMS studies at the CENTA laboratory focused on transmission characteristics of accelerated Be ions with different energy and charge states, and varying gas pressure in the gas stripper of the Pelletron [37]. As the AMS line at the CENTA laboratory does not yet include a fully capable analyzing system, the possibility of measuring ^{10}Be using only a switching magnet as the ion analyzer was tested. A detail description of the method is presented in [37], here we mention only that even with a small switching magnet a good separation of $^{10}Be^{2+}$ and $^{9}Be^{3+}$ ions can be obtained. A detection limit for $^{10}Be/^{9}Be$ of the order of 10^{-12} was achieved, which was mainly limited by scattering of $^{9}Be^{2+}$ ions (energy of 7.059 MeV) on residual gas inside the switching magnet.

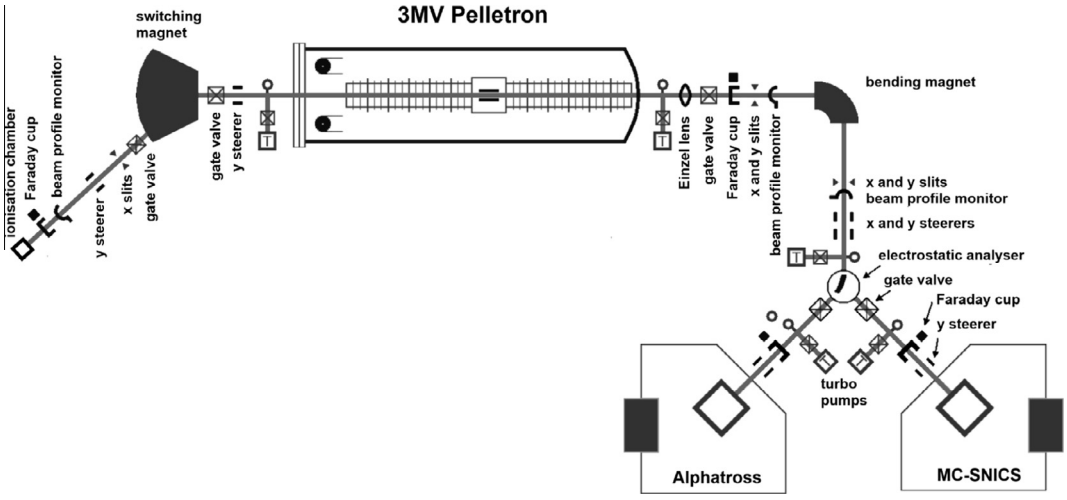

Fig. 1. Scheme of the tandem accelerator laboratory used for AMS measurements.

Fig. 2. Photos of the main parts of the tandem laboratory.

3. Preparation of targets for AMS measurements

3.1. Production of graphite targets

The vacuum line for preparation of graphite samples for ^{14}C measurements using AMS is of the same design as described by Liong Wee Kwong et al. [40], however, hydrogen used in the reaction is supplied directly from a gas cylinder. The graphitization line is located in a clean laboratory dedicated for preparation of radiocarbon samples. It is made of borosilicate glass and is used for extraction of CO_2 from various samples, e.g. groundwater, seawater, solid carbonates and organic samples that require either combustion or acid evolution of CO_2. The line has also advantage in extracting carbon dioxide and its graphitization in the same place, what substantially lowers a risk of contamination. The vacuum in the line, which is constantly monitored by Pirani and Magneton gauges (Edwards), can reach down to $\sim 10^{-5}$ torr with the use of rotary and diffusion pumps.

The well-known Bosch reaction [41] is exploited for graphite preparation:

$$CO_2 + 2H_2 \xrightarrow{\text{Fe, } 550-990\ ^\circ C} C(s) + 2H_2O \quad (1)$$

The reaction is consecutive:

$$CO_2 + H_2 \xrightarrow[-H_2O]{\text{Fe, } 550-990\ ^\circ C} CO + H_2 \xrightarrow[-H_2O]{\text{Fe, } 550\ ^\circ C} C(s) \quad (2)$$

Prior to reaction (1), an appropriate amount of Fe catalyst is weighed into a reaction tube, which is mounted on a graphitization reactor, and pre-heated in the presence of hydrogen. Hydrogen gas (purity of 99.9%), used for the catalyst activation and graphitization itself, is supplied from a pressurized gas bottle, which can be directly connected to a graphitization reactor. The amount of hydrogen used for graphitization equals approximately double the amount of the CO_2 sample. Typically, the reaction is ended in less than 4 h with a yield of 98%, which is calculated from the pressure decline during the reaction, and also confirmed gravimetrically.

A graphitization reactor is comprised of a reaction tube (with the iron catalyst inside), heated with an electric oven, a water trap (a tube cooled with methanol and liquid nitrogen to about −45 °C) and a pressure transducer (for monitoring of the pressure during the graphitization). All parts are joined together by stainless-steel connectors (Swagelok) and FPM O-rings (Fig. 3). There are 4 reactors altogether in the graphitization line, one with total volume of 18.2 mL, and three with total volume of 9.1 mL.

To reduce time consumption and increase the final yield of the graphitization, several parameters including reactor volume, amount of iron catalyst and its type, temperature and catalyst activation conditions, were optimized. Results of the optimization can be summarized as follows:

(i) Increasing the reactor volume from 9.1 mL to 18.2 mL enhanced the yield by 6%, and shortened the reaction time by 80 min.
(ii) Varying of the Fe-catalyst amount has a little or no effect; an optimal value was set at 4–6 mg.
(iii) Three types of iron powder from three different suppliers – Acros (97%, 325 mesh), Aldrich (97%, 325 mesh) and Alfa Aesar (99%, 200 mesh) were tested. The Aldrich powder had the best performance, and it has been used therefore in routine work.
(iv) As it has been reported in [42], the first step of the overall reaction (1) – the reduction of CO_2 to CO – could be improved if done at higher temperature, i.e. 900 °C. After 0.5 h the temperature is lowered to 550 °C for the rest of the graphitization.
(v) Heating of the iron powder in the presence of hydrogen (600 °C, 1 h) was chosen as the standard catalyst activation procedure, though, if compared to heating in the open atmosphere and vacuum, respectively, the yield and time differences were rather small.

A comparison of the history of two graphitization processes, expressed as the reactor pressure – one with and one without implemented optimized parameters, is presented in Fig. 4. Clearly, the optimization resulted in a much faster reaction (a time saving of more than 1.5 h), and slightly increased yield (from 94% to 98%).

Graphite targets from samples of different origin were prepared, e.g. from atmospheric carbon dioxide, tree rings, groundwater, painting canvas, parchment sheets from books, archeological samples, etc. As the Bratislava laboratory does not have at present a fully equipped AMS line for ^{14}C analyses, measurements have been carried out in Tucson, Vienna and Debrecen AMS laboratories.

3.2. Production of AgI targets

Two methods for total inorganic ^{129}I separation from water samples were studied at CENTA: solvent extraction and anion exchange chromatography. Both methods result in the preparation of silver iodide as the most suitable target material for ^{129}I AMS measurements [43,44].

3.2.1. Solvent extraction

The solvent extraction procedure, which exploits the solubility difference of the solute in two immiscible solvents, is based on the method described in [21], though some minor modifications have been applied. The procedure is shown in Fig. 5. After passing the water sample through a 0.45 μm membrane filter, an appropriate amount of iodine carrier with known $^{129}I/^{127}I$ ratio (e.g. Woodward iodine) is added to the sample. Then, the sample is acidified with 65% w/w HNO_3 to pH value around 2, and a part of the total iodine, which is present in IO_3^- form, is reduced to the iodide form by addition of 1 M $NaHSO_3$ solution:

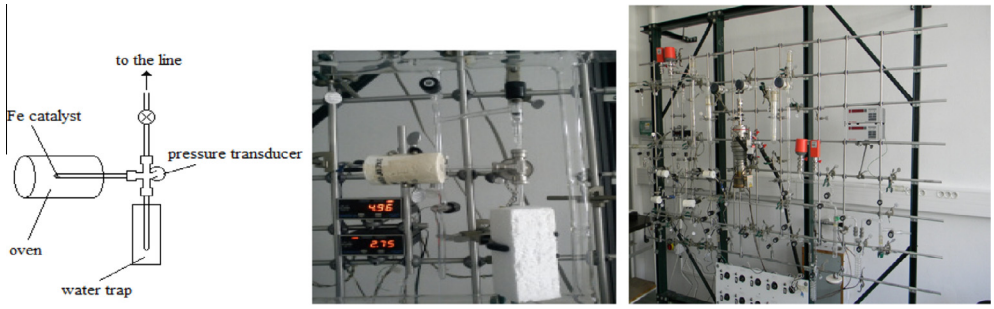

Fig. 3. Scheme of the graphitization reactor (left), its real image (center) and the graphitization line.

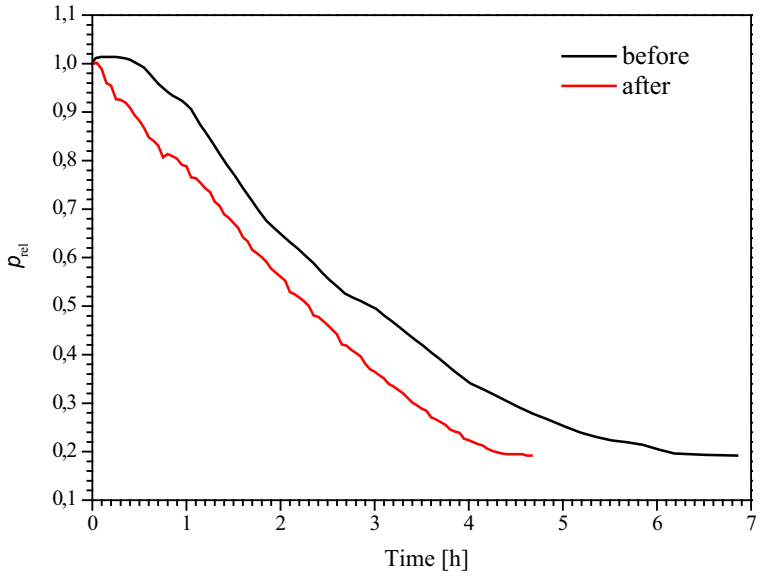

Fig. 4. Relative pressure in the reactor before (the upper line) and after (the bottom line) implementing the optimization.

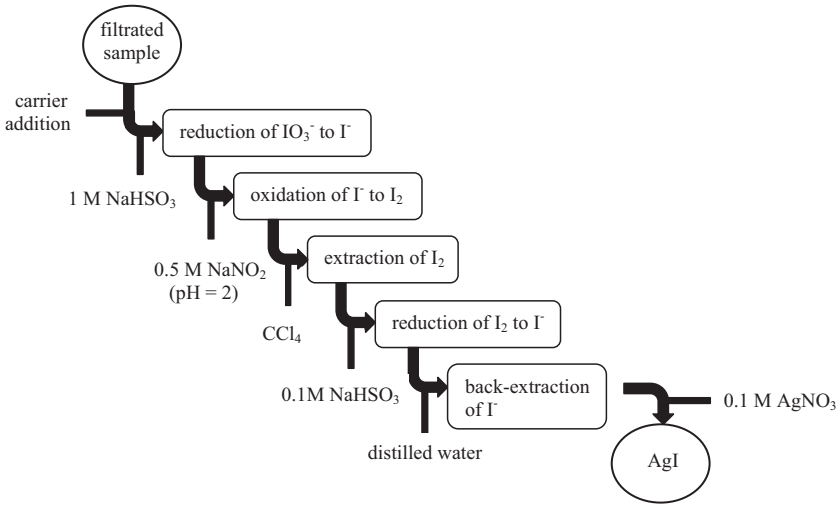

Fig. 5. Schematic diagram of ^{129}I separation by solvent extraction procedure.

$$IO_3^- + 3HSO_3^- \rightarrow I^- + 3HSO_4^- \quad (3)$$

As the reaction between IO_3^- to I^- is slow, it is necessary to wait for a few minutes to maximize the reduced fraction. Afterwards, iodide ions are oxidized with 0.5 M $NaNO_2$ solution to form water soluble I_2:

$$I^- + NO_2^- + 2H^+ \rightarrow 0.5I_2 + NO + H_2O \quad (4)$$

The sample of yellowish–brownish color is transferred to a clean separation funnel in which molecular iodine is extracted to CCl_4 ($k_D = [I_2]_{org}/[I_2]_{aq} \approx 86.2$). The organic phase with dissolved iodine is separated and a fresh portion of carbon tetrachloride is added. The extraction step is repeated 3–4 times. All violet-colored organic phase is poured into another separation funnel, together with a small amount of distilled water and 0.1 M $NaHSO_3$ solution. Here, molecular iodine is reduced to the iodide form and back-extracted to the aqueous phase:

$$I_2 + HSO_3^- + H_2O \rightarrow 2I^- + SO_4^{2-} + 3H^+ \quad (5)$$

The organic phase is discarded, and the water phase is acidified with 65% w/w HNO_3 to pH ~ 2, followed by the precipitation of AgI with low-concentrated 0.1 M $AgNO_3$ solution. Finally, the precipitate is filtrated (2.5 μm Whatman filter paper), washed intensively with dilute NH_4OH and distilled water, and dried in the oven at 60 °C overnight.

The chemical recovery of iodine, i.e. the chemical yield of the procedure, determined by the weight of prepared AgI precipitate is 60–70%. However, the yield can be overestimated by the presence of undesired silver salts, which do not dissolve completely in the washing step with NH_4OH solution. Furthermore, the method is limited by the sample volume (⩽1 L), and by the fact that one cannot work on two samples simultaneously.

To verify the quality of the final product, a sample prepared during the testing phase of the method was analyzed by a scanning electron microscope (SEM, TS 5136 MM, TESCAN Brno, Czech Republic) and energy dispersive X-ray spectrometer (EDS, INCA x-sight, Oxford Instruments Analytical, High Wycombe Bucks, UK). Fig. 6 shows results of this analysis, which can be compared

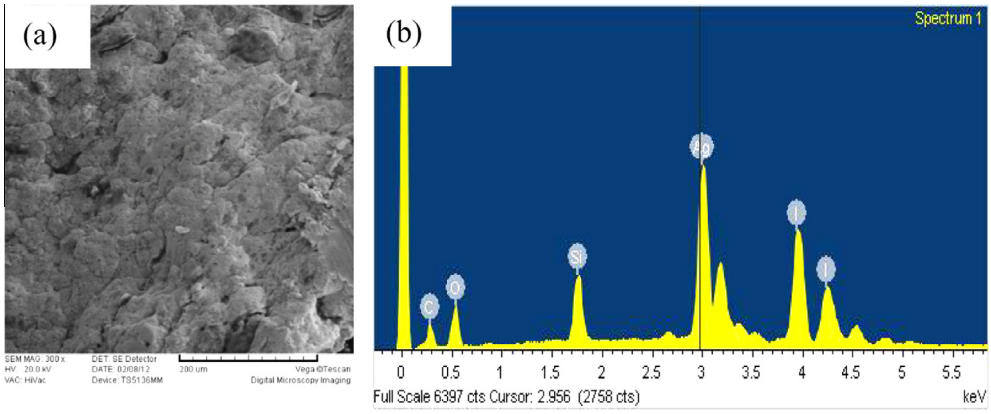

Fig. 6. (a) SEM micrograph (magnification 300×) and (b) EDS spectrum of AgI sample prepared during the testing phase of the solvent extraction method.

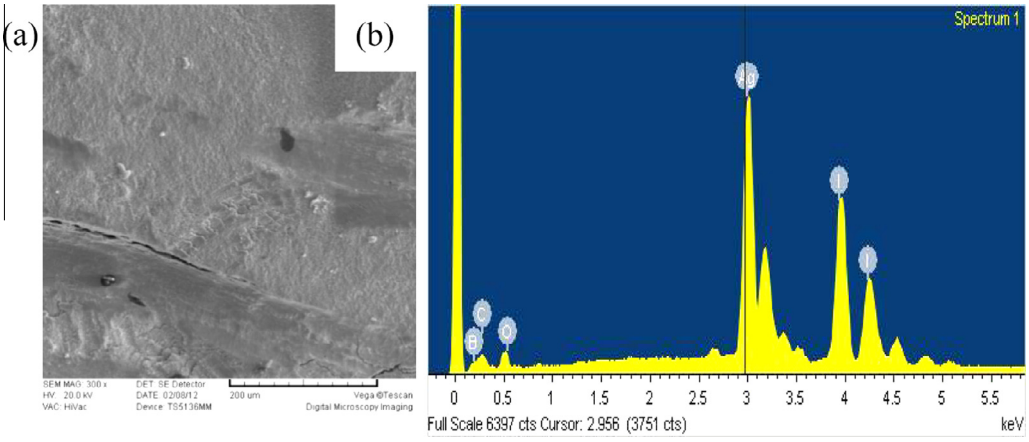

Fig. 7. (a) SEM micrograph (magnification 300×) and (b) EDS spectrum of 'standard' AgI sample prepared by direct precipitation of iodine carrier.

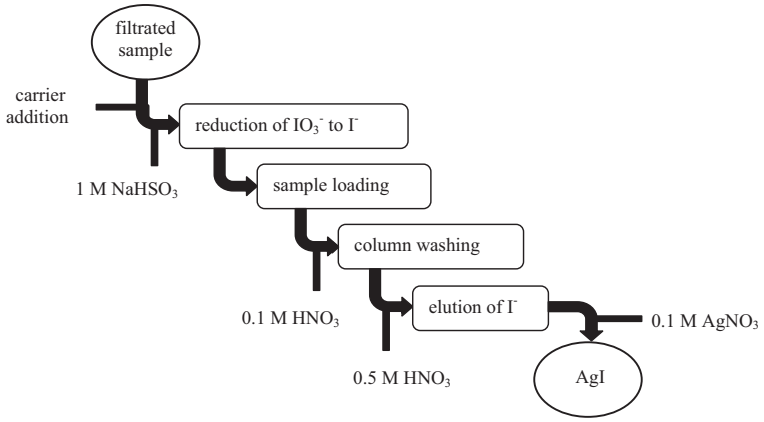

Fig. 8. Schematic diagram of ^{129}I separation by anion exchange chromatography.

with a 'standard' sample prepared by direct precipitation of AgI, i.e. by mixing iodine carrier with $AgNO_3$ solution in slightly acidic conditions (Fig. 7), which is in a good agreement with the result reported in [45]. The EDS spectrum of the testing sample (Fig. 6b) contains silicon and oxygen peaks, which are higher than in the spectrum of the 'standard' sample (Fig. 7b). This is supported by the clear difference in the surface structure (see Figs. 6a and 7a), suggesting a presence of the silicone grease (polydimethylsiloxane) in the final AgI precipitate. The silicone grease is used as a lubricant for the stopcock in separation funnels. It is expected, however, that this will not impact on AMS measurements.

3.2.2. Anion exchange chromatography

The second method (Fig. 8) for ^{129}I separation is based on the high selectivity of iodide ions for anion exchange resin and its

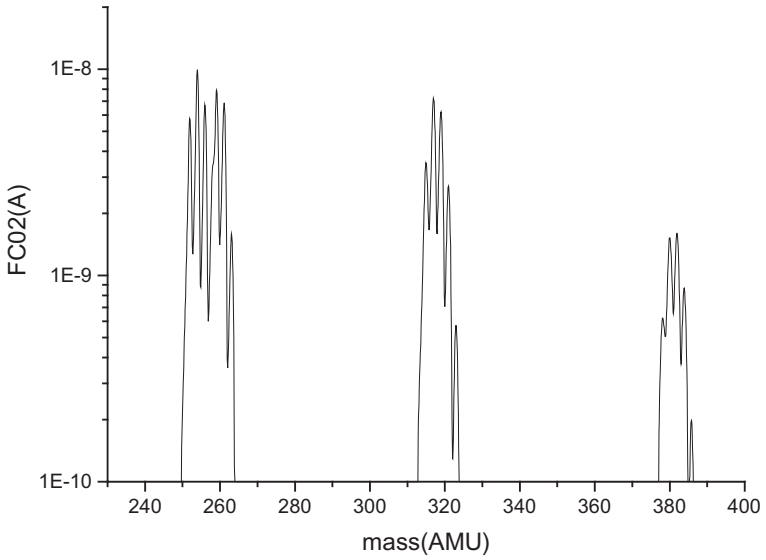

Fig. 9. Mass scan of ions from a copper target in the SNICS ion source at the entrance of the Pelletron accelerator (showing mostly Cu copper clusters of ^{63}Cu and ^{65}Cu ions).

consequent elution to the mobile phase by the use of a low concentration HNO_3 solution [46]. The first steps (filtration, carrier addition, acidification and reduction of IO_3^- fraction to I^-) are done in the very same way as in the case of solvent extraction (see above). Next, a clean chromatographic column (10 × 150 mm) is prepared and filled with strong anion exchange resin (DOWEX 1 × 8, 100–200 mesh, Cl^- form). By passing 1 M HNO_3 solution through the column the resin is first converted to NO_3^- form:

$$|-NR_3^+Cl^- + NO_3^- \rightarrow |-NR_3^+NO_3^- + Cl^- \quad (6)$$

The process is controlled by addition of $AgNO_3$ solution to the effluent; the white precipitate in the effluent suggests unfinished conversion. The pH value in the column is adjusted to the value of the sample which is then loaded on the column; anion exchange occurs as follows:

$$|-NR_3^+NO_3^- + I^- \rightarrow |-NR_3^+I^- + NO_3^- \quad (7)$$

The effluent is discarded and the resin is washed with 0.1 HNO_3 to remove interfering elements (e.g. Cl^-). Finally, the iodide ions strongly bound to the resin are eluted using 0.5 M HNO_3. The silver iodide precipitation and its additional treatment are executed in a similar way as in the case of the solvent extraction method.

Anion exchange chromatography, which can also be used for iodine speciation studies [47], is suitable for water samples with larger water volumes (1–5 L), in which the iodine concentration is quite low. On top of that, with this procedure it is easy to process two or even more samples at once. However, it is indeed more laborious and time-consuming than the solvent extraction method. The chemical yield is comparable with the solvent extraction method.

The AMS target itself is prepared in both methods by mixing AgI with silver powder (Alfa Aesar 99.9%, 635 mesh) in a weight ratio of 1:1, and pressing the mixture into a copper holder. Both methods were tested using seawater samples collected offshore of Fukushima, however, as the CENTA laboratory is not yet capable to analyze ^{129}I, AMS measurements were carried out in the Tucson and Vienna laboratories.

4. Radiopurity measurements of construction materials

One of the most important problems in underground physics experiments e.g. searching for neutrinoless double beta-decay of nuclei [48] or dark matter [49], is background from radioactive contamination of materials (mostly ^{40}K, and ^{232}Th, ^{235}U, ^{238}U and their decay products) used for construction of detectors. Radiopurity measurements of construction materials have mostly been carried out by non-destructive gamma-ray spectrometry with detection limits around 10 nBq/g [50]. A new generation of these experiments requires, however, decrease the detection limits at least by a factor of 50. Such very low-radioactivity measurements can be carried out only by AMS, preferably without any chemical treatment of samples, as this process could add radioactive contamination from chemicals used during sample processing. On the basis of previous experience with analysis of uranium in environmental samples, it is expected that measurable levels below 1 nBq/g (or around 0.1 pg/g) could be achieved. Typical samples for radiopurity tests include electrolytical copper, Mylar foils, stainless steel wires, various glues, etc. We have been focusing on radiopurity measurements of copper as this material is usually closest to the detector, and therefore its radiopurity has the dominant impact on the detector background.

We did preliminary tests with analysis of uranium in copper wire targets in the SNICS ion source. The copper wire was made of electrolytical copper with known ^{238}U concentration (~10 nBq/g), which we plan to use as a reference standard. There are two possibilities to extract uranium ions from the copper – either as uranium oxides or as a uranium compound with copper. Preliminary tests indicate that the first option is probably more advantageous. Fig. 9 shows mass spectra of ions measured after the injection magnet where ion clusters of ^{63}Cu and ^{65}Cu have been observed. The UO ions with mass of 254 can be expected in the first mass peak. Further investigations are on-going with optimization of ion acceleration as well as post-acceleration ion analyses.

5. Conclusions

The main results obtained in this study may be summarized as follows:

(i) The main characteristics of the AMS system, consisting of the SNICS ion source, the ion injection system, the Pelleteron accelerator with 3 MV terminal voltage, and the analyzer of accelerated ions were described.
(ii) A vacuum-cryogenic line for production of ^{14}C graphite targets was developed and operational characteristics were studied. Target developments for AMS analysis of ^{129}I in seawater were also presented. AMS ^{14}C measurements of

graphite targets prepared in Bratislava from different matrices such as seawater, groundwater, atmospheric carbon dioxide, wood, charcoal, bones, tree rings, and canvases, were carried out in collaboration with several AMS laboratories.

(iii) Development of AMS technique for potassium, uranium and thorium analysis in radiopure materials required for ultra-low background underground experiments was briefly mentioned as well.

Acknowledgements

The authors are indebted to Profs. R. Golser, A. Priller and P. Steier of the Vienna University for cooperation during development of the AMS system, Prof. X. Hou of the Technical University of Denmark for advise on development of AgI targets, and Mr. Ivan Kontul for assistance during preparation of graphite targets. This study was supported by the EU Research and Development Operational Program funded by the ERDF (projects # 26240120012, 26240120026 and 26240220004), and by the VEGA grant # 1/0783/14 from The Ministry of Education, Science, Research and Sport of the Slovak Republic.

References

[1] P. Povinec, Š. Šáro, M. Chudý, M. Šeliga, The rapid method of carbon-14 counting in atmospheric carbon dioxide, Int. J. Appl. Radiat. Isot. 19 (1968) 877–881.
[2] P. Povinec, Preparation of methane gas filling for proportional ^{3}H and ^{14}C counters, Radiochem. Radioanal. Lett. 9 (1972) 127–135.
[3] S. Usačev, P. Povinec, M. Chudý, Š. Šáró, Bratislava radiocarbon measurements I, Radiocarbon 15 (1973) 443–450.
[4] P. Povinec, Multiwire proportional counters for low-level ^{14}C and ^{3}H measurements, Nucl. Instr. Meth. 1978 (156) (1978) 441–445.
[5] P. Povinec, A study of proportional counter optimization for long term counting, Nucl. Instr. Meth. 163 (1979) 363–368.
[6] J. Staníček, P. Povinec, Internal pair production in alpha-decaying nuclei and gamma ray intensities of ^{241}Am, Nucl. Instr. Meth. B 17 (1986) 462–466.
[7] I. Sýkora, P. Povinec, Measurement of electron capture to positron emission ratios in light and medium nuclides, Nucl. Instr. Meth. B 17 (1986) 467–471.
[8] P. Povinec, M. Chudý, I. Sýkora, J. Szarka, M. Pikna, K. Holý, Aerosol radioactivity monitoring in Bratislava following the Chernobyl accident, J. Radioanal. Nucl. Chem. 126 (1988) 467–478.
[9] P.P. Povinec, Low-level gamma-ray spectrometry for environmental samples, J. Radioanal. Nucl. Chem. 276 (2008) 771–777.
[10] A.A. Burchuladze, S.V. Pagava, P. Povinec, G.I. Togonidze, S. Usačev, Radiocarbon variations with the 11-year solar cycle during the last century, Nature 287 (1980) 320–323.
[11] P. Povinec, A.A. Burchuladze, S.V. Pagava, G.I. Togonidze, Anthropogenic ^{14}C variations in atmospheric CO_2 and wines, Radiocarbon 31 (1989) 771–776.
[12] P. Povinec, A.A. Burchuladze, S.V. Pagava, Short-term variations in radiocarbon concentration with the 11-year solar cycle, Radiocarbon 25 (1983) 259–265.
[13] M.R. Attolini, M. Galli, T. Nanni, P. Povinec, A cyclogram analysis of the Bratislava tree-ring record during the last century, Radiocarbon 31 (1981) 839–843.
[14] P. Emrich, V. Jurina, P. Povinec, Cosmogenic ^{22}Na and ^{26}Al and track studies in Luna 16, 20 and 24 samples, Bull. Astron. Inst. Czechosl. 35 (1984) 253–257.
[15] P.P. Povinec, I. Sýkora, V. Porubčan, M. Ješkovský, Analysis of ^{26}Al in meteorite samples by coincidence gamma-ray spectrometry, J. Radioanal. Nucl. Chem. 282 (2009) 805–808.
[16] A. Kováčik, I. Sýkora, P.P. Povinec, V. Porubčan, Non-destructive gamma-spectrometry analysis of cosmogenic radionuclides in fragments of the Košice meteorite, J. Radioanal. Nucl. Chem. 293 (2012) 339–345.
[17] P.P. Povinec, J. Masarik, I. Sýkora, A. Kováčik, J. Beňo, M.M.M. Meier, R. Wieler, M. Laubenstein, V. Porubčan, Cosmogenic nuclides in the Košice meteorite: experimental investigations and Monte Carlo simulations, Meteorit. Planet. Sci. (2015) (in press).
[18] P.P. Povinec, M. Laubenstein, L. Ferrière, F. Brandstätter, I. Sýkora, A. Kováčik, A.J.T. Jull, D. Topa, C. Koeberl, The Chelyabinsk meteroid – what we learned from the recovered meteorite fragments?, Meteoritics Planet Sci. 50 (2015) 273–286.
[19] P.P. Povinec, A. Šivo, J. Šimon, M. Richtáriková, K. Holý, Impact of the Bohunice nuclear power plant on atmospheric radiocarbon, Appl. Radiat. Isot. 66 (2008) 1686–1690.
[20] P.P. Povinec, K. Holý, M. Chudý, A. Šivo, I. Sýkora, M. Ješkovský, M. Richtáriková, Long-term variations of ^{14}C and ^{137}Cs in the Bratislava air – implications of different atmospheric transport processes, J. Environ. Radioact. 108 (2012) 33–40.
[21] P.P. Povinec, B. Oregioni, A.J.T. Jull, W.E. Kieser, X.-L. Zhao, AMS measurements of ^{14}C and ^{129}I in seawater around radioactive waste dump sites, Nucl. Instr. Meth. Phys. Res. B 172 (2000) 672–678.
[22] S.H. Lee, J. Gastaud, J.J. La Rosa, L. Liong Wee Kwong, P.P. Povinec, E. Wyse, L.K. Fifield, P.A. Hausladen, L.M. Di Tada, G.M. Santos, Analysis of plutonium, isotopes in marine samples by radiometric, ICP-MS and AMS techniques, J. Radioanal. Nucl. Chem. 248 (2001) 757–764.
[23] T. Aramaki, T. Mizushima, T. Kuji, P.P. Povinec, O. Togawa, Distribution of radiocarbon in the Southwestern North Pacific, Radiocarbon 43 (2001) 857–867.
[24] P.P. Povinec, A.J.T. Jull, G.S. Burr, Radiocarbon in seawater at radioactive waste dumping sites in the Northeast Atlantic and Northwest Pacific, Radiocarbon 43 (2001) 879–886.
[25] P.P. Povinec, J.J. La Rosa, S.H. Lee, S. Mulsow, I. Osvath, E. Wyse, Recent developments in radiometric and mass spectrometry methods for marine radioactivity measurements, J. Radioanal. Nucl. Chem. 248 (2001) 713–718.
[26] P.P. Povinec, T. Aramaki, G.S. Burr, A.J.T. Jull, L. Liong Wee Kwong, O. Togawa, Radiocarbon in the water column of the southwestern North Pacific Ocean – 24 years after GEOSECS, Radiocarbon 46 (2004) 583–594.
[27] P.P. Povinec, Ultra-sensitive radionuclide spectrometry: radiometrics and mass spectrometry synergy, J. Radioanal. Nucl. Chem. 263 (2) (2005) 413–417.
[28] P.P. Povinec, Developments in analytical technologies for marine radionuclide studies, Radioact. Environ. 6 (2005) 237–294.
[29] P.P. Povinec, M. Betti, A.J.T. Jull, P. Vojtyla, New isotope technologies in environmental physics, Acta Phys. Slov. 58 (2008) 1–154.
[30] S.H. Lee, P.P. Povinec, E. Wyse, M.A.C. Hotchkis, Ultra-low-level determination of ^{236}U in IAEA marine reference materials by ICPMS and AMS, Appl. Radiat. Isot. 66 (2008) 823–828.
[31] S.H. Lee, P.P. Povinec, J. Gastaud, J.J. La Rosa, E. Wyse, L.K. Fifield, Determination of plutonium isotopes in seawater samples by Semiconductor Alpha Spectrometry, ICP-MS and AMS techniques, J. Radioanal. Nucl. Chem. 282 (2009) 831–835.
[32] P.P. Povinec, S.H. Lee, L. Liong Wee Kwong, B. Oregioni, A.J.T. Jull, W.E. Kieser, U. Morgenstern, Z. Top, Tritium, radiocarbon, ^{90}Sr and ^{129}I in the Pacific and Indian Oceans, Nucl. Instr. Meth. Phys. Res. B 268 (2010) 1214–1218.
[33] P.P. Povinec, R. Breir, L. Coppola, M. Groening, C. Jeandel, A.J.T. Jull, W.E. Kieser, S.H. Lee, L. Liong Wee Kwong, U. Morgenstern, Y.H. Park, Z. Top, Tracing of water masses using a multi isotope approach in the southern Indian Ocean, Earth Planet. Sci. Lett. 302 (2011) 14–26.
[34] D.J. Donahue, J.W. Beck, D. Biddulph, G.S. Burr, C. Courtney, P.E. Damon, A.L. Hatheway, L. Hewitt, A.J.T. Jull, T. Lange, N. Lifton, R. Maddock, L.R. McHargue, J.M. O'Malley, L.J. Toolin, Status of the NSF-Arizona AMS laboratory, Nucl. Instr. Meth. Phys. Res. B 123 (1997) 51–56.
[35] A.E. Litherland, R.P. Beukens, J.P. Doupe, W.E. Kieser, J.S. Krestow, J.C. Rucklidge, I. Tomski, G.C. Wilson, X.-L. Zhao, Progress in AMS research at Iso Trace, Nucl. Instr. Meth. Phys. Res. B 172 (2000) 206–210.
[36] A. Priller, T. Brandl, R. Golser, W. Kutschera, S. Puchegger, W. Rom, P. Steier, C. Vockenhuber, A. Wallner, E. Wild, Extension of the measuring capabilities at VERA, Nucl. Instr. Meth. Phys. Res. B 172 (2000) 100–106.
[37] P.P. Povinec, J. Masarik, P. Kúš, K. Holý, M. Ješkovský, R. Breier, J. Staníček, A. Šivo, M. Richtáriková, A. Kováčik, J. Szarka, P. Steier, A. Priller, A new IBA-AMS laboratory at the Comenius University in Bratislava (Slovakia), Nucl. Instr. Meth. Phys. Res. B 342 (2015) 321–326.
[38] National Electrostatics Corp., Instruction manual No. 2JT045500 for MC-SNICS Ion Source. Middleton, 2011.
[39] National Electrostatics Corp., Instruction manual No. 2AT067500 for 9SDH-2 AMS Pelletron. Middleton, 2011.
[40] L. Liong Wee Kwong, P.P. Povinec, A.J.T. Jull, Preparation of graphite targets from small marine samples for AMS radiocarbon measurements, Radiocarbon 46 (2004) 133–139.
[41] J.S. Vogel, J.R. Southon, D.E. Nelson, T.A. Brown, Performance of catalytically condensed carbon for use in Accelerator Mass Spectrometry, Nucl. Instr. Meth. Phys. Res. B 5 (1984) 289–293.
[42] J. Liebl, R. Avalos Ortiz, R. Golser, F. Handle, W. Kutschera, P. Steier, E.M. Wild, Studies on the preparation of small ^{14}C samples with an RGA and ^{13}C-enriched material, Radiocarbon 52 (2010) 1394–1404.
[43] X.L. Hou et al., Iodine-129 in seawater offshore Fukushima: distribution, inorganic speciation, sources, and budget, Environ. Sci. Technol. 47 (2013) 3091–3098.
[44] P.P. Povinec, M. Aoyama, D. Biddulph, R. Breier, K. Buesseler, C.C. Chang, R. Golser, X.L. Hou, M. Ješkovský, A.J.T. Jull, J. Kaizer, M. Nakano, H. Nies, L. Palcsu, L. Papp, M.K. Pham, P. Steier, L.Y. Zhang, Cesium, iodine and tritium in NW Pacific waters – a comparison of the Fukushima impact with global fallout, Biogeosciences 10 (2013) 5481–5496.
[45] S.D. Park, J.S. Kim, S.H. Han, Y.K. Ha, K.S. Song, K.Y. Jee, The measurement of ^{129}I for the cement and the paraffin solidified low and intermediate level wastes (LILWs), spent resin or evaporated bottom from the pressurized water reactor (PWR) nuclear power plants, Appl. Radiat. Isot. 67 (2009) 1676–1682.

[46] T. Jabbar, P. Steier, G. Wallner, N. Kandler, C. Katzlberger, AMS analysis of iodine-129 in aerosols from Austria, Nucl. Instr. Meth. Phys. Res. B 269 (2011) 3183–3187.
[47] X. Hou, V. Hansen, A. Aldahan, G. Possnert, O.C. Lind, G. Lujaniene, A review on speciation of iodinie-129 in the environmental and biological samples, Anal. Chim. Acta 632 (2009) 181–196.
[48] J. Argyriades, Results of the BiPo-1 prototype for radiopurity measurements for the SuperNEMO double beta decay source foils, Nucl. Instr. Meth. Phys. Res. A 622 (2010) 120–128.
[49] G. Angloher et al., EURECA conceptual design report, Phys. Dark Universe 3 (2014) 41–74.
[50] W. Maneschg, M. Laubenstein, D. Budjáš, W. Hampel, G. Heusser, K.T. Knoepfle, B. Schwingenheuer, H. Simgen, Measurements of extremely low radioactivity levels in stainless steel for GERDA, Nucl. Instr. Meth. Phys. Res. A 593 (2008) 448–453.

Appendix D

Recent results from the AMS/IBA laboratory at the Comenius University in Bratislava: preparation of targets and optimization of ion sources

J Radioanal Nucl Chem (2016) 307:2101–2108
DOI 10.1007/s10967-015-4406-9

Recent results from the AMS/IBA laboratory at the Comenius University in Bratislava: preparation of targets and optimization of ion sources

Pavel P. Povinec[1] · Jozef Masarik[1] · Miroslav Ješkovský[1] · Robert Breier[1] · Jakub Kaizer[1] · Ján Pánik[1] · Marta Richtáriková[1] · Jaroslav Staníček[1] · Alexander Šivo[1] · Jakub Zeman[1]

Received: 12 June 2015 / Published online: 27 August 2015

Abstract Developments of solid targets and optimizations of ion sources were carried out with the aim to produce high ion yields for applications of tandem accelerators as mass spectrometers. A comparison of Al^- yields from different aluminum targets showed that the best results were obtained with AlN targets. Transmission studies of ^{9}Be and ^{12}C ions through the Pelletron accelerator showed highest efficiencies for $^{9}Be^{2+}$ and $^{12}C^{2+}$. First results obtained with a simplified version of the AMS line are presented as well.

Keywords Accelerator mass spectrometry (AMS) · Ion beam analysis (IBA) · Tandem accelerator · Pelletron · CENTA

Introduction

Nuclear physics research, especially development of tandem accelerator technologies has had important impact on applications of small accelerators in environmental, biomedical and material sciences. The recent developments in accelerator technologies for AMS and IBA analyses have been an inspiration for creation of a Centre for Nuclear and Accelerator Technologies (CENTA) at the Comenius University in Bratislava (Slovakia). A state-of-the-art tandem accelerator laboratory has been designed for (i) AMS studies of long-lived radionuclides in environmental, life and space sciences, (ii) IBA applications in environmental, life and material research, including cultural heritage studies, (iii) nuclear reaction studies with charged particles for new generations of fission reactors, for thermonuclear reactors, and for astrophysics investigations.

The AMS analyses of long-lived radionuclides [1–12] represent the most important development in radioanalytical techniques since the development of HPGe detectors and their operation in underground laboratories [7, 11, 13–15]. The AMS technology has been widely used in environmental studies, both terrestrial and marine. Specific applications included tracing of long-lived radionuclides (^{10}Be, ^{14}C, ^{36}Cl, ^{129}I, U-isotopes, etc.) in climate change, atmospheric, hydrology, marine, geology and geophysics studies [2, 10, 16–19]. Some of the cosmogenic radionuclides (e.g. ^{10}Be, ^{14}C, ^{26}Al, ^{36}Cl, ^{41}Ca, ^{53}Mn, etc.) have been widely applied in space research, e.g. in analysis of meteorites and lunar samples [7, 20–23]. The AMS technology has also been frequently used in radioecology research, e.g. in atmospheric radioactivity monitoring (e.g. ^{14}C, ^{129}I, U and Pu isotopes, etc.) around nuclear reprocessing and nuclear power plants [24–26]. Actinides (U and Pu isotopes), and other long-lived radionuclides on the other hand have been playing an important role in the case of nuclear accidents (e.g. the Chernobyl accident), in long-term storage of radioactive wastes, or their dumping in the sea (e.g. ^{14}C, ^{129}I, ^{135}Cs, etc.) [9, 10, 27–29].

Recently the AMS techniques have been widely applied in tracing radionuclides released during the Fukushima accident to the terrestrial and marine environments [30]. Except the most frequently studied ^{134}Cs and ^{137}Cs (gamma-ray emitters easily measured with HPGe detectors [31, 32]), which have been important for delivery of post-accident radiation doses to the public and biota [33], there

✉ Pavel P. Povinec
povinec@fmph.uniba.sk

[1] Department of Nuclear Physics and Biophysics, Faculty of Mathematics, Physics and Informatics, Comenius University, 84248 Bratislava, Slovakia

have been many other radionuclides released during the accident [30, 34–36], requiring our attention. This has been motivated first of all because of delivery of radiation doses to the public and biota by long-lived radionuclides (e.g. ^{14}C, ^{129}I, ^{135}Cs, U and Pu isotopes, etc.), where especially the AMS technology (together with Inductively Coupled Plasma Mass Spectrometry (ICPMS), and Thermal Ionization Mass Spectrometry (TIMS)) has been recognized as the most sensitive analytical technique [7, 8, 10, 11, 37, 38].

The IBA technologies (e.g. PIXE, PIGE, RBS, etc.) together with the Nuclear Reaction Analysis (NRA) of environmental and material samples, and Ion Beam Modification (IBM) of materials (e.g. for construction of new generations of nuclear and thermonuclear reactors) represent the most successful applications of small accelerator technologies in various branches of science [39, 40]. The IBA technologies may also help better understanding of behavior of long-lived radionuclides in the environment via studying suitable stable elements as their analogues.

In this paper we present a short description of the CENTA laboratory, focusing on the laboratory design, description of the basic equipment and discussion of its characteristics. The first results obtained with a simplified version of the AMS line are presented as well.

Experimental

Description of the tandem accelerator laboratory

The CENTA laboratory because of financial constrains has been built *per partes*, comprising the main equipment required for AMS and IBA analytical work. The design of the laboratory has been driven by general needs to establish in Slovakia a national laboratory devoted to ion beam studies and applications, and to assure for the future wide-range research capabilities and successful participation in international programs. The present laboratory design comprises of two ion sources (for gas and solid targets), the injection system, the 3 MV tandem accelerator, and a high energy analyzer with two ion beam end stations for PIGE/PIXE, NRA and AMS applications. All available equipment was supplied by the National Electrostatics Corporation (NEC, Middleton, USA). A floor scheme of the tandem accelerator laboratory is presented in Fig. 1. The near future installation will include a fully equipped AMS line with 90° magnet, an electrostatic spectrometer, and the end of the line detector. Later installations will include a nuclear microscope, a raster station for IBM studies of materials, and a station for biomedical research.

A dedicated hall to accommodate the tandem accelerator laboratory has been built at the Comenius University campus at Mlynská dolina. The hall design separates the ion beam channels (placed in a bunker covered by soil) from the AMS line, enabling thus work in different radiation environments (Fig. 1). Neutron and gamma-ray detectors monitor radiation situation in the main hall.

The laboratory is equipped with an Alphatross ion source (radio frequency plasma source producing ions from gases), and with MC-SNICS source (MultiCathode Source of Negative Ions by Cesium Sputtering) having a wheel accommodating up to 40 solid targets (Fig. 2). All elements, which can exist in gaseous form and can form negative ions (either atomic or molecular) could be considered candidates for ion production in the Alphatross ion source. The MC-SNICS ion source is used for production of ions from solid targets (from lithium to transuranics).

The ion beams from the Alphatross and MC-SNICS sources are forwarded to an electrostatic analyzer (ESA) with 300 mm radius of electrodes, mounted on a rotatable platform (Figs. 1, 2). The ion beams from both ion sources are chosen for analysis, where the first E/q separation is made. The X–Y steerers and slits can be used for beam tuning, attenuation and analysis before entering the injection magnet. The momentum analysis ME/q^2, and separation of ions before acceleration is made by double focusing 90° magnet with bending radius of 0.4572 m. The mass resolution of the injection magnet (for a 3 mm beam spot and the dispersion constant $D_m = 4$) is $m/\Delta m = 305$. After the proper mass is selected, another set of slits is used for parameterization of the beam, and a Faraday cup is used for measurements of ion currents. Negative ion beams produced in Alphatross or MC-SNICS ion sources, pre-accelerated to modest energies (40–100 keV), are then injected into the tandem accelerator.

A 3 MV tandem electrostatic accelerator (NEC Pelletron Model 9SDH-2) can accelerate a variety of ion species over a broad range of energies for use in AMS, IBA, IBM, and nuclear physics/astrophysics studies. The terminal is provided with a gas (presently nitrogen) stripping system. The energy of accelerated ions depends mainly on the terminal voltage and on the charge state of accelerated ions. The accelerator is housed in a pressure vessel (diameter of 1.22 m and length of 5.64 m), which allows an evacuation and subsequent filling with sulphur hexafluoride (SF6) insulating gas required for high voltage operation. A cryogenic-vacuum/pressure apparatus used for the evacuation, transport and storage of SF_6 gas has been supplied by the DILO company (Germany).

The ions accelerated in the Pelletron are then focused in the high-energy beam line with a magnetic quadrupole triplet lens, and a Y-axis electrostatic steerer (Figs. 1, 2). The quadrupole magnet is primarily used for IBA and NRA applications. The switching magnet, presently also used as an analyzing magnet for AMS ($ME/Z^2 = 300$ amu-MeV

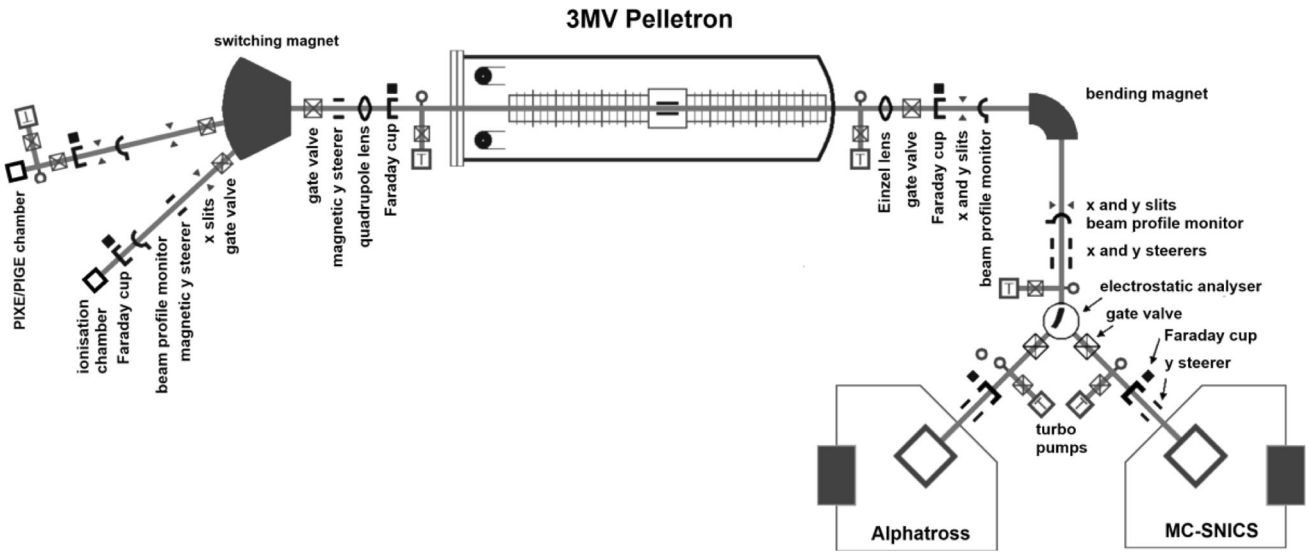

Fig. 1 Floor scheme of the tandem accelerator laboratory

@ ± 15°), is equipped with seven ports at ± 45°, ±30°, ±15°, and 0° with respect to the accelerator. The beam lines from these ports will be used for IBA (channeling, RBS, PIXE, PIGE), IBM, nuclear reaction studies, nuclear microscope and for biomedical applications. The +45° and +15° beam lines are currently equipped with slits to control the divergence of the ion beam, with X–Y electromagnetic steerers, with Faraday cups for current measurements and with beam profile monitors. A PIXE/PIGE end station has been installed at the +15° port. The other end of the line detectors (an ionization chamber, silicon detector, time of flight detector) for the total energy analysis of ions, for analysis of their energy loses and their residual energy will also be installed soon. The switching magnet can also be used to select the energy and charge state of the ions to be delivered to the end station as a dedicated beam line for AMS analysis will be installed later.

Preparation of graphite targets for ^{14}C analysis by AMS

A vacuum-cryogenic apparatus was constructed to produce CO_2 either by combustion of samples in oxygen atmosphere, or by acid evolution (Fig. 3). The graphitization apparatus is located in a clean laboratory dedicated for preparation of radiocarbon samples. The line is made of borosilicate glass and is used for extraction of CO_2 from various samples, e.g. groundwater, seawater, solid carbonates and organic samples. The line has an advantage in extracting carbon dioxide and its graphitization in the same place, what substantially lowers a risk of contamination. The vacuum in the line can go down to $\sim 10^{-5}$ torr with the use of rotary and diffusion pumps. The CO_2 after its extraction from samples is purified by passing through water vapor traps kept at −45 °C and silver (wool) plus copper (granules) furnaces heated to about 900 °C. After the purification the CO_2 is then injected into the graphitization reactor. Precisely known volumes of the pure CO_2 were then reduced to graphite in four graphite reactors.

We compared two graphitization procedures: one is using for the graphitization reaction Zn and Fe [41], the second method is using externally supplied hydrogen from a gas cylinder [42]. In the first reaction

$$CO_2 + Zn \rightarrow CO + ZnO$$

$$2CO \rightarrow CO_2 + C \text{ (graphite)}$$

the reduction was carried out with Zn in the presence of dendritic Fe (200 mesh). Both chemicals were carefully weighed and introduced into the glass tubes. They were then connected to the graphite apparatus, together with a tube filled with purified CO_2 extracted from a sample. The air above was pumped out and the CO_2 was transferred cryogenically to the reactor. The Zn tube was then heated to 450 °C, which pre-reduced CO_2 to CO. After 1 h, the Fe was heated to 550 °C and graphite was produced and deposited onto the Fe. The pressure was constantly monitored until the reaction was completed, which usually takes between 8 and 10 h. The produced graphite was then carefully weighed.

Fig. 2 View of the main components of the tandem laboratory. **a** Alphatross (*left*) and MC-SNICS ion sources (*right*); **b** Injection line; **c** Pelletron accelerator with control system; **d** Ion analyzer with switching magnet and ion beam lines

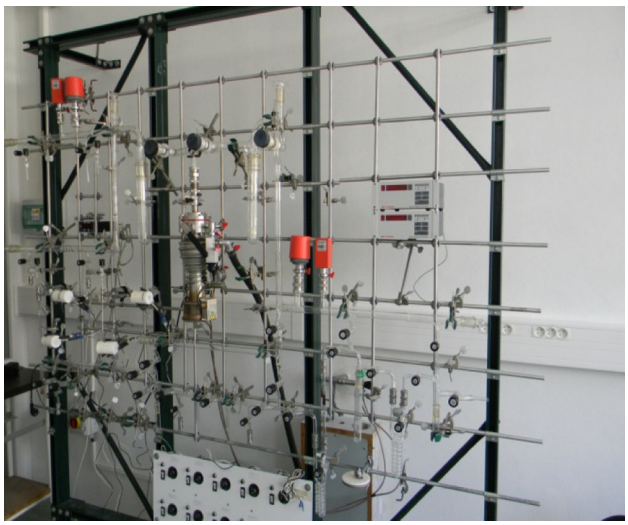

Fig. 3 Combustion-graphitization line for preparation of ^{14}C targets for AMS measurements

The second method is based on the following reaction [42]:

$$CO_2 + 2H_2 \xrightarrow[Fe]{500-900\,^{\circ}C} C + 2H_2O$$

A graphitization reactor is comprised of a reaction tube (with the iron catalyst inside), heated with an electric oven, a water trap (a tube cooled with methanol and liquid nitrogen to about −45 °C) and a pressure transducer (for monitoring of the pressure during the graphitization). There are four graphitization reactors altogether. High-purity iron powder (325 mesh) is used as the catalyst. An appropriate amount of Fe catalyst is weighed in a reaction tube mounted to a graphitization reactor, which is then pre-heated in the presence of hydrogen. Hydrogen gas (purity of 99.9 %) used for the catalyst activation and graphitization itself, originates from an external gas bottle. The amount of hydrogen used for graphitization equals approximately double the amount of the CO_2 sample. Typically, the reaction is ended in less than 4 h with a yield of 98 %, which is calculated from the pressure decline during the reaction, and also confirmed gravimetrically.

Results and discussion

Several studies have been carried out till now in the CENTA laboratory, including investigations of characteristics of ion sources, ion transmission efficiency studies [43, 44], optimization of ion yields from UF_4 and UO targets for analysis of uranium isotopes by AMS [25], analysis of ^{10}Be by AMS [43], development of ^{14}C and ^{129}I targets for AMS analyses [44, 45], and ^{14}C analysis in

single tree-ring samples [25, 45]. Here we shall focus only on a few recent results.

Comparison of methods for preparation of graphite targets

The full procedure of preparation of graphite targets was tested by burning several samples of the oxalic-acid standard reference material (HOxII, NIST SRM 4990C) of the National Institute of Standards and Technology's (Gaithersburg, USA). The graphite yields as obtained by both methods were calculated gravimetrically and also barometrically from pressure readings. In the case of the first method about 2 mg of carbon was found to be the appropriate amount for synthesis. For complete reduction, the pressure should drop to zero, meaning all gaseous CO_2 and CO has been reduced to solid graphite. Figure 4, depicting the variation of pressure with time, shows that a successful synthesis with a yield of about 98 % was reached. Sometimes a lower synthesis, with a yield of about 95 % was reached, as the curve did not return to a zero pressure state, probably because of the presence of water vapors in the system. The mass of Fe used, enabling to reach an acceptable ionic current in the AMS source, was twice the amount of carbon that needed to be reduced.

Several parameters, including reactor volume, amount of iron catalyst and its type, temperature and catalyst activation conditions were studied in the hydrogen method with the aim to reduce a reaction time and increase a final yield of the graphitization. Increasing the reactor volume from 9.1 ml to 18.2 enhanced the yield by about 6 %, and shortened the reaction time by about 80 min. Varying of the Fe catalyst amount has little or no effect, an optimal value was set between 4 and 6 mg. It has been found that the first step of the overall reaction—the reduction of CO_2 to CO—has improved if done at higher temperature, i.e. 900 °C. After 0.5 h the temperature is lowered to 550 °C for the rest of the graphitization. Heating of the iron powder in the presence of hydrogen (600 °C, 1 h) was chosen as our standard catalyst activation procedure, though if compared to heating in the open atmosphere and vacuum respectively, the yield and time difference was rather small.

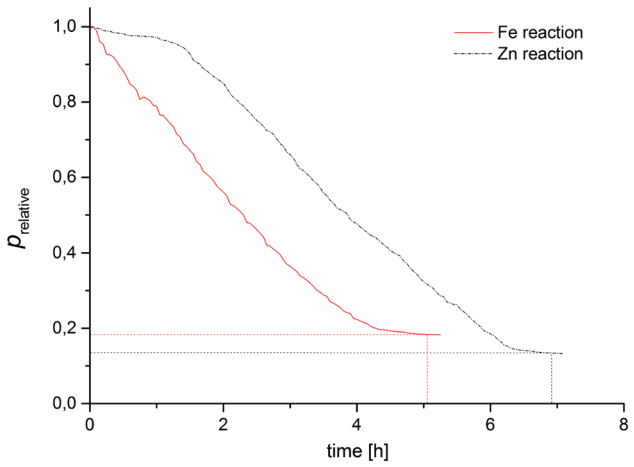

Fig. 4 Comparison of pressure–time records obtained with different graphitization methods (*top line* a reactor without external hydrogen; *bottom line* a reactor with external hydrogen)

Figure 4 compares history of two graphitization processes, with and without external supply of hydrogen, expressed as the reactor pressure and the reaction time. It is clearly seen that the optimization in the hydrogen procedure resulted in a much faster reaction (below 4 h), and slightly increased yield up to 98 %. Therefore, the method with external hydrogen has been routinely used for preparation of graphite targets for AMS ^{14}C measurements.

Investigation of aluminum targets for AMS analysis

Different aluminum samples were tested as possible targets in the MC-SNICS ion source for preparation of Al ions for ^{26}Al measurements by AMS. It is well known that aluminum does not have high yields of negative ions as for example chlorine, carbon or beryllium. As it is disadvantageous to use metallic aluminum in the ion source (e.g. in the form of aluminum powder, wires or sheets) because of low ion yields, synthesized targets should be prepared. The Al_2O_3 target could be a compromise because it is stable at high temperatures used in the ion source, it is not toxic, it is stable on the air, and relatively easy to be prepared from geological or biological samples. However, there are also disadvantages, e.g. a high concentration of oxygen, and a high electrical resistance of the oxide. Therefore it should be mixed with good conductor, e.g. iron, copper or silver.

On the other hand AlN could be a promising target material as it could produce higher ion yields, and as nitrogen does not form negative ions, it should not interfere with production of Al^- ions. The disadvantages of AlN include more complicated preparation chemistry (an air-free Schlenk-type technique), its sensitivity to water vapors (formation of $AlOH_3$), and lower electrical conductivity [46, 47].

Several aluminum samples (Al_2O_3, AlF_3, AlN, and Al_2SO_4) were tested in the MC-SNICS ion source with the aim to study Al^- ion yields. A comparison of mass spectra obtained with Al_2O_3 and AlN targets mixed with Fe powder at the ratio 2:1 shows that the best yields have been obtained with the AlN target (Fig. 5). Lower Fe mixing ratios, or mixing of the targets with Cu or Ag (for getting a better thermal and electric conductivity) gave lower yields. In both mass spectra we also see ^{63}Cu and ^{65}Cu peaks from the copper cathode in which Al + Fe mixtures were

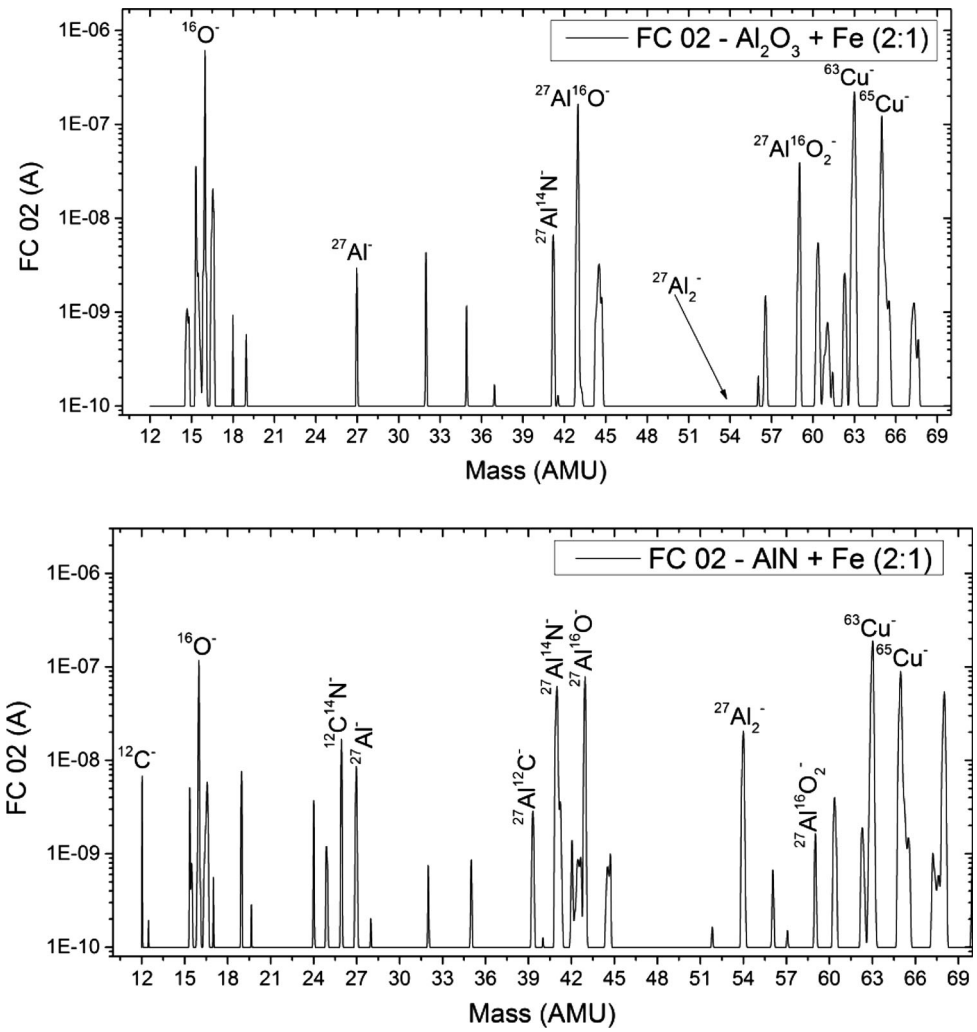

Fig. 5 Comparison of mass spectra of the Al_2O_3 and AlN targets mixed with Fe powder

pressed. The peak with mass of 26 seen in the AlN mass spectrum is not due to the radioactive ^{26}Al for which we are looking for in AMS measurements, but this is interference from $^{12}C^{14}N^-$.

Transport of ions through the accelerator system

The Alphatross and MC-SNICS ion sources were optimized for IBA and AMS operations, including studies of transmission characteristics of accelerated ions with different energy and charge states. The nitrogen gas pressure in the gas stripper has been optimized for different ions and charge states. For example, the maximum transmission efficiencies at 3 MV obtained for $^9Be^{1+}$, $^9Be^{2+}$ and $^9Be^{3+}$ ions used for AMS measurements of ^{10}Be were about 30, 52 and 5 %, respectively (Fig. 6). The $^9Be^{2+}$-beam tuned to the end Faraday cup had the diameter of 2 mm.

In the case of ^{12}C ions the maximum transmission efficiencies at 3 MV obtained for $^{12}C^{2+}$, $^{12}C^{3+}$, $^{12}C^{4+}$ and $^{12}C^{5+}$ were about 45, 33, 23 and 0.6 %, respectively (Fig. 6).

AMS analysis of ^{10}Be standard and background samples

As an example of the first AMS measurements carried out at the CENTA facility we present an analysis of ^{10}Be [48]. AMS analysis of ^{10}Be using only a small switching magnet as the ion analyzer (Fig. 1) was tested. The method for suppression of ^{10}B ions, based on a silicon nitride foil stack used as a passive absorber was developed earlier at the VERA laboratory. The AMS analysis of ^{10}Be is mainly limited by the stable isobar ^{10}B, while the requirements for mass separation are the least stringent of all standard radionuclides analyzed by AMS. The MC-SNICS was used for the production of $^{10}BeO^-$ ions, which were mass separated and injected into the 9SDH-2 Pelletron, operating at 3 MV terminal voltage. As already mentioned, the $^{10}Be^{2+}$

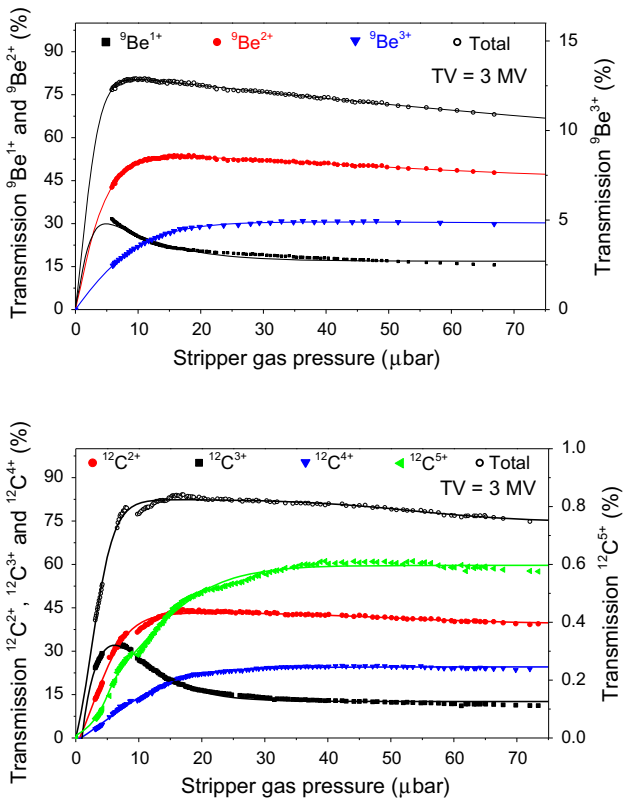

Fig. 6 Transmission of ^{9}Be and ^{12}C ions on the stripper gas (N_2) pressure at the terminal voltage of 3 MV

ions were selected for analysis because of highest transmission efficiency. The ^{10}B ions, as well as of most background ions from heavier masses were absorbed in the silicon nitride stack introduced in front of the ionization chamber consisting of two anodes (based on the ETH Zürich design [49]), which was used for the ion detection. The standard ^{10}Be source (S555 developed at ETH Zürich [50]) with the $^{10}Be/^{9}Be$ mass ratio of $(8.71 \pm 0.24) \times 10^{-11}$ was used in these measurements. Using this setup, a detection limit for $^{10}Be/^{9}Be$ of the order of 10^{-12} was achieved, which was mainly determined by scattering of $^{9}Be^{2+}$ ions (energy of 7.059 MeV) on residual gas inside the switching magnet.

Conclusions

The ion sources, the Pelletron accelerator and the analyzer of accelerated ions installed in the CENTA laboratory have been described. Preliminary results indicated a reliable operation of all parts of the system. A vacuum-cryogenic apparatus has been constructed and a method for preparation of graphite targets for ^{14}C AMS analysis has been developed. It has been shown that the method using external hydrogen for graphitization of samples has been faster and more reliable than the Zn method. A comparison of Al^- yields from different aluminum targets in the MC-SNICS ion source showed that the best results were obtained with AlN and Al_2O_3 targets mixed with iron powder at the ratio of 2:1. Transmission studies of ^{9}Be and ^{12}C ions on the pressure of nitrogen gas in the gas stripper of the Pelletron accelerator and on the charge states of the ions showed that the highest efficiencies were obtained for $^{9}Be^{2+}$ (52 %) and $^{12}C^{2+}$ (45 %). A simplified system for AMS analysis of ^{10}Be using the switching magnet (as the analyzing magnet) and an ionization chamber with a silicon nitride stack absorber for ^{10}B isobar suppression achieved a detection limit for $^{10}Be/^{9}Be$ mass ratio of the order of 10^{-12}.

A wide range of samples were used for ^{14}C AMS analysis including, atmospheric CO_2, tree-ring, groundwater, seawater, sediment, canvas, pergamon, charcoal, mortar, and bone samples. It is planned that a complete AMS line will also be available soon. The scientific program of the CENTA will be devoted mainly to nuclear, environmental, material and life sciences.

Acknowledgments A support provided by the EU Research and Development Operational Program funded by the ERDF (projects Nos. 26240120012, 26240120026 and 26240220004) has been crucial for establishing the CENTA laboratory. The authors are also acknowledging support from the Technical Cooperation Program of the International Atomic Energy Agency (project No. SLR/0/008), and from the Nuclear Regulatory Authority of the Slovak Republic. They are also indebted to Profs. R. Golser, A. Priller, and P. Steier of the Vienna University for support during development of the AMS system. The staff of the Comenius University is acknowledged for assistance during various stages of preparation and building of the CENTA laboratory.

References

1. Tuniz C, Bird JR, Fink D, Herzog GF (1998) Accelerator mass spectrometry: ultrasensitive analysis for global science. CRC Press, Boca Raton
2. Kutschera W (2005) Intern J Mass Spectrom 242:145–160
3. Povinec PP (2005) J Radioanal Nucl Chem 263:413–417
4. Povinec PP, Sanchez-Cabeza JA (eds) (2006) Radionuclides in the environment. Elsevier, Amsterdam
5. Povinec PP (ed) (2008) Analysis of environmental radionuclides. Elsevier, Amsterdam
6. Povinec PP (2008) J Radioanal Nucl Chem 276:771–777
7. Povinec PP, Betti M, Jull AJT, Vojtyla P (2008) Acta Phys Slovaca 58:1–154
8. Lee SH, Povinec PP, Gastaud J, La Rosa J, Wyse E, Fifield LK (2009) J Radioanal Nucl Chem 282:831–835
9. Lehto J, Hou XL (2010) Chemistry and analysis of radionuclides. Wiley, Weinheim
10. Povinec PP (2004) In: Livingston HD (ed) Marine radioactivity. Elsevier, Amsterdam
11. Povinec PP, Eriksson M, Scholten J, Betti M (2012) In: Annunziata M (ed) Handbook of radioactivity measurement. Elsevier, Amsterdam
12. Povinec PP (2013) J Radioanal Nucl Chem 295:537–544

13. Povinec PP, Comanducci JF, Levy-Palomo I (2004) Appl Rad Isotopes 61:85–93
14. Povinec PP, Comanducci JF, Levy-Palomo I (2005) J Radioanal Nucl Chem 263:441–445
15. Povinec PP (2012) J Anal Sci Technol 3:42–71
16. Povinec PP, Lee SH, Kwong LLW, Oregioni B, Jull AJT, Kieser WE, Morgenstern U, Top Z (2010) Nucl Instrum Meth Phys Res B 268:1214–1218
17. Povinec PP, Zenisova Z, Sivo A, Ogrinc N, Richtáriková M, Breier R (2013) Radiocarbon 55:1017–1028
18. Povinec PP, Breier R, Coppola L, Groening M, Jeandel C, Jull AJT, Kieser WE, Lee SH, Kwong LLW, Morgenstern U, Top Z (2011) Earth Planet Sci Lett 302:14–26
19. Fabel D, Stroeven AP, Harbor J, Kleman J, Elmore D, Fink D (2002) Earth Plant Sci Lett 201:397–406
20. Povinec PP, Laubenstein M, Ferrière L, Brandstätter F, Sýkora I, Kováčik A, Jull AJT, Topa D, Koeberl C (2015) Meteor Planet Sci 50:273–286
21. Poutivtsev M, Dillmann I, Faestermann T, Knie K, Korschinek G, Lachner J, Meier A, Rugel G, Wallner A (2010) Nucl Inst Meth Phys Res B 268:756–758
22. Jull AJT, McHargue LR, Bland PA, Greenwood RC, Bevan AWR, Kim KJ, Giscard MD, LaMotta SE, Johnson JA (2010) Meteor Planet Sci 45:1271–1283
23. Leya I, Welten KC, Nishiizumi K, Caffee MW (2009) Meteor Planet Sci 44:77–85
24. Molnár M, Major I, Haszpra L, Svetlik I, Svingor E, Veres M (2010) J Radioanal Nucl Chem 286:471–476
25. Povinec PP, Svetlik I, Ješkovský M, Šivo A, John J, Špendlíková I, Němec M, Kučera J, Richtáriková M, Breier R, Fejgl M, Černý R (2015) J Radioanal Nucl Chem 304:67–73
26. Livingston HD, Povinec PP (2000) Ocean Coast Manag 43:689–712
27. Steier P, Hrnecek E, Priller A, Quinto F, Srncik M, Wallner G, Winkler S (2013) Nucl Instrum Methods Phys Res B 294: 160–164
28. Lujanienė G, Beneš P, Štamberg K, Šapolaite J, Vopalka D, Radžiute E, Ščiglo T (2010) J Radioanal Nucl Chem 286: 353–359
29. Povinec PP, Oregioni B, Jull AJT, Kieser WE, Zhao XL (2000) Nucl Instrum Meth Phys Res B 172:672–678
30. Povinec PP, Hirose K, Aoyama M (2013) Fukushima accident: radioactivity impact on the environment. Elsevier, New York
31. Levy I, Povinec PP, Aoyama M, Hirose K, Sanchez-Cabeza JA, Comanducci J-F, Gastaud J, Eriksson M, Hamajima Y, Kim CS, Komura K, Osvath I, Roos P, Yim SA (2011) Prog Oceanogr 89:120–133
32. Povinec PP (2011) J Anal Sci Technol 2(Suppl A):A15–A21
33. Povinec PP, Hirose K (2015) Sci Rep 5:9016. doi:10.1038/srep09016
34. Steinhauser G (2014) Environ Sci Technol 48(9):4649–4663
35. Hou XL, Povinec PP, Zhang LY, Biddulph D, Chang C-C, Fan YK, Golser R, Jeskovsky M, Jull AJT, Liu Q, Shi KL, Steier P, Zhou WJ (2013) Environ Sci Technol 47:3091–3098
36. Povinec PP, Aoyama M, Biddulph D, Breier B, Buesseler K, Chang CC, Golser R, Hou XL, Jeskovsky M, Jull AJT, Kaizer J, Nakano M, Nies H, Palcsu L, Papp L, Pham MK, Steier P, Zhang LY (2013) Biogeosciences 10:5481–5496
37. Lee SH, Povinec PP, Wyse E, Hotchkis MAC (2008) Appl Rad Isotopes 66:823–828
38. Zheng J, Tagami K, Homma-Takedaa S, Buab W (2013) J Anal At Spectrom 28:1676–1699
39. Jeynes C, Webb RP, Lohstroh A (2011) Rev Accel Sci Technol 4:41–82
40. Hosemann P (2011) Rev Accel Sci Technol 4:161–182
41. Liong Wee Kwong L, Povinec PP, Jull AJT (2004) Radiocarbon 46:133–139
42. Vogel JS, Southon JR, Nelson DE, Brown TA (1984) Nucl Instrum Meth Phys Res B 5:289–293
43. Povinec PP, Masarik J, Kúš P, Holý K, Ješkovský M, Breier R, Staníček J, Šivo A, Richtáriková M, Kováčik A, Szarka J, Steier P, Priller AA (2015) Nucl Instrum Meth Phys Res B 342:321–326
44. Povinec PP, Masarik J, Ješkovský M, Kaizer J, Šivo A, Breier R, Pánik J, Staníček J, Richtáriková M, Zahoran M, Zeman J (2015) Nucl Instrum Meth Phys Res B. doi:10.1016/j.nimb.2015.02.021
45. Povinec PP, Šivo A, Ješkovský M, Svetlik I, Richtáriková M, Kaizer J (2015) Radiocarbon 57:355–362
46. Flarend R et al (2004) Nucl Instrum Meth Phys Res B 223–224:263–267
47. Sharma P et al (2000) Nucl Instrum Meth Phys Res B 172:112–123
48. Ješkovský M, Steier P, Priller A, Breier R, Povinec PP, Golser R (2015) Nucl Instrum Meth Phys Res B. doi:10.1016/j.nimb.2015.04.072
49. Stocker M, Döbeli M, Grajcar M, Suter M, Synal H-A, Wacker L (2005) Nucl Instrum Meth Phys Res B 240:483–486
50. Christl M, Lachner J, Vockenhuber C, Lechtenfeld O, Stimac I, van der Loeff MR, Synal H-A (2012) Geochim Cosmochim Acta 77:98–107